Cholinergic Modulation of Network Activity and Applications in Sleep, Memory and Anesthesia

by

Bolaji Paul Eniwaye

A dissertation submitted in partial fulfillment
of the requirements for the degree of
Doctor of Philosophy
(Applied Physics and Scientific Computing)
in the University of Michigan
2023

Doctoral Committee:

Professor Michal Zochowski, Co-Chair
Professor Victoria Booth, Co-Chair
Associate Professor Sara Aton
Professor Alfred Hero
Professor Anthony Hudetz

Bolaji Paul Eniwaye
ENIWBOLA@umich.edu
ORCID ID: 0000-0002-2455-6973

Acknowledgements

"Three passions, simple but overwhelmingly strong, have governed my life: the longing for love, the search for knowledge, and unbearable pity for the suffering of mankind. These passions, like great winds, have blown me hither and thither, in a wayward course…". This quote, is from my favorite passage, an excerpt from the prologue to the auto biography of Betrand Russell, Nobel Laureate in literature and co-author of the Principia Mathematica.

In middle school when my 6th grade teacher asked me what I wanted to be when I grew up I confidently answered, “I want to be an Astrophysicist”. “Astronaut you mean?”, she replied, to which I corrected her, “Astrophysicist”. This answer was likely inspired by late night broadcasts of “Nova” occasionally narrated by Neil deGrasse Tyson and an encyclopedia I owned about the solar system. Fortunately or unfortunately this would change after my junior year in high school where a biology course made me realize that, as complex as the solar system is, life on earth is seemingly just as complex, eventually leading me to major in biomedical engineering in college. The accrual of and pursuit of many different passions over the years eventually led me to the University of Michigan which has been a journey of its own. This journey until now would not be complete without the many people who have helped me along the way.

.

First, I would like to thank my parents who selflessly supported me throughout my life and on my academic journey. Specifically, I’d like to thank my mother Elaine, for her unwavering and unconditional love and my father Olu, for serving as my first role model.

My deepest gratitude goes to my brother for always entertaining philosophical discussions and providing me interesting perspectives on life. Finally, I would like to thank my extended relatives, including the aunts and uncles that jointly raised me as well as my cousin for charting the waters of engineering ahead of me and showing me the many possibilities for the future.

My gratitude, however, isn't reserved to my family. I owe a lifetime of appreciation to all of the friends I've made until now. In high school, Joco and Juan Paul were my first friends, giving me a sense of community in an initially isolating environment, without whom I may not have graduated. Additionally, my thanks goes out Rajan, my high school rival, who pushed me excel and introduced me to a novel perspective of the world cultivated during our many after school car conversations.

In college and grad school I made a wealth of connections that not only shaped my intellectual curiosity but were also essential in molding my personality in adulthood. I would first like to thank the other two members of our physics trio, Tamra and Dean, for germinating my interest in physics, without whom I would never have considered graduate school. I would also like to thank the other two members of my engineering trio, Kay and Jenny for struggling with me in our biomed courses and subsequently becoming the closest thing to sisters that I will ever have. I am grateful to all of the people in mire court for bringing me out of my shell and giving me a sense of community in college as well as my prior romantic relationships for inspiring a wealth of introspection and reflection on the strength emotional connection. Finally, I would like to thank Ahmed for being my closest friend for nearly a decade and treating me like family though difficult times.

Prior to graduate school there have been many mentors that served as my inspiration and who I believe were directly responsible for my academic growth. The earliest of mentor that comes to mind is my 5th grade teacher Mr. Scanlan who instilled in me a passion for books and reaffirmed a confidence in my abilities despite my young age. In high school my biology teacher, Dr. White, fostered my love of biology and gave me an understanding of both the practical use of science as well as its significance in our

understanding of the world around us. In college, my advisors Professor Mark Kruse and Professor Gleb Finkelstein have my thanks for granting me an early exposure to scientific research and exposure to the frontiers of physics.

At the University of Michigan, I owe a lifetime of gratitude to the Applied Physics program, especially Cindy McNabb and Professor Cagliyan Kurdak, for their consistent encouragement, support, and guidance. To my advisers Professors Michal Zochowski and Victoria Booth , I thank you for giving me the infinite support and patience as well as the opportunity to learn and develop as a scientist. I would also like to thank the others on my committee for providing invaluable collaborative support and abundance of feedback. The valuable lessons I learned working as part of this team will serve me well as I start a new chapter in my professional career.

Similarly, I am grateful for my fellow researchers and lab mates in the Zochowski lab at the University of Michigan as well as the connections I made within my cohort for growing with me over the last few years. Lastly, I want to acknowledge financial support from the University of Michigan through the Rackham Merit Fellowship in addition to many other sources of support.

Table of Contents

List of Figures

List of Tables

Abstract

In all organisms, the nervous system allows for the ability to form complex responses to the environment leading to intricate behaviors that aid survival and facilitate social interactions in a complex ecosystem. Neurons are the presumed functional units that allow for such a complex range of behaviors and perceptual phenomena. In the nervous system, neurons work in tandem with a full range of complex signaling chemicals known as neuromodulators which tune neuron function to fit different behavioral tasks by varying temporal firing of the neurons. The aim of this dissertation is to use biophysically-based in-silico modeling to study how acetylcholine (ACh), one of the major neuromodulatory molecules in the brain, through its effect on cellular firing behavior, can affect brain function. As ACh modulates, among others, m-type voltage gated potassium currents through muscarinic receptors, neurons change their firing behavior in response to extracellular input. These changes are exhibited in both the average neuron firing rate as well as differences in phase relationships between coupled neurons. Our modeling results focus on elucidating how these cellular-level changes lead to modulation of network dynamics that can influence brain network functions.

First, we investigated the influence of ACh on neuron firing behavior and its network-wide implications in the transition between rate and phase coding of information. We used direct current input as a proxy for the effects of external stimuli on the network and found that for high ACh conditions, increased neural gain causes a dispersion of firing rates in response to the different magnitudes of these inputs. Additionally, ACh-induced increased neural responsiveness to input allowed neurons to persist in firing to maintain a representation in frequency space (rate coding). Alternatively, in low ACh conditions, phase coding was promoted through reduced frequency spread, increased neural resonance, and augmented propensity for synchronization.

Next, we analyzed how ACh-induced changes in firing behavior can contribute to the formation and consolidation of memories during non-rapid eye movement (NREM) sleep. Combining reduced neuronal network models and analysis of in vivo recordings, we tested the hypothesis that ACh-induced neuromodulatory changes during non-rapid eye movement (NREM) sleep mediate stabilization of network-wide temporal firing patterns, with the temporal order of neuronal firing dependent on their intrinsic mean firing rate during wake. We found, in both reduced models and in vivo recordings from mouse hippocampus, that the temporal order of firing among neurons during NREM sleep initially reflects their relative firing rates during prior wake. We also showed that learning-dependent reordering of sequential firing in the hippocampus during NREM sleep, together with spike timing-dependent plasticity (STDP), reconfigures neuronal firing rates across the network, similarly as has been reported in multiple brain circuits across periods of sleep.

Finally, we investigated changes in electrophysiological activity associated with anesthesia and showed that differences in synaptic transmission properties can emulate the observed alteration of neural firing patterns observed during states of anesthesia. We then proposed how these effects can be ameliorated by ACh-induced changes to the muscarinic receptor-based potassium currents. Specifically, we showed that increasing the influence of the muscarinic-mediated ACh effects under simulated anesthesia leads to an increase in firing rate and neural interaction measures, showing a population level reversal of anesthesia-induced changes in activity. We found that the simulated ACh reversal restored neurons' spiking activity, functional connectivity, as well as other measures of pairwise and population interactions.

Chapter I

Introduction

1.1 Cellular Basis of Nervous System Function

The brain is the most complex organ in the human body. Modern estimates suggest there are roughly 100 billion neurons with 100 trillion connections. This complexity allows for the executive control of most of the primary functions in the body as well as the emergence of emotion, sensation, memory and, finally, consciousness, leading to complex thought underpinning all human culture, creativity and innovation. The cross-species conservation of spatio-temporal function of the nervous system opens the avenue for animal experimental studies to elucidate how structure promotes function in the brain. These experimental studies have shed light on the cellular building blocks of the nervous systems with the most well studied units being the neuron. The neuron is a voltage sensitive cell whose functions can be abstracted to on and off spiking behavior. As neurons can connect to other neurons through synapses, this relatively simple behavior has complex implications such that elaborate spiking behaviors across neuronal networks can be observed [1]. This coordination is widely accepted to underlie all cognitive processes. Modern neuroscience employs both experimental, mathematical and computational approaches to understand how neural activity phenomena relate to

behavior and cognition [2,3]. A natural starting point would be to ask, what modulates the properties of neuron firing, and what implications can it have on cognitive phenomena? Answers to these questions get even more complicated, as neurons work in tandem with a full range of complex signaling chemicals known as neuromodulators which can change neural firing and response properties depending, for example on the vigilance state. In this thesis, we focus on the neuro-modulatory effects of acetylcholine and aim to understand its role in different neurological processes.

1.1.1 Neurons: Functional Units of the Nervous System

Neurons are the functional units of the nervous system with activity, upon depolarization, that is characterized by fast autonomic changes in membrane voltage potential commonly referred to as action potentials or spikes. Neurons vary in morphology but typically consist of axons, dendrites and a cell body [4]. When a neuron spikes, it sends a stereotypic signal down the axon to the axon terminal. This signal is then relayed from axon terminal to the dendrites of the post synaptic neuron through predominantly chemical synapses [5]. The amount of synaptic input a post synaptic neuron receives influences its propensity to spike as each neuron integrates all of its inputs to determine if it will fire.

1.1.2 Basic Biophysical Mechanisms Underlie the Function of Individual Neurons

Although the concept of neural transmission was first postulated by Ramon y Cajal after his discovery of the neuron in 1889 [6], a wealth of research has since contributed to the understanding of the electrochemical properties of neurons in their resting state as well as the dynamical mechanism of spike generation. In the resting state, a potential difference is maintained between the inside and outside of the neuron due to properties

of its lipid bilayer membrane which restricts the flow of ions into and out of the cell and contributes to capacitive properties of the cell. Ions can, however, pass through the membrane under certain conditions, specifically the cellular membrane includes voltage-gated ion channels that are selectively permeable to different types of ions. These ion channels can switch between open and closed states with a probability of occurrence that depends on the membrane potential [7]. In the neuron's resting state, Na+ and Cl- ions are more concentrated in the extracellular space outside of the membrane, whereas K+ and organic anions are more concentrated inside the cell. The maintenance of the concentration gradients of these ions is facilitated by Na+ -K+ pumps, which balance out the passive movement of these ions by transporting them against their electro-chemical gradients, i.e., they pump Na+ outside of the cell and K+ inside of the cell with the usage of ATP. In an equilibrium state, the potential difference between the inside and the outside of the membrane, also known as the resting potential, is around -65mV [7].

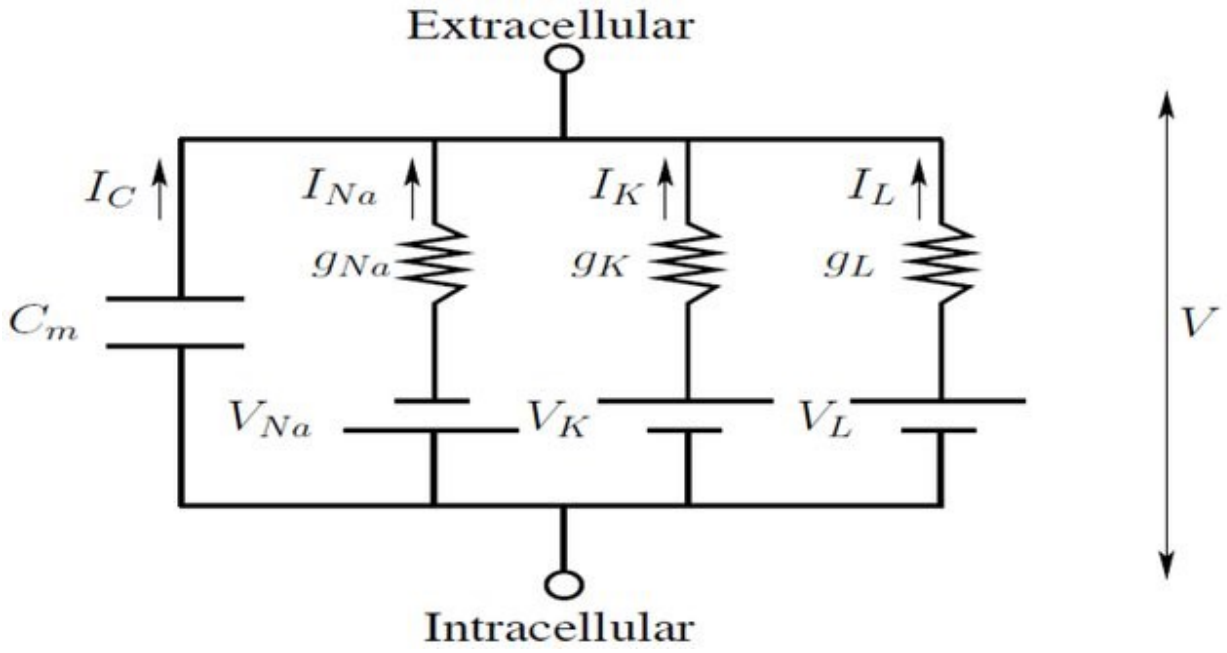

Figure I.1 Circuit diagram of a Hodgkin-Huxley model of the neuron.

Cellular membrane potential is modeled as voltage potential across circuit with currents representing major ion flow and voltage sources representing the steady state voltage contribution of each ion concentration gradient. The capacitance models the capacitive property of cellular membrane.

Action potentials are a transient deviation from resting potential and are considered to represent information bits conveyed, integrated and processed in the brain. The generation of action potentials requires an input signal to cause membrane voltage to exceed a certain threshold value [8]. Once the membrane potential of a neuron reaches the threshold, the amplitude and the duration of the resulting voltage change is the same independent of the properties of incoming signal. This stems from the nonlinear, voltage dependent dynamics of the ion channels. At the resting state, voltage-gated Na+ and K+ channels are in a closed state but the transient increase in the membrane potential, called depolarization, due to the input signal opens Na+ channels, which results in the influx of the Na+ ions down their concentration gradients. If the membrane potential reaches a certain voltage, Na+ ion channels open fully allowing a large Na+ influx that depolarizes the neuron rapidly, generating an action potential [9,10]. Due to the high membrane potential resulting from this influx, Na+ channels block and K+ channels open, leading to the outflow of the K+ ions and a sharp decrease of the membrane potential. The return to resting potential leads to closing of K+ channels and resetting of Na+ channels to a close state marking the end of a unitary neuronal response.

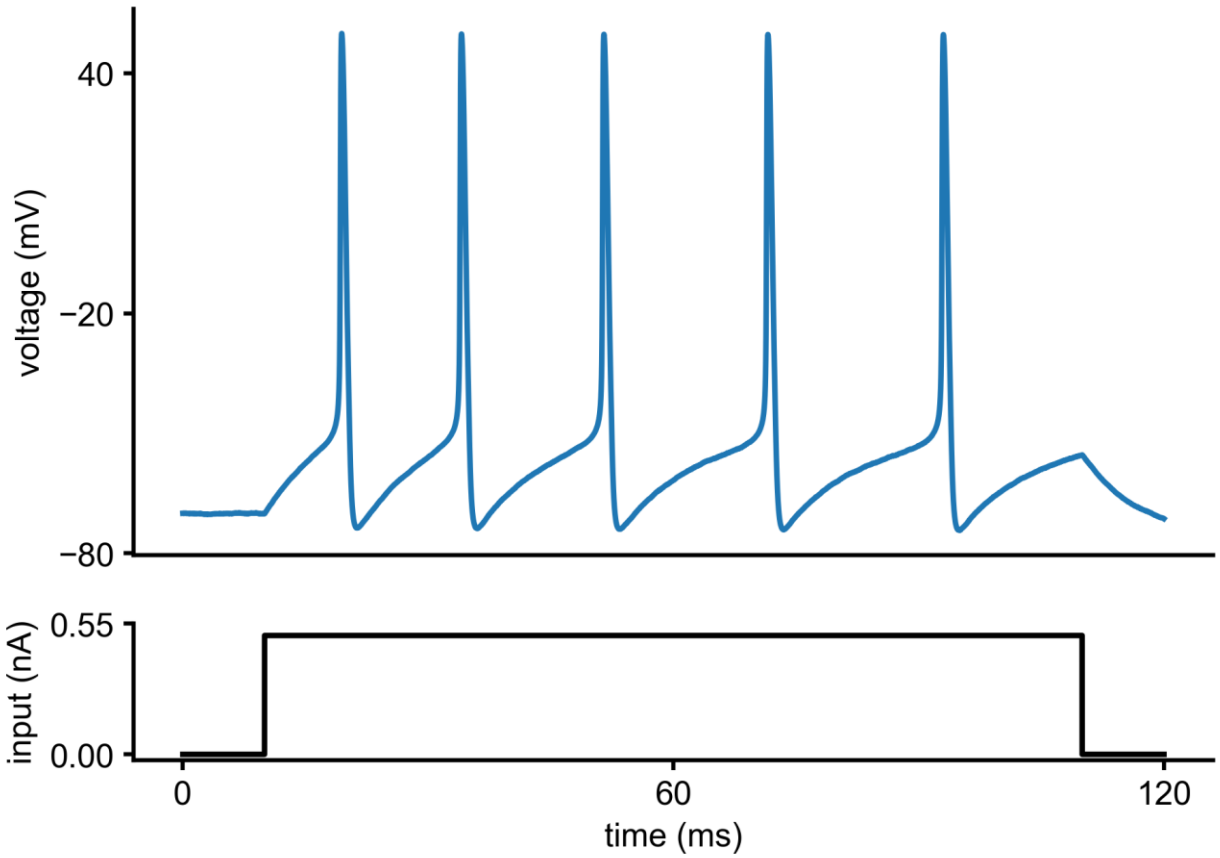

Figure I.2 Voltage profile of a Hodgkin-Huxley neuron under external input.

(Top) Computer simulated time course of neuron membrane potential using Hodgkin Huxley model. Voltage profile exhibits a periodic nonlinear response to input that is characterized by an initial slow depolarization followed by a sharp spike. (Bottom) Time course of input current. Input profile is modeled as a step function impulse. The start and end of the impulse corresponds to the onset and quiescence of voltage spikes.

1.1.3 Formal Modeling of Neural Activity

This basic understanding of action potential generation allows for mathematical modeling of neuron responses. A standard way to mathematically model a neuron is to represent a patch of the neural membrane as an electrical circuit with capacitance based on the capacitive properties of the membrane, resistors for each type of ionic current and voltage sources relating to concentration gradients for each ion species (Figure I.1) [11,12]. This framework allows for membrane potential to be represented by a system of differential equations in a framework first introduced by Hodgkin and Huxley [9].The Hodgkin-Huxley equations incorporate the voltage induced conductance changes of ionic currents by modelling gating variables specific to each type of ion channel [13].

In the Hodgkin-Huxley model, the neural membrane potential evolves according to:

$$c_m \frac{dV_i}{dt} = I_{syn,i} + I_{ext,i} - m^3\, h g_{Na}(V_i - E_{Na}) - n^4 g_K(V_i - E_K) \qquad \text{(I. 1)}$$

$$-g_L(V_i - E_L),$$

where g_x is the maximal conductance associated with an ionic current, E_x is the reversal potential for an ionic current, $I_{ext,i}$ is a direct current applied to each neuron and $I_{syn,i}$ represents the synaptic current to the neuron. The ionic current gating variables *h*, *n*, and *m* obey equations of the form

$$\frac{dx}{dt} = \frac{(x_\infty(V) - x)}{\tau_x(V)} \qquad \text{(I.2)}$$

where $x_\infty(V)$ is the voltage-dependent, steady state activation function for the gating variable and $\tau_x(V)$ is the voltage-dependent time constant. Numerical simulation of the Hodgkin-Huxley equations replicates action potential firing in response to direct current input as shown in Figure I.2.

1.1.4 Neural Networks

In the brain, neurons do not act in isolation. Each neuron is connected to other neurons forming a complex information processing network. About 60 years ago MuCulloch and Pitts showed that even a highly simplified, binary model of a neuron is capable of executing logical computations when arranged in a connected network [14]. In the brain, the connection between neurons occurs at the synapses that bridge the axon terminal and dendrite of a presynaptic and post synaptic neuron, respectively. When a presynaptic neuron fires, it induces an ionic current in the post synaptic cell that changes its membrane potential which can lead to the dynamic firing process. As a neuron can receive many (up to 10000) inputs from other cells, it processes these inputs through non-linear summation. Thus this integration of inputs from a set of presynaptic neurons by a single post synaptic neuron can allow for complex dynamic firing patterns to emerge [15,16].

In very general terms, the structure of neural networks in the nervous system ranges from dense locally connected networks to complex long-range connections with specialized functionality. In locally connected networks, many different topological archetypes can manifest varying with the functional demands. The most basic connectivity architecture is

often approximated as randomly connected neurons where neurons connect to each other independent of their specific relative locations while varying in density of connections as well as range of connectivity. In addition to random networks, another common archetype consists of networks that exhibit similarity to the features of small world networks [17] or networks that maximize physical clustering (the probability that cells connected to a common neuron are also connected to each other) while minimizing the mean path length (the average number of connections between each pair of neurons in the network). In other cases specialized networks can be uniquely attributed to certain behavioral and cognitive responses [18].

Synaptic connections between neurons aren't fixed, however. New external experiences and/or intrinsic computations result in formation of new synapses, or strengthening/weakening of existing synaptic connections implying functionally dynamic relationships between neurons in a network. The process underlying this variation in connectivity was captured originally in a framework proposed by Donald Hebb, who suggested that when pre and post synaptic neurons are coactive their connectivity strength increases such that neurons that "fire together wire together"[19]. Experimental work has validated this principle and discovered that both the firing co-activity as well as relative timing of pre and post synaptic spikes can determine the direction and magnitude of changes in synaptic strength[20,21]. Such changes in neural connectivity, referred to as synaptic plasticity, are thought to be the source of the brain's adaptability as well as the key to understanding memory formation [22,23].

Functional vs Anatomical Connectivity in the Brain

Although anatomical connections between neurons provide direct insight into network structure, functional connections, based on coactivity of neural groups and brain regions, can occur without anatomical evidence of direct connectivity. This functional connectivity can be inferred on various time scales. For example, when single neural spike resolution is available, correlations between the spike times of two neurons can be used to infer whether the neurons are functionally connected and in some cases whether this connection directional (i.e., causal). When considering functional connectivity across larger domains, imaging tools, like FMRI, can detect whether different brain regions are functionally connected in specialized cognitive tasks[24].

1.1.5 Neural Oscillations

Spiking of many individual, interconnected neurons across the brain, organize on the network level into complex dynamic patterns across various spatial and temporal scales. This spatio-temporal dynamics is thought to underlie cognitive phenomena in in the brain as well as its functional pathologies. This dynamics can range from ensembles of neurons firing with widely different frequency profiles, to highly synchronous bursts of activity across the local network.

One of the important brain activity patterns that is a direct result of synaptic connectivity among neurons are neural oscillations or rhythms. Rhythmicity in neural activity has been observed as early as the 1920s when Hans Berger introduced the earliest implementation of the EEG. This rhythmicity, or neural oscillations, can be observed both at the scalp, by EEG measurements, as well as in brain tissue by local field potential (LFP)

measurements and was shown to be a result of synchronization, on various timescales, in firing within and across neural ensembles [25–27]. Because neural oscillations are a measure of coherent variations in neural firing they has provided some of the earliest insights into nervous system function.

Neural oscillatory activity is commonly grouped into specific rhythm bands, defined by the frequency content of the predominate signal. For example, EEG frequency content changes drastically during the transition between sleep and awake states [28,29]. During wake, EEG signals demonstrate high frequency oscillatory behavior characterized as beta and gamma waves, with oscillations in the 12-30 Hz and 25-100 Hz range, respectively, with specific frequency content varying based on brain region, behavioral patterns and cognitive demands [30–32]. Alpha oscillations (8–12 Hz) are most prominent around the occipital cortical area when the eyes are closed. Large-amplitude theta oscillations (4–10 Hz) dominate the hippocampal-entorhinal system during spatial navigation and memory processing. Delta waves (0.5–1.5 Hz), the largest-amplitude waves in the neocortex (the cerebral cortex region associated with sight and hearing), are present during non-REM sleep. Beta rhythms (13–30 Hz) are present throughout the motor system in the absence of movement, while transient beta oscillations (or sleep spindles) are present in the thalamocortical system during the early stages of sleep. Gamma oscillations (30–120 Hz) are present in nearly all structures and all brain states, although they dominate in the aroused, attentive brain. The transient ripple pattern (130–200 Hz), most prominent in the hippocampus, serves to transfer memories and action

plans from the hippocampus to the neocortex. These and other rhythms can temporally coexist in the same or in different structures and interact with each other [33,34].

In addition to their association with different physiological/cognitive states, neural oscillations are thought to underlie the integration or binding of spatially distributed neural responses corresponding to features of the same object or specific tasks. The act of binding is thought to happen through synchronization of neurons through oscillatory firing activity incorporating specific groups of neurons [33,35,36]. The dynamic nature of neural oscillations allows for temporary coherent oscillatory firing among different groups of neurons that can change with the specific object or task. For example, synchronous firing in the Beta and Gamma frequency bands has been correlated with the process of feature binding [37,38] as well as with the persistent activation of neural responses during memory formation and working memory activation [38,39].

1.1.6 Mechanisms of Neural Synchrony

Although EEG recorded neural oscillations have a longer history of study, invasive recording techniques have demonstrated the presence of oscillatory activity at the single neuron level [40]. Several theoretical studies have contributed to our understanding of how periodic rhythms can result from neuron-neuron interactions. There is a number of known mechanisms underlying formation of synchronous oscillatory dynamics in the brain, ranging from coherent input into/from various brain modalities, direct excitatory coupling, cellular resonance, or interaction between inhibitory and/or inhibitory or excitatory cell populations[41,42]. Examples of the latter are the mechanisms underlying gamma oscillations. Two key mechanisms which can produce gamma band oscillations, for example, are the “interneuronal network gamma” (ING) mechanism and the

“pyramidal—interneuronal network gamma” (PING) mechanism [25,43]. In the ING mechanism if two mutually inhibitory neurons are coupled they cause mutual suppression when firing. This can lead to zero lag synchronization of their firing in the gamma range that occurs due to the fact that each neuron preferentially fires after its synaptic inhibition wanes.

In the PING mechanism, AMPA-mediated projections of excitatory cells onto inhibitory cells provide fast excitation and promote inhibitory firing. These inhibitory cells, in turn, provide fast inhibition to the excitatory cells through GABAergic synapses and inhibit firing. When the inhibition to the excitatory cells wears off, the excitatory cells fire. The excitatory firing results, a short delay later, in inhibitory firing, thus bringing the network into an oscillatory rhythm of firing.The generation of neural oscillations from neuron-neuron interactions remains a current area of study [31,32].

1.1.7 Synchronization and Plasticity

One primary role of neural oscillations is proposed to be the binding of features and consolidation of memory. In the case of consolidation, synchronization enables activity-dependent modification of synaptic connections [44,45].The combination of synchronization and synaptic plasticity, via spike timing dependent plasticity (STDP), is thought to underlie the stabilization of neural assemblies that correspond to integrated experiences as the probability of spontaneous synchronization increases for groups of neurons that previously engaged in context dependent synchronous firing [46].

Therefore, these changes in synchronization appear to depend on the phase relations of the oscillations under different conditions. The precise timing necessary for potentiation is evident in many experimental paradigms and can be observed in experiments that show potentiation resulting in cortical slices when an EPSP from a presynaptic neuron precedes firing in the postsynaptic neuron within a window of 10ms. This changes to long-term depression when the firing order is reversed [47].

1.2 Neuromodulation and Nervous System Function

Neuromodulators are chemicals found throughout the nervous system that have complex effects on neurons and their synaptic interactions [26]. They generally regulate large populations of neurons with nonlinear effects on their response to input as well as the steady state characteristics of these neurons [48–50]. The concentration of neuromodulators throughout the nervous system is often regulated by neuro-modulatory systems, or groups of neurons that project throughout the nervous system and control the influence of different neuromodulators. The role and function of different neuromodulatory systems are often determined by exploring behavioral and cognitive outcomes by perturbing neural pathways involved in the system as well as exploring the effects of varying the concentration of the neuromodulator in different regions of the nervous system.

Dopaminergic neurons, for example, originate from different regions in the brain including the substantia nigra and ventral tegmentum and act on dopamine receptors through

dopamine binding [51]. The dropout of dopamine receptors is commonly observed to cause problems with motor coordination and is believed to be the mechanistic cause in Parkinson's. Similarly, in animal experiments removing the ventral tegmental dopamine systems can lead to starvation even in the presence of food [52–55].

The serotonin system, another major neuro-modulatory system, originates in the dorsal raphe nucleus and projects to receptors in the cerebellum as well as other regions including the thalamus, striatum, amygdala and hippocampus. The regulation of serotonin has been shown to have an important impact on mood and is why SSRI's (selective serotonin reuptake inhibitors) are often used to treat mood disorders such as depression [53,56,57]. Adrenergic neurons, neurons that play a role in noradrenaline regulation, originate in the Locus coeruleus (LC) and project to different targets including the hypothalamus, hippocampus, amygdala and thalamus among others [58,59]. Noradrenaline is released during many cognitive processes associated with increased attention including the formation and retrieval of working and long term memory and well as increases in response to sensory input [58].

Another well studied neuro-modulatory system is the cholinergic system which is responsible for the regulation of ACh effects. To start, acetylcholine (ACh) is a molecule that serves as both a neurotransmitter and neuromodulator and plays a prominent role in cognitive functions throughout the brain including in attention and memory. Cholinergic neurons, neurons that produce ACh, are found throughout the brain and are highly concentrated in the striatum, basal forebrain and brain stem and can project to distal

regions of the nervous system [60]. ACh is also known to play a role in the control of autonomic functions and has been implicated in homeostatic regulations of metabolism and body temperature [61]. Furthermore, the amygdala and hypothalamus receive cholinergic projections which can explain the changes in amygdala activity in mood disorders and, supporting that, ACh plays a strong role in mood regulation and depression [62–64] as well as the consolidation of long term memories [65]. The effects of ACh can therefore be implicated in a wide variety of cognitive process due to its distributed effects throughout the brain. We primarily focus on acetylcholine in this thesis because we seek to understand the cholinergic effects on memory formation as well as the interaction of the cholinergic system and inhalation anesthesia.

Mechanistically, ACh is an important regulator of neural excitability [66]. Acetylcholine affects neuron function by altering the synaptic input and cell membrane properties through both muscarinic and nicotinic acetylcholine receptor activation, the two main types of acetylcholine receptors. Within the nicotinic class of receptors there are the N1 and N2 types, where N1 is primarily found between the neuromuscular junctions while N2 is found in the brain, autonomic and parasympathetic nervous system. Nicotinic acetylcholine receptors are activated by nicotine and, through the act of ACh binding, can facilitate the passage of ions into the cellular membrane. In general the purpose of the N-type ACh receptors is to mediate fast synaptic transmission of nerve impulses[67]. In the hippocampus, nicotinic influence on excitatory synaptic transmission has been observed in the path from CA3 to the entorhinal cortex [68]. Furthermore, in thalamocortical slice preparations of somatosensory cortex [69], activation of nicotinic receptors leads to

increased thalamic input response. Nicotinic effects of glutamatergic transmission have also been shown at the medial dorsal thalamic input to prefrontal cortex [70].

Muscarinic receptors are the other primary acetylcholine receptor class and are of interest to us as they form an important component of the core model we use throughout this thesis. Muscarinic receptors are a type of G-protein coupled receptor that is found in the brain, the heart and in smooth muscles with 5 subtypes that can be both excitatory and inhibitory. The distribution of muscarinic acetylcholine receptors (mAChRs) has been shown to vary across cortical layers, cell types, and brain regions [71–73]. ACh modulates the excitability, or response to input, of neurons through its interaction with the muscarinic receptor system, which activates a G-protein signaling cascade [74]. The Muscarinic acetylcholine system serves to mediate a slow metabolic response in target neurons, an example of which is the slow m-type repolarizing potassium current, or m-current to modulate cellular firing behavior as discussed in chapter 1.3.

1.3 Exploring Effects of M1 ACh Receptor Activation on Neuron Excitability and Firing Behavior through Computational Modeling.

ACh modulation of the m-current exerts continuous control of neuronal excitability properties. The K+ ion channels influenced by muscarinic M1 receptor activation, and their corresponding ionic current, are blocked when ACh is high and are responsible for a switch in membrane excitability type [75]. Drawing on the physiological underpinnings of cholinergic modulation, a wealth of mathematical and computational research has been dedicated to understanding how ACh changes neural spiking behavior [33]. We build

upon this research by using a neuron model that accounts for the effects of ACh in the Hodgkin-Huxley model formalism through the addition of a separate current I_M which captures the dynamical effects of the K+ m-current. We will refer to this model throughout the text as the Ks model. In the Ks model, the effects of ACh are simulated by decreasing the value of the maximal conductance of the K+ m-current, $\bar{g}_{Ks}$, such that low values of $\bar{g}_{Ks}$ correspond to high ACh tone and high values of $\bar{g}_{Ks}$ correspond to low ACh tone.

1.3.1 ACh Facilitates a Transition between Type 1 and Type 2 Excitability Types

The mathematical framing of neural spiking behavior allows for us to capture many of the dynamical changes to the neuron as a result of the m-current. Acetylcholine changes the response of the neuron to input such that for high and low levels of acetylcholine the neuron excitability changes between two archetypes: Type 1 and Type 2, respectively. These two excitability types differ in the dynamical mechanism of spike generation [76]. Because low levels of ACh allow for an increase in the hyperpolarizing m-current, Type 2 (low ACh) neurons have increased competition between depolarizing and hyperpolarizing currents which must be overcome to initiate a spike, while Type 1 (high ACh) neurons do not. This leads to several differences in input response characteristics between the two types, including a change in frequency and spike timings response to different current inputs.

The ACh-induced change in neuron spike rate can be traced back to the effects of the m-current which directly affects firing frequency. In terms of spike frequency, response to an injected current (f/I or gain function) [77], both excitability types (Type 1 and Type 2) have a critical current, I_c, below which no spiking occurs, but are quite different in terms of

spiking response around this point. Type 1 (high ACh) neurons will fire at arbitrarily small frequencies as the critical value of I_c is reached leading to a continuous frequency-current curve, whereas Type 2 (high ACh) neurons have a discontinuous frequency increase from quiescence and initiate firing at a higher frequency (Figure I.3 A). Another critical feature difference between Type 1 and Type 2 neurons is that Type 2 neurons vary their firing rate much less in response to changes in injected current, or have reduced gain[77]. The difference in gain between these neuron types leads to larger differences in firing rates between cells receiving different inputs in Type 1 (high ACh) networks compared to Type 2 (low ACh) networks.

A concurrent change in response characteristics that occurs with ACh activation of the ion channels associated with the M-current is differential response to brief and weak stimuli in terms of spike timing perturbation (i.e. advance or delay). This cellular property is quantified by the phase response curve (PRC)[78–82]. The PRC is measured, both experimentally and numerically, by driving a neuron to fire at a stable periodic frequency and delivering small, brief, and depolarizing perturbations between its spikes, at different timings (phases) within the spiking cycle. In response to these perturbations the timing of the following spike will be earlier, later, or the same as an unperturbed period (Figure I.3 D,E). Type 1 and Type 2 neurons display significant differences in PRC shape. A Type 1 PRC is uniformly positive, meaning that perturbations will always advance the timing of the next spike. Type 2 neurons have a biphasic PRC, meaning that depending on the timing of the perturbation it will either advance or delay the next spike. The biphasic character of the Type 2 PRC allows these neurons to synchronize spike firing due to the

ability to either shorten or elongate the period, with zero value of phase response becoming a stable fixed point of the dynamics.

In addition to controlling the initial membrane response to input, the ACh-induced changes in m-current also regulate spike-frequency adaptation (SFA) over the time course of sustained input [83]. SFA effectively represents a negative feedback on neuronal firing and is frequently due to a hyperpolarizing current that builds up as a neuron fires action potentials. Here, the m-current acts as an adaptation current and its blockade in high ACh conditions causes a significant reduction in SFA (Figure I.3 B&C). The effects of SFA and gain modulation are related by the fact the neuronal gain reflects the firing rate of a neuron when the m-current has saturated. Here we refer to SFA as the short-time scale effect of reducing the frequency of a neuron as it fires, possibly terminating a burst of firing.

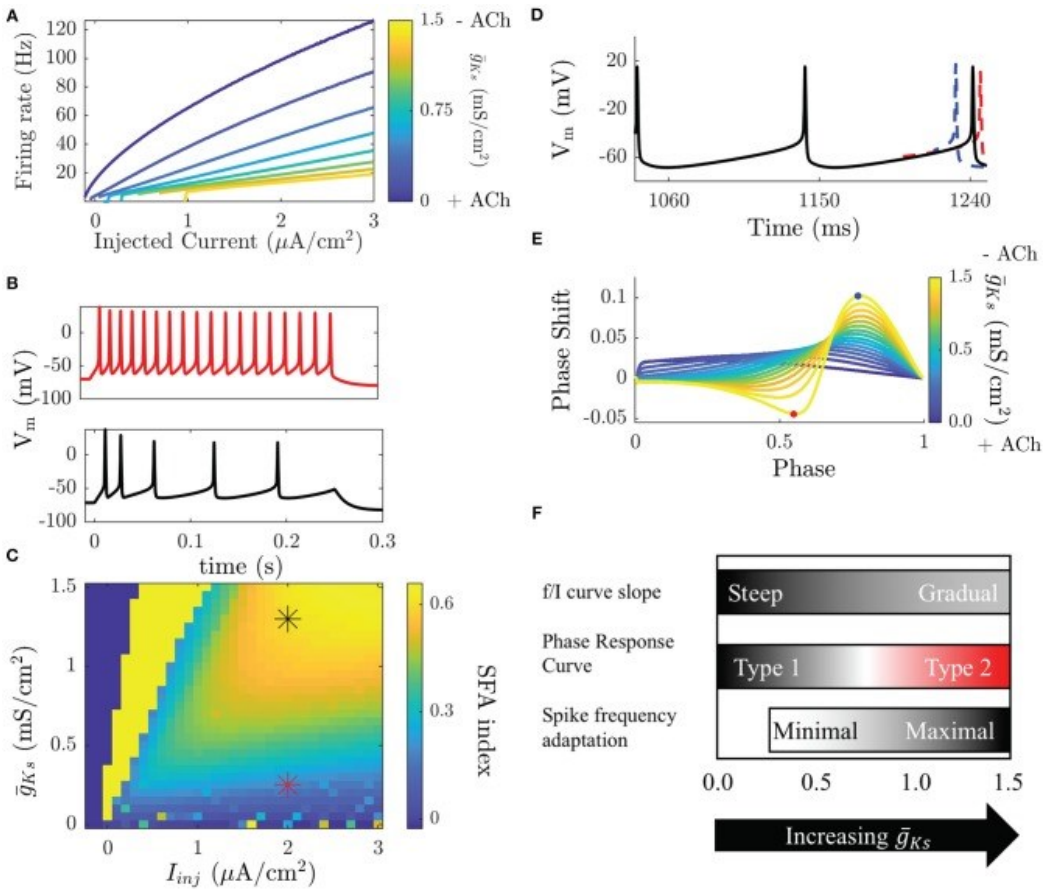

Figure I.3 Modulation of neuronal properties in a model of cholinergic modulation.

(A) The f/I curve increases its slope as ACh increases (g_{Ks} decreases). Blue colors represent the high ACh case. The onset of spike frequency adaptation in the Ks model occurs at a high g_{Ks}. SFA is quantified here by the SFA index, which compares the inter-spike interval between the first two and the last two spikes in an induced burst. (**B**, top) When g_{Ks} is low SFA is minimal and ISIs are equivalent throughout the burst. (**B**, bottom) When g_{Ks} is high ISIs gradually increase though out the burst. **(C)** Measured SFA indices for various g_{Ks} and injected current values show that SFA is only significantly reducing frequency during the burst above g_{Ks} = 0.25 mS/cm2, below this the effects are negligible. Stars indicate the parameters of the voltage traces shown in **(B)**. Dark blue squares indicate parameters that do not elicit spikes and bright yellow squares parameters that yield <3 spikes. **(D)** The PRC is measured by comparing perturbed vs. unperturbed periods when neurons fire at a fixed frequency. When the next spike is earlier the phase response is positive (blue), when it is delayed it is negative (red). **(E)** Type 1 neurons have a strictly positive PRC (blue) while Type 2 neurons have a biphasic PRC. **(F)** Transitions in biophysical properties in the Ks model occur over different ranges of g_{Ks}. Modulation of the f/I slope occurs continuously over the range of g_{Ks}. The slope is steep for low g_{Ks} and gradual for high g_{Ks}. The transition between a Type 1 and a Type 2 PRC occurs for high g_{Ks}, though the PRC shape does change in a continuous manner as g_{Ks} changes. SFA has little effect for low g_{Ks} and only significantly effects the frequency of neurons for high g_{Ks}.

1.3.2 Interaction of ACh Dependent Excitability and Network Structure

For neural networks, both the intrinsic excitability of the constituent cells as well as the network structure of the synaptic connectivity can affect the overall spiking dynamics across the network. Differences in neural response can have a cascade of effects when expressed in a network as previous work has shown that the strong effects of ACh on neuron excitability lead to significant changes in network dynamics which depend highly on the network's connectivity structure.

For example, many neural structures in the brain follow connectivity that exhibit features of small world networks [17]. A small-world network is a type of mathematical graph in which most nodes are not neighbors of one another (i.e. don't share direct connection), but the neighbors of any given node are likely to be neighbors of each other and most nodes can be reached from every other node by a small number steps through existing connections. Specifically, a small-world network is defined to be a network where the typical distance L between two randomly chosen nodes (the number of steps required) grows proportionally to the logarithm of the number of nodes N in the network while the global clustering coefficient is not small. To construct small world networks in biological context, neurons are arrayed on two dimensional or ring lattices and the varied network parameters are the radius of connectivity (r; the distance across the lattice each neuron sends local outputs to) and the rewiring probability (P; the probability that a local output is exchanged for an output to a random target). Depending on the value of P, the resulting networks have either all local connections (P=0), mostly local with a few random, long range connections (P=0.2, typical small world connectivity), or completely random

connectivity (P=1). When networks of Type 1 excitatory neurons (without any inhibitory neurons) are coupled, more diversity of spike firing patterns are observed[84]. Specifically, in Type 1 excitatory networks, only networks with high connectivity radii and random structure (P close to 1) support synchronous firing patterns or network bursting. Networks composed of Type 2 neurons, on the other hand, are much less dependent on the values of r and P in the formation of synchronous dynamics. As long as r is greater than 2%, networks generate highly synchronized bursting dynamics. Overall, varying synaptic weights and neuron depolarization has a similar effect, Type 1 networks exhibit more variable firing patterns while Type 2 networks are generally synchronous[85].

Hence, ACh-induced modulation of neural excitability plays an important role in shifting between network and cellular mechanisms of pattern formation. When gain is high (the f/I curve is steep and ACh is high) variations in synaptic input will drastically modify the firing rate of a neuron and interrupt network mechanisms for synchronous firing among cells, while a shallow f/I (ACh is low) merely causes slight shifts in an internal driven period and supports network promotion of synchrony. Also an important distinction between Type 1 and Type 2 neurons that applies to these results is the difference in PRCs leading to integrator (Type 1) versus resonator (Type 2) modes of activity [76,86].

Another network connectivity scheme often encountered in the brain [18] and having strong dependence on Type 1 and Type 2 cellular dynamics is the lateral inhibition network. In general, lateral inhibition networks are formed from two lattices, one for excitatory neurons and one for inhibitory neurons where inhibitory neurons send their

outputs farther than the excitatory neurons do. When modelling this we take the extreme of this condition and have globally connected inhibitory neurons and locally connected excitatory neurons. In lateral inhibition networks, firing is usually localized to a small region of the network, called a bump. The most obvious distinction between networks with Type 1 versus Type 2 neurons is that Type 1 networks have stationary bump dynamics while Type 2 networks have moving bump dynamics [87]. This transition is due to SFA, which in the Ks neuron model results from the conductance of the m-current, g_{Ks}, that is responsible for the Type 1 to Type 2 transition. In this neuron model, the effects of SFA occur for lower g_{Ks} values than it takes to transition from Type 1 to Type 2 excitability. The transition from stationary to moving dynamics occurs because the currents responsible for SFA build up in the neurons within the bump of activity, lowering their excitability and firing frequency. As the average frequency within the bump decreases, inhibition is decreased across the network allowing neurons just outside the bump to begin firing, and for the bump to move to another region of the network.

Variations in ACh sensitivity as well as biological heterogeneities in neuronal morphology and ion channel expression can lead to networks of mixed populations of Type 1 and Type 2 neurons. When modeling excitatory networks containing an equal mix of Type 1 and Type 2 cells, removal of synapses connecting the populations drastically affects the nature of synchronous bursting dynamics [88]. The ability of Type 2 neurons to synchronize a mixed population is also seen when these cells are network hubs (i.e. cells that have a high number of random, not local outputs). In such networks, synchrony during bursting is greatly increased and is more robust to changes in the distributions of

connection probability used to generate a network structure than in Type 1 dominated networks [89].

This brief summary of effects of Ach on network dynamics lead us to believe that generally the changes in neural excitability induced by muscarinic effects of ACh may have consequences for how information may be coded in the spiking activity of neural networks. The two predominant coding strategies identified in the brain are rate coding and phase coding. Rate coding represents information in the firing rates between neurons and phase coding represents information in the time differences between neurons [25,37,90,91]. High ACh concentration, supports frequency coding via strong modulation of firing frequencies depending on the cell input. On the other hand low ACh concentration promotes neuronal synchrony and phase coding.

1.3.3 Hypothesized Role of Acetylcholine in Memory Processing

Acetylcholine is released throughout the CNS where it impacts global brain function by affecting sleep-wake cycles, attention, and memory formation. One of the functional roles of ACh is thought to be the promotion of the retrieval and formation of memories [92,93]. The hippocampus, one of the core regions implicated in memory formation, receives cholinergic projections from neurons in the medial septum [94] and its neuronal activity is modulated by activation of both nicotinic and muscarinic acetylcholine receptors. The combined effects of acetylcholine release on glutamatergic inputs and neuron function are thought to play important roles in tuning the hippocampal CA1 network for recall and the formation of new memories [66]. Low ACh allows intra-hippocampal synaptic

interactions to increase thereby promoting hippocampal output signaling and memory retrieval, whereas high ACh concentrations promote processing of inputs from outside the hippocampus allowing for the transient formation of memories in CA1 [92]. This suggests that ACh governs mechanisms of the active maintenance in working memory tasks as well as the mechanism underlying the regulation of network dynamics important in the processing of stimuli memory tasks [95].

Another important mechanism actively participating in memory consolidation, that could be mediated by changing ACh concentrations is disinhibition. Recent evidence suggests that acetylcholine has the ability to selectively activate inhibitory somatostatin positive (SST+) interneurons in the hippocampus[96,97]. This selective sensitivity is mediated by both nicotinic and muscarinic receptors expressed preferentially on the neurons[98,99]. Acetylcholine release in the hippocampus by medial septal inputs is known to be higher during wake vs. NREM sleep (with release increasing again during REM sleep) [100,101]. Aton lab tested whether gating of the hippocampal network, and CFM consolidation, are affected by manipulations of hippocampal cholinergic input. They that, similarly to the results of chemogenetic manipulation of SST+ interneuron activity, chemogenetic suppression of medial septal cholinergic neurons after CFC resulted in greater DG network activity. On the other hand, Chemogenetic activation of cholinergic inputs resulted in suppression of DG network activity[102].

One way to evaluate role of ACh in memory maintenance would be to look at the effects of increased acetylcholine on memory consolidation. This effect is in fact observed

through experimental impairments to consolidation caused by cholinergic stimulation of the medial septum after training in rats as well as when observing the effects of physostigmine (an acetylcholine antagonist) on memory consolidation in humans [103–105]. One of our aims in this thesis is to investigate a plausible dynamical underpinning of the relationships among ACh and the resultant change in network firing patterns and the implications for synaptic plasticity and memory consolidation.

1.4 Sleep, ACh and Memory Formation and Consolidation

The extent to which ACh is released throughout the forebrain is a physiological variable which is widely divergent between wake, NREM sleep and REM sleep. Understanding links between ACh release, network dynamics and role of sleep in memory consolidation may allow us to better understand the neuromodulatory effects of ACh on brain function.

1.4.1 Stages of Sleep

Wake and sleep are two distinct behavioral modes observed in nearly all mammals. Each state can be further identified by differences in EEG recorded neural activity with sleep being further decomposed into rapid eye movement (REM) sleep and three stages of non-REM (NREM) sleep [106]. REM sleep is distinguished by rapid eye movements and shares EEG activity traits with wake. NREM sleep, on the other hand, ranges from light sleep in stage N1 to the deep sleep of N3[107]. Stage N1 only lasts for a few minutes and retains the presence of muscle tone and light breathing while demonstrating distinct alpha wave EEG signatures. Stage N2 comprises 45% of sleep, during which heart rate and body temperature drop and the presence of K complexes, which are prominent transient

Delta wave signatures, can be detected in the EEG[108]. Stage N3 is deep sleep, or slow wave sleep, with dominant Delta EEG activity, is associated with a high arousal threshold[109–111] and is when the body engages in repair. Activity of the different neuromodulatory systems also varies across sleep and wake states. All neuromodulators are at high levels during wake states and drop to lower levels in NREM sleep states. Norepinephrine, serotonin and dopamine remain low during REM sleep but ACh rises to high levels during REM sleep, to levels even higher than observed in the wake state in some brain regions[112].

1.4.2 Role of ACh in Neural Oscillations during Sleep Stages

Sleep has been implicated in promoting synaptic plasticity and memory consolidation [113–115]. Additionally, there is a wealth of research that focuses on how ACh influences network oscillations and as such modulates synaptic plasticity[116–118]. The differential activation of cholinergic neurons across REM and NREM sleep states contributes to the differences in neurological activity in these states. For this reason it is plausible that the dynamic changes in neurological activity induced by ACh are mechanistically integral to the neurological processes that occur during sleep. Hypothetically, the transition to oscillatory dynamics between wake and sleep could constitute the change in bias between rate coding (useful during initial learning) and phase coding (which may promote consolidation). In this thesis we elucidate how the spiking dynamics that are associated with Type 1 and Type 2 excitability interact with synaptic plasticity rules to modulate synaptic strengths within networks by taking advantage of network oscillatory activity.

1.4.3 Memory Consolidation and NREM Sleep

How the brain binds various sensory features of life events into a neural representation for memory storage is a long-standing question in neuroscience. Available data suggest that initial memory encoding is driven by increases in activity (rate coding) among a specific population of neurons, often referred to as “engram neurons”[119–122]. Over time, these mnemonic representations are incorporated into more widely distributed networks in a process referred to as systems memory consolidation [123–125]. A critical unanswered question is how heterogeneous neural populations, distributed across the brain over vast synaptic distances, cooperate in the process of long-term memory storage. Recent experimental findings show that, specifically during NREM sleep, slow oscillations and sharp waves, with ripples associated with them, promote temporal segregation between neurons with high intrinsic firing rates during wake and those firing less frequently, with the former leading the latter [53,124,126] . At the same time, slow oscillatory patterning of neuronal firing during sleep has been implicated in promoting synaptic plasticity and memory storage [114,127–131]. Network oscillations that are present in brain circuits during sleep have been implicated in promoting STDP by precisely timing the firing between pairs of neurons[128].

We will show that a NREM sleep-like state associated with low ACh conditions drives network dynamics to change the bias between information coding schemes–a transition which occurs naturally through the sleep-wake cycle. Through this switch, functional network structures associated with engrams may become more stable and robust for long-term information storage.

1.5 Anesthesia Effects on the Nervous System and Interactions with Acetylcholine.

1.5.1 Cellular Mechanisms of Anesthesia

Anesthesia is a pharmacological procedure that is used extensively in the medical profession. The goal of anesthesia is typically to suppress the patient's conscious awareness, stress and pain associated with surgery. Several putative mechanisms have been proposed as to how anesthetic agents induce loss of awareness or consciousness, however the variety of effects of different anesthetic agents within the central nervous system make this an active area of study. Experimental studies implicate the brainstem, thalamus, and cortex as regions where neuronal activity is heavily modified by general anesthesia [132,133]. However, the primary target region likely depends on the type of anesthetic [134]. At the single cell level, common inhalational anesthetics facilitate inhibitory transmission and suppress excitatory synaptic transmission [135,136]. However, the extent of effects on specific synaptic receptors varies across different anesthetics (Figure I.4).

Despite such differences in direct effects of different anesthetic agents, an underlying implicit hypothesis exists that there is an anesthetic agent-invariant mechanism that accounts for their final effect, the loss of awareness or consciousness. Proposed neural correlates of anesthetic action include modulation of neuronal excitability, increased network synchrony [137], disrupted brain functional connectivity and deficits in information integration [138,139]. Integrated Information Theory is one of the leading theories of consciousness providing a general framework for how attention and awareness can be

attributed to transfer and processing of information within a system [140]. Supporting this view, experimental studies have shown that information theoretic metrics of brain activity are reduced during anesthesia associated with suppressed behavioral signs of consciousness [141].

1.5.2 Cholinergic Interactions with Anesthesia

In both humans and rodent model, interventions that raise ACh concentration in the brain are associated with a reversal of anesthetic traits or a reduction in anesthetic potency[142]. Conversely, lesions of cholinergic neurons in the basal forebrain—the main source of acetylcholine for the cortex—reduce anesthetic requirements for commonly used drugs such as isoflurane and propofol [143].

Furthermore, many investigations using pharmacological, electrical, or optogenetic stimulation of various brain regions to counter or reverse the unconscious state in humans and animals under the continued presence of anesthetic [144–147] have utilized nicotinic [148] or muscarinic [149] cholinergic interventions. Recently, reverse dialysis delivery of the acetylcholine agonist carbachol was used to successfully reverse the effect of sevoflurane in rats *in vivo* [150]. Similar effects were observed *in vitro* when bathing cortical slices with cholinergic and noradrenergic agonists led to a reversal of slow wave oscillations induced by anesthesia [151]. These studies have shown that various behavioral expressions of the conscious state can be restored by exogenous cholinergic interventions that counter the pharmacological effect of anesthetics. Less investigated, however, is the question of whether the brain's electrophysiological activity, particularly

in cortical areas that are chiefly responsible for conscious representations, are also restored to pre-anesthetic levels and quality by such interventions. In other words, how do cortical neuronal activity patterns compare before anesthesia, during anesthesia and after conscious-like behavior is restored by exogenous stimulation while still in the presence of the anesthetic?

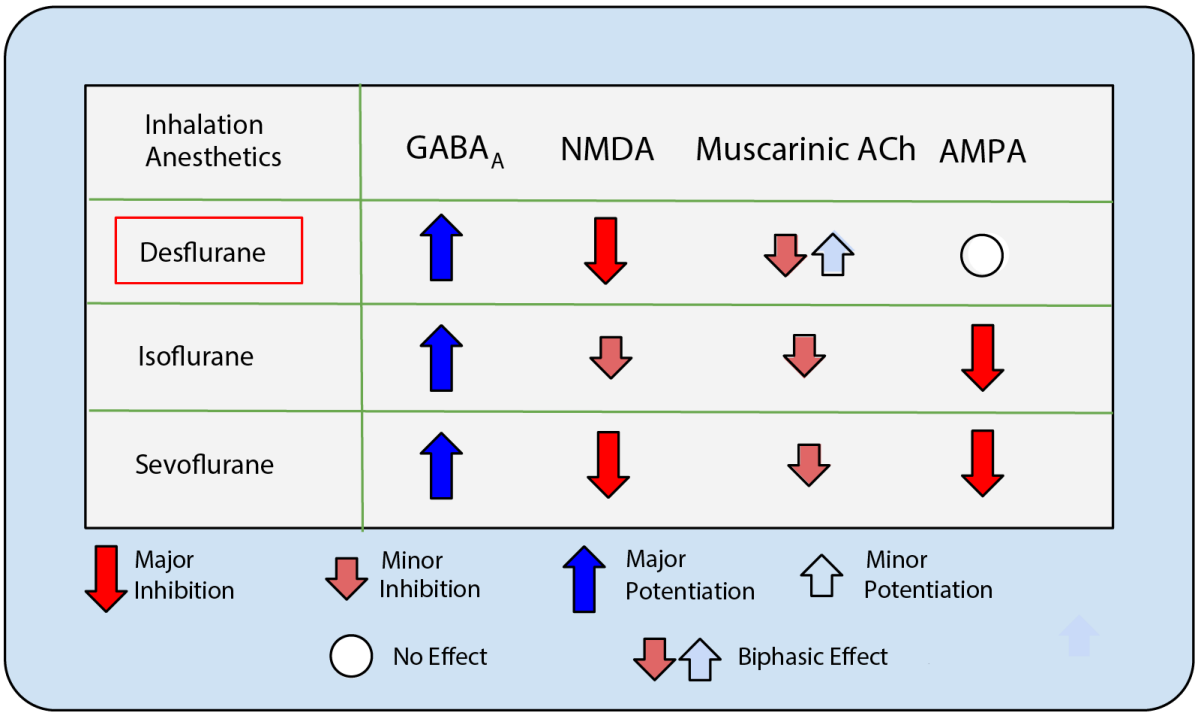

Figure I.4 Common inhalation anesthetics have similar effects on synaptic receptors.

Experimental findings show similar effects across inhalation anesthetics on synaptic receptors [152–155]. Binding to inhibitory $GABA_A$ receptors is commonly potentiated while NMDA receptor activity is commonly inhibited with the magnitude of effect varying between anesthetics. Activation of muscarinic acetylcholine receptors and AMPA receptors is inhibited by isoflurane and sevoflurane while desflurane has a biphasic effect and null effect on muscarinic acetylcholine and AMPA receptors, respectively.

1.6 Overview

The goal of this thesis is to understand the role of acetylcholine, through its influence on the m-current, on brain states and function. Specifically, we use computational modeling to analyze its role in information coding, its effects on memory formation and its influence on the states of anesthesia.Our modeling work uses a Hodgkin-Huxley conductance based neuron model with the addition of a slow potassium current, the Ks model, to simulate cholinergic modulation[76], the details of which are introduced in Chapter 2. This biophysical model emulates muscarinic receptor mediated cholinergic effects on neural membrane potential by blocking the m-current. As discussed above, ACh modulation of the slow m-type potassium conductance, g_{Ks}, is responsible for the transition from Type 1 to Type 2 excitability [84,85,87,89,156].

In Chapter 2, we investigate how ACh mediated transitioning neurons from Type 1 to Type 2 excitability impacts the patterns of neural activity that can represent information within a network. We argue that this neural excitability transition enables a dynamic switch between rate coding and phase coding as levels of ACh release change. To investigate our hypothesis, we consider different network structures and external input patterns and show that correlations in frequency between pairs of neurons for Type 1 networks and correlations in phase locking for Type 2 networks were more similar on repeated simulations of the same structural realization of networks when compared to different structural realizations. These effects were not observed when reversed the paradigm and we measured phase relations in Type 1 networks and frequency responses in Type 2 networks. Similar results were observed for fixed network conditions when different input

current patterns were tested. Moreover, we found functional mapping between frequency representations in Type 1 networks and phase representations in Type 2 networks. These results lead us to formulate a hypothesis that ACh mediates coding shift from frequency coding (high ACh concentration) to phase coding (low ACh concentration).

In Chapter 3, we use a similar model framework together with spike timing dependent plasticity to investigate how ACh mediates network reorganization during sleep dependent memory consolidation. We show that regulation of neuronal excitability, mediated via muscarinic ACh pathway, that are analogous to those occurring in NREM sleep, drives changes in network-wide oscillatory properties, recreating a number of experimentally-observed phenomena. We specifically show that the experimentally observed network reorganization, can be mediated by network transition between rate coding (during a wake-like state) and phase coding (during a NREM-like state). Namely, NREM phase coding drives STDP between neurons which causes dramatic, differential changes in the strength of reciprocal connections between highly active vs. sparsely firing neuronal populations. These changes lead to differential changes in firing rate in the two populations. Together, our results show that the NREM-like state associated with low ACh conditions drives network dynamics to change bias between information coding schemes–a transition which occurs naturally through the sleep-wake cycle.

In Chapter 4, we model the synaptic induced effects of anesthesia and investigate the role of ACh in anesthetic effects as well as the potential for ACh to mitigate effects of anesthesia. To do this we simulated an excitatory-inhibitory (E-I) neuron network

consisting of the Hodgkin-Huxley Ks model neurons with glutamatergic, GABAergic and cholinergic inputs. We model the effects of desflurane, a common inhalation anesthetic, by varying the effect of excitatory and inhibitory neurotransmitters in a manner consistent with experimentally observed effects of desflurane at the synaptic level. To fit the model to experimentally obtained measures of *in vivo* visual cortex network firing activity at different concentrations of desflurane, we applied a differential evolution algorithm to optimize parameters modulating the effect of neurotransmitter binding at different receptors. Specifically, we quantified the graded, concentration-dependent effect of simulated anesthetic on neuronal firing rate distributions, phase coherence, monosynaptic spike transmission, network functional connectivity, and information theoretic measures of neuronal interactions, and fit these measures to corresponding experimentally measured quantities in the rodent visual cortex *in vivo*. We then used the model to simulate the presumed effect of cholinergic activation, without changing parameters for the simulated anesthetic-induced synaptic alterations, to see if these measures were reversible to near pre-anesthetic levels. Our model results provide insight into the mechanisms by which distinct neurotransmitter systems shape network behavior under the combined influence of complex pharmacological interventions that may affect the state of consciousness.

Finally, in Chapter 5, we revisit our main results to better contextualize the varied effects of ACh on neural activity and how ACh impacts different cognitive processes. We further assess the limitations of our methodology as well as how these limitations can be addressed and the methodology expanded in future research endeavors.

Chapter II

Acetylcholine Mediates Dynamic Switching Between Information Coding Schemes in Neuronal Networks

2.1 Introduction

As discussed in Chapter 1, rate coding and phase coding are the two major coding modes seen in the brain. For these two modes, network dynamics must either have a wide distribution of frequencies for rate coding, or a narrow one to achieve stability in phase dynamics for phase coding. Acetylcholine (ACh) is a potent regulator of neural excitability. Acting through the muscarinic receptor, ACh reduces the magnitude of the potassium M-current, a hyperpolarizing current that builds up as neurons fire. The M-current contributes to several excitability features of neurons, becoming a major player in facilitating the transition between Type 1 and Type 2 excitability. In this chapter, we argue that this transition enables a dynamic switch between rate coding and phase coding as levels of ACh release change. Specifically, when a network is in a high ACh state variations in synaptic inputs will lead to a wider distribution of firing rates across the network and this distribution will reflect the network structure or pattern of external input to the network. When ACh is low, network frequencies become narrowly distributed and the structure of a network or pattern of external inputs will be represented through phase relationships

between firing neurons. This work provides insights into how modulation of neuronal response properties influences network dynamics and information processing across neuromodulatory states.

This work was completed with multiple coauthors. In this study I conducted the network simulations and statistical analysis of model results to measure how input and network structure is represented through frequency and phase correlations. The article discribing these results was published in Frontiers in Systems Neuroscience [157].

2.2 Methods

2.2.1 Model Design and Network Connectivity

Networks were composed 300 excitatory and 75 inhibitory neurons arrayed on two interconnected ring lattices. Excitatory neurons were randomly connected to 3% of the neurons on each lattice, while inhibitory neurons were connected to 6%. The random process used in the generation of a network structure was seeded such that one of 20 network structures could be reproduced.

Connections between neurons were defined by a synaptic conductance pulse:

$$g_{syn,ij}(t) = \max\left(\left(e^{\frac{-(\tilde{t}_{max}-\tau_D)}{\tau_S}} - e^{\frac{-(\tilde{t}_{max}-\tau_D)}{\tau_F}} \right)^{-1} \left(e^{\frac{-(\tilde{t}_j-\tau_D)}{\tau_S}} - e^{\frac{-(\tilde{t}_j-\tau_D)}{\tau_F}} \right), 0\right) \quad \text{(II.1)}$$

$$\tilde{t}_{max} = \frac{\tau_D\tau_S - \tau_D\tau_F - \tau_S\tau_F ln\left(\frac{\tau_F}{\tau_S}\right)}{\tau_S - \tau_F} \quad \text{(II.2)}$$

where $\tilde{t}_j$ is the time of the last spike fired by the presynaptic neuron *j*, $\tilde{t}_{max}$ is the time where the synaptic pulse reaches its maximum, τ_D is a synaptic delay constant set to 0.08 ms, τ_S is the slow synaptic decay constant set to 3 ms, and τ_F is the fast synaptic decay constant set to 0.3 ms. Thus, the synaptic pulse ranges between 0 and 1. The total synaptic input to a neuron i is defined by:

$$I_{syn,i}(t) = w_e \sum_{j=1}^{N_E} A_{ij} g_{syn,ij}(t)(E_E - V_i) + w_i \sum_{j=1}^{N_I} A_{ij} g_{syn,ij}(t)(E_I - V_i) \quad \text{(II.3)}$$

where V_i is the membrane potential of neuron *I*, $E_{E/I}$ is the reversal potential of either excitatory or inhibitory synapses, A_{ij} is 1 if neuron *j* synapses onto neuron *i* or 0 otherwise, and $N_{E/I}$ is the number of excitatory or inhibitory neurons. The synaptic weight, $w_{e/i}$, was set to 0.2 mS/cm^2 for all simulations, unless otherwise stated.

In the Ks neuron model (see also chapter I), the membrane potential evolved according to:

$$c_m \frac{dV_i}{dt} = I_{syn,i} + I_{ext,i} - m_\infty^3 h \bar{g}_{Na}(V_i - E_{Na}) - n^4\, \bar{g}_{Kdir}(V_i - E_K)$$

$$-s\bar{g}_{Ks}(V_i - E_K) - g_L(V_i - E_L), \quad \text{(II.4)}$$

where $\bar{g}_x$ is the maximal conductance associated with an ionic current, E_x is the reversal potential for an ion, and $I_{ext,i}$ is a random direct current which is unique to each neuron and constant during a simulation. The range of $I_{ext,i}$ was set to 2.0 μA/cm2 and the mean was set so that all neurons would fire at 10 Hz without any synaptic input. The gating variables *h*,*n*, and *s* were of the form

$$\frac{dx}{dt} = \frac{(x_\infty(V) - x)}{\tau_x(V)}, \tag{II.5}$$

where $x_\infty(V)$ is the steady state value of the variable and $\tau_x(V)$ is the time constant. $\tau_s(V)$= 75 ms for all *V*. When V_i crossed 0 mV a spike was recorded and synaptic outputs were triggered. $\bar{g}_{Ks}$ is the parameter responsible for the transitions in excitability seen in this model and is used as a proxy for the level of acetylcholine (which is inversely proportional $\bar{g}_{Ks}$). Noise was introduced by randomly inducing spiking in all neurons at a low rate. Unless otherwise noted the frequency of noise was set to 1 Hz .All simulations were integrated for 7 s at a 0.05 ms time step using a 4th order Runge-Kutta algorithm. This neuronal dynamic was taken from [82], for more details see [85].

2.2.2 Correlation and Network Similarity

The dependence of network firing pattern on network structure, or the pattern of DC inputs, was quantified by a network similarity score based on either frequency or phase, NS_{Freq} or NS_{Phase}. This score was defined by:

$$NS_{Freq,i} = \frac{<S_{Freq,i}> - <S_{Freq,\sim i}>}{2}, \tag{II.6}$$

$$\text{or: } NS_{Phase,i} = \frac{<S_{Phase,i}> - <S_{Phase,\sim i}>}{2} \tag{II.7}$$

where $S_{x,i}$ (x = *Freq* or *Phase*) is the similarity between all runs on the same realization of network structure i (or of DC input pattern i); $S_{x,\sim i}$ is the similarity between the runs on network i and all other network realizations (or with DC input pattern i and all other DC input patterns). NS_x will be 1 if all runs on the same network (or input pattern) realization have identical network similarity while all other network (or input pattern) realizations are orthogonal, and it will be 0 if all runs are equally similar regardless of network structure (or DC input pattern). NS_x will be −1 if all runs on the same network (or DC input pattern) realization have orthogonal network similarity but it is identical on runs with different realizations.

Spiking dynamics from 20 patterns of external current input or 20 network structures were analyzed. Each pattern or network was simulated 50 times. The network activity was quantified in two ways. The first was to calculate an average firing rate for neurons in a network. To maximize the variance in the data principal component analysis was performed on the frequencies for all simulations run at a given $\bar{g}_{Ks}$ and the frequencies were projected onto the 1st principal component for further analysis. The correlation of firing rates (in PCA space) between simulations was calculated as the dot product of a vector containing frequencies sorted by cell id for each simulation, yielding the value SF. All analysis considered only spikes which fired during the last 5 s of the simulation. Phase correlations were calculated in a similar manner. As a control, the frequencies/phases were scrambled and assigned to random neurons.

Whether a network was in a phase coding regime was based on a measure of how stable the phase relationships are between neurons in the network. For a pair of neurons *i* and *j* the phase relationship for a given (the k^{th}) spike fired by neuron *i* is $\phi_{ij}^{k} = 2\pi \frac{(t_k^i - t_-^j)}{(t_+^j - t_-^j)}$, where t_k^i is the time of the k^{th} spike fired by cell *i*, t_-^j is the time of the last spike fired by neuron *j* before t_k^i, and t_+^j is the time of the first spike fired by neuron *j* after t_k^i. Between neurons *i* and j the phase coherence, or how reliable the phase difference between the neurons is across cycles, is:

$$r_{ij} = \frac{1}{T}\sum_{k=0}^{T} e^{i\phi_{ij}^{k}}, \tag{II.8}$$

where *T* is the number of spikes fired by neuron *i* that are between a pair of spikes fired by neuron *j*. Note that this measure is not reciprocal (i.e. $r_{ij} = r_{ji}$ is not always true). The pairwise r_{ij} values are averaged for all neurons which fire more than 30 spikes in the simulation and for presentation the average value of each network was computed. Network bursts were identified by binning spike times into 0.05 ms time bins and convolving with a gaussian kernel $k(t) = e^{\frac{-t^2}{\sigma^2}}$ evaluated between -10 and 10 ms and with σ^2 of 1 ms.

When the convoluted signal was above a threshold of 10% of the neurons in the network the network was considered to be in a burst. Each burst was padded with 10 ms before and after the threshold crossing to any capture the spikes initiating the burst. To evaluate the similarity of two bursts the order of neuron's firing in a burst window was correlated. Example bursts were selected by identifying those bursts with the highest correlation on

two different runs on the same network realization. Average pairwise burst correlations were compared between two runs on the same network realization and one run on two different realizations.

2.3 Results

In a network, the I_m mediated switch between Type 1 to Type 2 excitability together with effects of SFA have a profound influence on resulting network dynamics. Using numerical modeling we've investigated how transitioning neurons from Type 1 to Type 2 excitability impact the patterns of neural activity in networks. We use the conductance-based Ks neuron model of cholinergic modulation [158]. The details of this model are included in Chapter I and Section 2.2 of this chapter. This biophysical model reproduces the effects of ACh blocking I_m through activation of the M1 acetylcholine receptor. Throughout this thesis it will be referred to as the Ks model, named for the slow potassium conductance, $\bar{g}_{Ks}$, responsible for the transition from Type 1 to Type 2. Specifically, low $\bar{g}_{Ks}$ corresponds to the high ACh, Type 1 excitability condition.

As we dicussed in Ch 1, when ACh is high, neurons in the network are Type 1, and the f/I curve increases continuously from 0 Hz with a steep slope as a function of input currents between neurons (Figure I.3A). This will result in a wide distribution of firing frequencies across the network when cells are driven by heterogeneous synaptic input or external drive. The resulting frequency distribution will be stable through time, due to reduced SFA during high ACh conditions (low $\bar{g}_{Ks}$, Figures I.3B,C). On the other hand,

during low ACh conditions (high $\bar{g}_{Ks}$), when Type 2 excitability dominates, variations in input across the network create less variance in neuronal firing rates due to the shallow slope of the f/I curve. As the firing rates are more uniform, oscillatory firing paired with the increased synchronizability demonstrated by the shape of the PRC (Figures I.3D,E) leads to synchronized bursting. The variations in inputs are now reflected by relative phases of firings among interacting neurons, rather than by their frequency variations. Through the changes in neural excitability controlled by the M-current, the circuit is thus shifted between these two, distinct functional regimes: rate coding when ACh is high (low $\bar{g}_{Ks}$, Type 1) and phase coding when ACh is low (high $\bar{g}_{Ks}$, Type 2; these changes are summarized in Figure I.3F).

Much of the previous work on the different dynamics displayed by Type 1 vs. Type 2 networks indicates that Type 1 networks are more sensitive to variations in network structure [84]. Specifically, Type 1 networks have higher variability in neuronal frequency and our results suggest that the particular frequency distribution of these networks will be highly dependent on a particular physical network realization [87]. Type 2 networks, on the other hand, have more uniform firing rate distributions leading to more synchronous dynamics, suggesting that the effect of the specific network structure will be seen in the phase relationships between neurons. To provide an initial test of this prediction we generated a set of unique networks based on the Watts-Strogatz network model [159]. The networks were composed of two interconnected ring lattices, one excitatory and one inhibitory. Since the Watts-Strogatz model of network generation is based on random processes, specific network structures (i.e., sets of inputs and outputs for each neuron)

can be reproduced by changing the seed in a random number generator. We generated 20 network realizations; each network structure was simulated 50 times for a given $\bar{g}_{Ks}$, randomizing voltage and gating variable initial values each time. This allowed us to compare firing patterns between the 50 runs on the same network realization with the 950 runs on the other network realizations. Additionally, to examine the effects of changing patterns of inputs, a parallel line of simulations were run on an unchanging network structure but with randomized patterns of external applied current (DC) inputs applied across the cells in the network. We generated 20 DC patterns and simulated each 50 times for a given $\bar{g}_{Ks}$ value and random initial conditions.

2.3.1 Network Representation of Phase and Frequency Code

We first investigated how the firing patterns changed when network connectivity structure is varied. In the absence of variations in external input between neurons, patterns in network activity should reflect the specific structure of the network. The aim of these simulations is to show that, for each network topology, for high ACh (low $\bar{g}_{Ks}$) a neuron's firing rate will be more correlated on the 50 runs with the same network realization than on the 950 runs with the other network realizations, but that this effect will be reduced as ACh falls. In terms of relative phases of firing between neurons, the opposite will occur. Namely, when ACh is low (high $\bar{g}_{Ks}$), the pairwise phase relationships between neurons will be more correlated on the same network realization compared to the other realizations and that this specificity is reduced as ACh increases.

This effect is apparent when examining raster plots of network activity. Spiking dynamics for low $\bar{g}_{Ks}$ lack temporal organization (Figure II.1A) and neurons have variable firing rates

(revealed by density of points on the raster plot). The raster plots show that the firing rate pattern is dependent on the network structure for low $\bar{g}_{Ks}$, with cells exhibiting different rates in different networks. For high $\bar{g}_{Ks}$ firing rates are more uniform as networks enter a bursting regime. Here the frequencies of cells across the network are highly similar, but the organization of neurons within bursts is more consistent across runs on the same network realization and changes for different network realizations. This result is summarized on Figure II.1B; for low $\bar{g}_{Ks}$ networks the frequency correlation of neurons is high on the same network structure and very low across structures (Figure II.1B, left). When comparing burst structure in high $\bar{g}_{Ks}$ networks, quantified by neuron order within a burst, compared runs on the same network realization have more similar burst structure than those on different realizations (Figure II.1B, right).

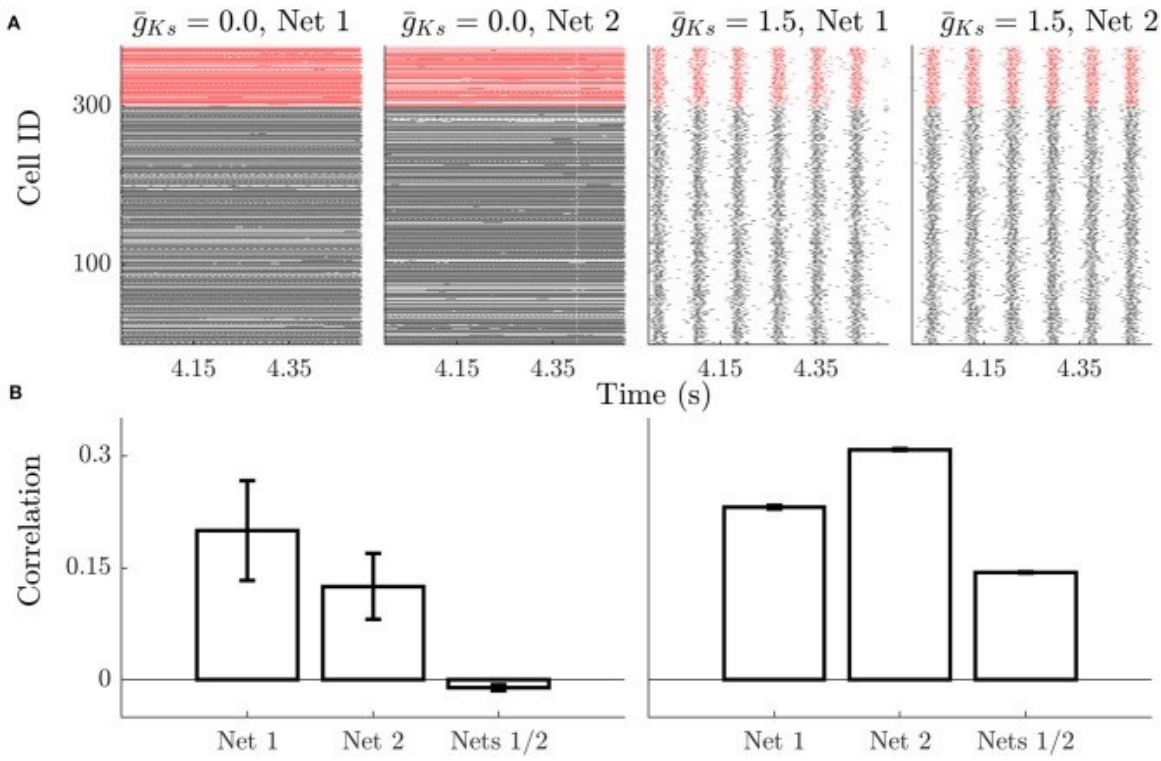

Figure II.1 Example dynamics show rate specificity during high ACh dynamics and high phase specificity during low ACh dynamics.

(A) Raster plots show that high ACh networks have high similarity in firing rates, but low temporal organization. Changes in network structure (Net 1 vs. Net 2) alter which neurons are high frequency vs. low frequency, but this is stable between simulations on the same network. Low ACh networks have a more uniform firing rate but more temporal organization and synchrony. The phase relationships between neurons is stable across stimulations, but not across networks. Black rasters indicate the spike time of excitatory neurons and red rasters indicate inhibitory spikes. **(B)** During High ACh conditions the firing rate of neurons is highly correlated during simulations run on the same networks and uncorrelated between runs on different networks (left). The order of neuron firing during bursts is higher between runs on the same network compared with runs on different networks during low ACh conditions (right). Error bars indicate s.e.m.

2.3.2 Mechanism of Coding Switch

We next proceeded to quantify more carefully the underlying mechanisms of this coding switch. We first investigated the modulation of frequency variance and phase locking (as measured by mean phase coherence, MPC) with varying ACh as it provides a basis for the different coding schemes (Figure II.2). We observed that high ACh networks have high frequency variance and low phase locking. As ACh is reduced ($\bar{g}_{Ks}$ is increased), frequencies become more uniform, and phase locking increases. Figure II.2 (top, black curve) shows that when ACh is high ($\bar{g}_{Ks}$ is low) the firing rate distribution is wide as measured by coefficient of variation. As ACh is reduced firing rate variance rapidly decreases and all neuron firing rates collapse to the mean, which can be seen by comparing empirical cumulative distribution functions of firing rate on the same network for varying $\bar{g}_{Ks}$(Figure II.2, bottom). At the same time, the transition to phase locked firing happens for networks with low ACh (high $\bar{g}_{Ks}$) (Figure II.2, top, red curve). This transition supports a transition between rate and phase coding regimes. These two effects on the character of network dynamics provide a substrate for each coding scheme at each pole of cholinergic modulation. High ACh networks are primed for rate coding and low ACh networks are primed for phase coding.

We then investigated the effects of differential input on the network dynamics. Specifically, we measured the effect on network dynamics, in both regimes (high and low ACh), when randomly chosen neurons receive additional input current. We compared dynamics of networks with constant structure, where 20 excitatory neurons received an

additional offset current I_{offset} (up to 1.95 μA/cm2) above the remaining neurons. In these simulations, when $\bar{g}_{Ks}$ = 0.0 mS/cm2 , increasing I_{offset} reliably increased the firing rate of the subset of neurons as expected (Figure II.3A). When $\bar{g}_{Ks}$ = 1.5 mS/cm2 , the subset of neurons fired at an increasingly earlier phase as I_{offset} increased (Figures II.3B,C). The increase in firing during high ACh conditions and the phase advancement in the low ACh conditions are correlated (Figure II.4D) providing a link between the two representations. The effect of differential input on frequency and phase form the basis for frequency coding when ACh is high and phase coding when ACh is low.

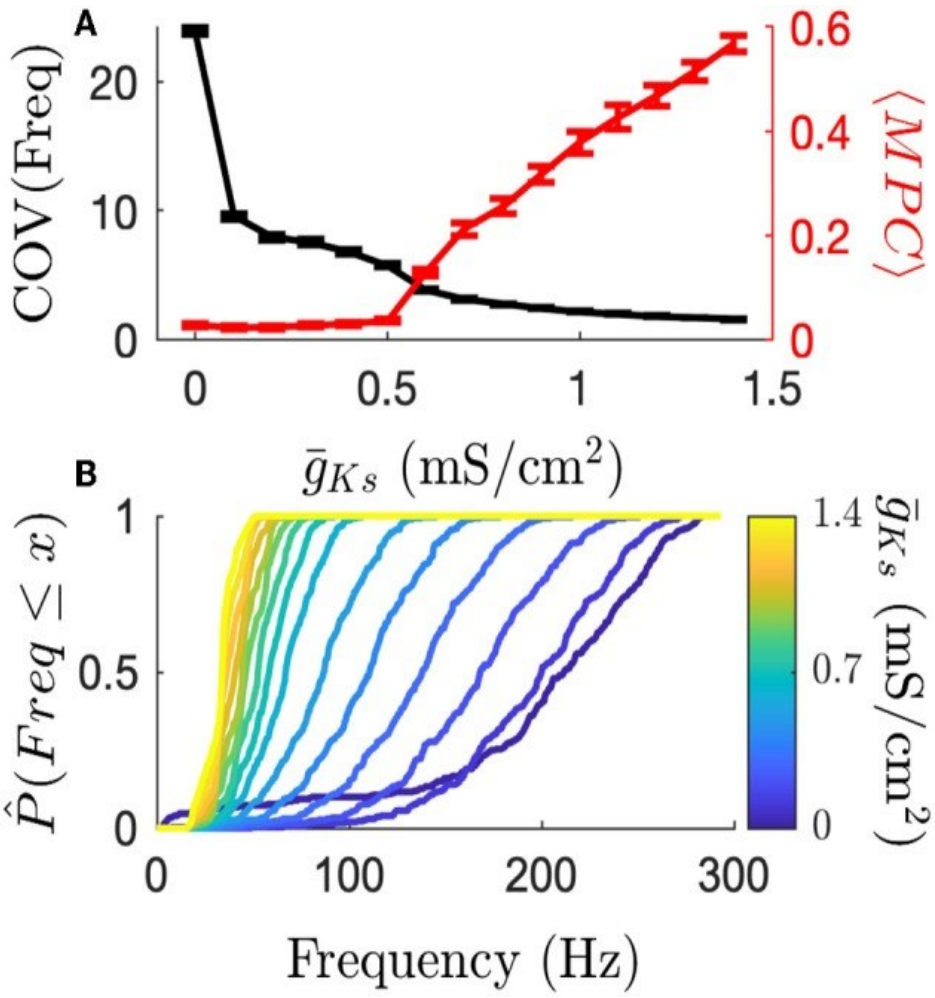

Figure II.2 The transition from high frequency variance to high phase locking shows how cholinergic modulation can change coding principles.

(A) High ACh networks have highly varied firing rates as measured by the coefficient of variation. Firing rates quickly become more uniform as gKs increases. Conversely, MPC (phase locking) is high for low ACh networks. **(B)** Frequency CDFs for single simulations, each on the same network structure, show that the same network display large differences in the variance of firing rates across the network. High ACh networks have high variance, which deceases dramatically as ACh is reduced. Error bars indicate s.e.m.

To further pursue our hypothesis and measure the extent that networks either rate code or phase code information about their structure, we investigated if the correlation in frequency (for Type 1, high ACh, low $\bar{g}_{Ks}$ conditions) or the phase locking (for Type 2, low ACh, high $\bar{g}_{Ks}$conditions) between pairs of neurons would be more similar on repeated simulations of the same structural realization of randomly generated networks vs. different structural realizations. Similarly, for the dynamical response to external stimulation patterns in networks with fixed connectivity, we investigated if the correlation in frequency (under Type 1, high ACh, low $\bar{g}_{Ks}$ conditions) or the phase locking (for Type 2, low ACh, high $\bar{g}_{Ks}$ conditions) between pairs of neurons would be more similar on repeated simulations with the same DC input pattern to the network vs. different random realizations of DC input.

To measure these functional relationships between neurons, we constructed a similarity score based on three measures: pairwise mean phase, pairwise MPC, and frequency. As indicated before, MPC is a measure of phase locking between pairs of neurons and ranges between 0 for random firing and 1 for perfect phase locking. To compare two simulations, we define the phase similarity (S_{Phase}) as the correlation in pairwise mean phase calculated across all neurons that fired 30 or more spikes in both simulations. Similarly, to compare neuron frequencies across simulations, the frequency similarity (S_{Freq}) is defined as the correlation of their frequencies across both simulations. To maximize the variance within the data, principal component analysis was performed on

the data for each level of $\bar{g}_{Ks}$, and the data was projected onto the 1st principal component for only correlation analysis. Calculation of MPC and coefficient of variation were performed on raw data.

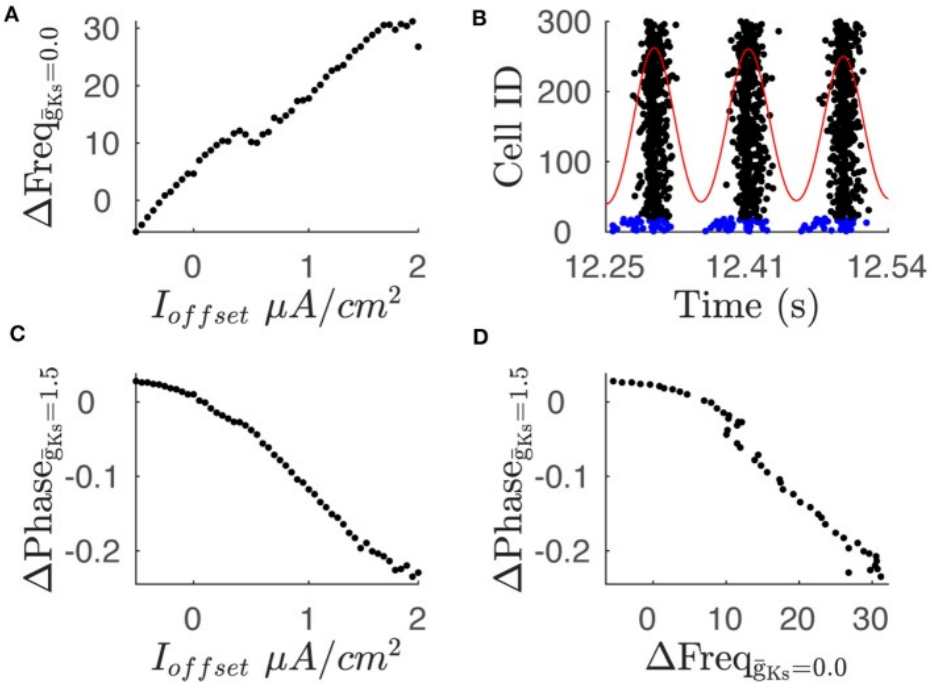

Figure II.3 Variations in current input between neuron subsets leads to changes in average frequency and phase.

(A) The difference in average frequency of the two neuron populations shows a positive relationship with the difference in current input, labeled as Ioffset, when gKs is 0.0. **(B)** Raster plot shows phase leading in spike times of neuron subset. The raster plot shows spike times for neuron population where 20 neurons receive an additional current input of 1.95 μA/cm2. Blue rasters indicate subpopulation with additional current while black rasters indicate sub population with baseline current input. Red trace shows convolution of spike times with Gaussian function which is used to define the phase reference. The above simulation is conducted with a gKs value of 1.5. **(C)** Phase difference between subpopulation with additional current input and subpopulation with baseline current input shows a negative relationship with the current input. **(D)** Comparison of the phase difference and frequency difference for a given current input. Plot shows comparison of phase difference for gKs = 1.5 and frequency difference for $\bar{g}_{Ks}$ = 0.0 for a given current offset.

2.3.3 Input Representation for Frequency and Phase Code

To account for the effect of an increased bandwidth which results from a wider distribution of frequencies (i.e., a frequency pattern with a wider range will be easier to detect than a narrow pattern) NS_{Freq} was scaled by the coefficient of variation as such: $NS_{Freq,i} =< Cov_{Freq,i} > \frac{<S_{Freq,i}>-<S_{Freq,\sim i}>}{2}$. Similarly, to account for low MPC reflecting random firing between neurons NS_{Phase} was scaled by the average MPC of each network across all simulations: $NS_{Phase,i} = \frac{<S_{Phase,i}>-<S_{Phase,\sim i}>}{2}$ For simplicity, pairwise phase relationships between all excitatory neurons and an arbitrary inhibitory neuron were analyzed.

We measured mean frequency similarity score, NS_{Freq}, for both cases, networks with changing DC input patterns (Figures II.4A–C) and changing connectivity structure (Figures II.4D–F), and we measured phase similarity score NS_{Phase}, for the two cases (Figures II.5A–C and Figures II.5D–F, respectively). The results in both figures are compared to scrambled spike trains (blue line).

Rate coding of DC input pattern (Figures II. 4A–C) and network structure (Figures II.4D–F) was prevalent for high ACh (low $\bar{g}_{Ks}$) dynamics and reduced for low ACh (high $\bar{g}_{Ks}$) dynamics. As $\bar{g}_{Ks}$ increased (lower ACh), network frequency similarity scores decreased (first and middle columns), but not because of reduced frequency correlations within the same input pattern (last column).

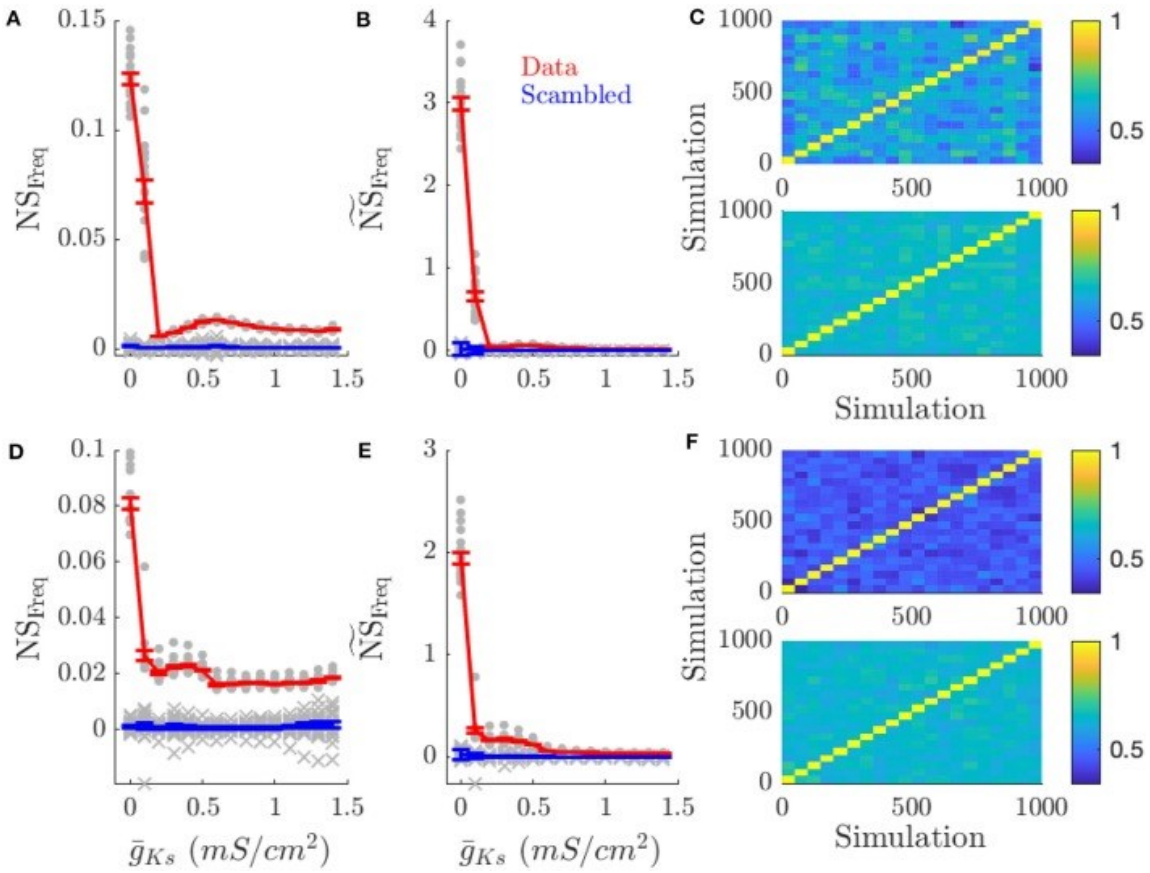

Figure II.4 High ACh networks show increased rate coding which is diminished in low ACh networks.

Rate coding, measured by the specificity of neuronal firing rates across simulations with the same pattern of inputs across the network vs. different patterns of input, occurs for high ACh networks. This effect is decreased in low ACh networks, largely because firing rates become more similar between different networks. **(A)** NSFreq is the network score based on comparing frequency correlations on simulations with the same input pattern against simulations with different patterns. **(B)** NSFreq scales NSFreq by the coefficient of variation for frequency. **(C)** Color plots show the correlation of firing rates between simulations for gKs=0.0 and gKs=1.4 mS/cm2 (top and bottom, respectively). Each simulation is sorted along the x and y axis by network structure. A similar effect occurs when information is represented through network structure. **(D–F)** NSFreq, NSFreq, and correlation plots for simulations with varying network structure. Gray points show the NSFreq for each input pattern or network structure. Gray crosses show NSFreq for scrambled data. Error bars indicate s.e.m.

Instead neuronal frequencies across other network realizations became more correlated. This is evident in the frequency correlations for runs on the same realization of an input pattern or network structure compared to runs with other patterns or structures (diagonal vs. off-diagonal elements in Figures II.4C,F, respectively). This is expected as all frequencies across all network realizations converge due to reduced gain of the f/I curve for Type 2 cells.

In low ACh (high $\bar{g}_{Ks}$) conditions, networks have highly phase locked dynamics and phase coding prevails (Figure II.5). Networks presented with the same pattern of inputs (Figures II.5A–C) or having the same network structure (Figures II.5D–F) showed higher network phase similarity scores as $\bar{g}_{Ks}$ increased (first and middle columns), and displayed higher phase correlations than between different patterns or structures when $\bar{g}_{Ks}$ is high (low ACh) (color plots in Figures II.5C,F). As ACh is reduced (and $\bar{g}_{Ks}$ is correspondingly increased) correlations in firing phase decrease. This effect is apparent in NS_{Phase} (Figures II.5A,D) and becomes even more pronounced when phase-locking is taken into account (Figures II.5B,E). As opposed to frequency correlations, phase correlations are uniformly low for simulations where different patterns were presented (Figure II.5C). This effect is due to the low phase locking in high ACh conditions.

Finally, we checked robustness of the obtained results by introducing and varying the level of external noise to the networks and also, separately, by changing the strength of excitatory coupling, which effectively changes internal excitatory inhibitory balance within

the network. Rate coding during high ACh conditions and phase coding for low ACh was robust to changes in noise and variations in excitatory coupling.

.

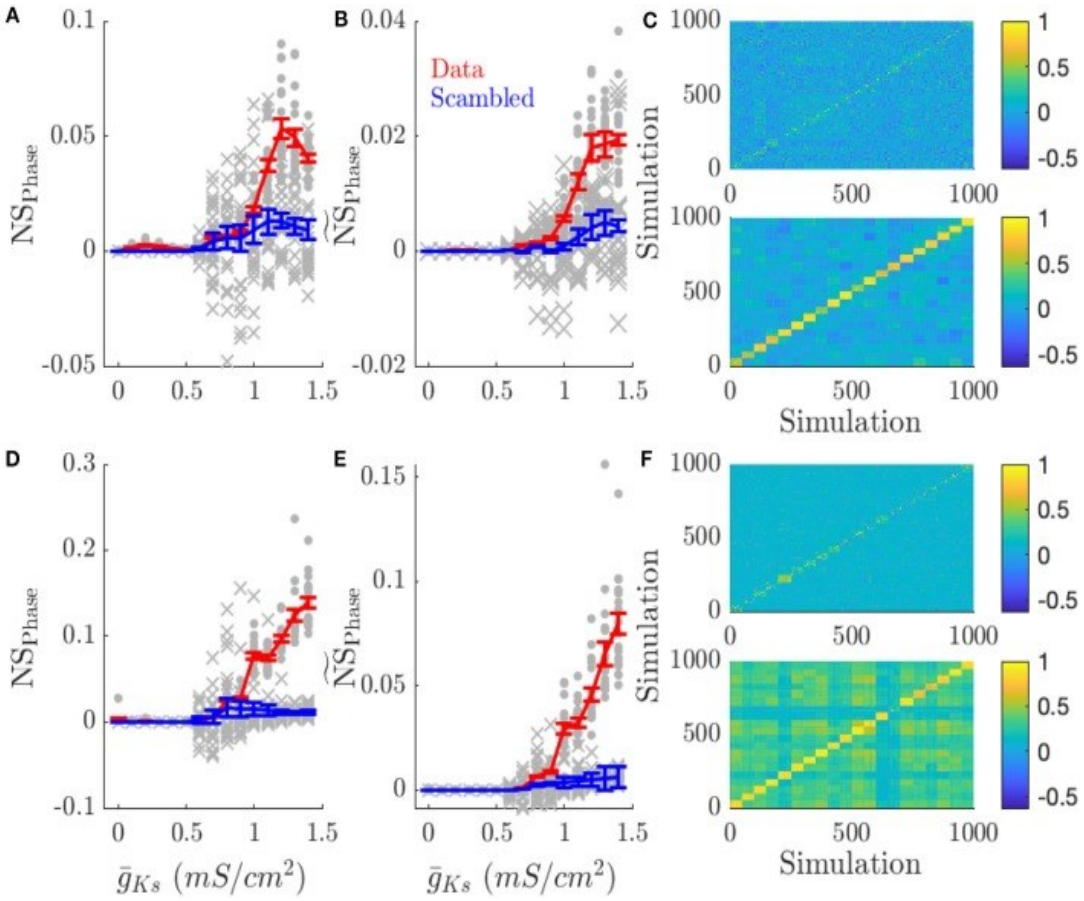

Figure II.5 Low ACh networks show increased phase coding.

Phase coding, measured by the network specificity of mean phase coherence across simulations with the same input pattern vs. different patterns, occurs for low ACh networks on all topologies. This effect is decreased in high ACh networks, due to the increased frequency variation and decreased phase locking. **(A)** NSPhase is the network score based on phase correlations. **(B)** NS Phase scales Phase by the mean MPC of the simulations. Scaling average MPC accounts for low MPC reflecting essentially random firing. **(C)** Color plots show the correlation of phase values between simulations for $\bar{g}_{Ks}$ =0.0 and $\bar{g}_{Ks}$ =1.4 mS/cm2 (top and bottom, respectively). Each simulation is sorted along the x and y axis by network structure. **(D–F)** NSPhase, NSPhase, correlation plots for simulations with varying network structure. Gray points show the NSPhase for each input pattern or network structure. Gray crosses show NSPhase for scrambled data. Error bars indicate s.e.m.

Supplemental Figures II.S1, S2 in the Appendix at the end of this thesis show the effect of increasing noise on frequency coding (Figure II.S1) and phase coding (Figure II.S2). When information is presented as the pattern of DC input, in high ACh networks frequency coding is robust to increasing noise and was uniformly low for low ACh networks. Phase coding of inputs is more sensitive to noise at high $\bar{g}_{Ks}$, and uniformly low for low $\bar{g}_{Ks}$ (Figure II.S2 in the Appendix at the end of this thesis). As excitatory coupling was scanned from zero to 0.04 mS/cm2 , frequency coding of inputs initially decreased as coupling was increased for all $\bar{g}_{Ks}$, but for low $\bar{g}_{Ks}$ networks frequency coding recovered (Figure II.S3 in the Appendix at the end of this thesis). Low $\bar{g}_{Ks}$ networks maintained a higher NS_{Freq} as coupling increased compared to high $\bar{g}_{Ks}$ networks. When representing network structure, coupling needed to reach a sufficient level for frequency coding to occur. Phase coding, on the other hand, required a minimum coupling strength to emerge (Figure II.S4 in the Appendix at the end of this thesis), but only emerged for high $\bar{g}_{Ks}$.

2.4 Discussion

Using the Ks model we have shown that neuromodulation of the M-current can switch networks from a rate coding regime when ACh is high ($\bar{g}_{Ks}$ is low) to an oscillatory phase coding state when ACh is low ($\bar{g}_{Ks}$ is high). This neuronal model recreates biophysical changes displayed in neurons when the muscarinic system is activated, including gain modulation, PRC modulation, and SFA modulation (Figure I.3). As ACh levels are

continuously changed, these three properties are inflected over different ranges of the maximal conductance of the I_M, $\bar{g}_{Ks}$.

We note that here we focus only on the biophysical effects of a single target of ACh modulation, inactivation of slow (M-type) potassium channels. However, ACh has numerous effects both at the cellular and network level. Through the nicotinic receptors ACh directly depolarizes neurons and the nicotinic signal is faster than the cascade required to inactivate M-type potassium channels. Activation of muscarinic receptors also inhibits presynaptic release at both excitatory and inhibitory axon terminals reducing the effects of recurrent connectivity [92,160]. During high ACh release direct depolarization of neurons through nicotinic receptors, reduction in local network inputs, increased gain, and reduced SFA could all work together to prime a network to represent an external input in the firing rate distribution. Removal of these effects would lead to phasic dynamics shaped by the structure of the local network.

It is important to note that all three of I_M modulated properties, gain modulation, PRC modulation, and SFA modulation, are important for switching from a rate to a phase coding regime. For rate coding in high ACh conditions, high gain is beneficial in widening the firing rate distribution for a given range of synaptic inputs. Low SFA allows neurons to persist in firing to maintain a representation in frequency space and low synchrony facilitated by Type 1 PRC, prevents a reduction in frequency variation. For phase coding under low ACh conditions, low gain reduces frequency variation in the network, while a

Type 2 PRC and high SFA induce increased periodicity and synchronizability for phase differences to persist.

Thus, reductions in ACh level provide two dynamical substrates for phase coding: (1) near uniformity in firing rates across the network, and (2) the ability of neurons to collectively organize into network-wide oscillatory behavior. By directly quantifying the dependence of a network firing pattern on a particular network realization for networks of the same connection structure and external input pattern we've provided strong evidence that Type 1 networks represent information about internal structure and external inputs through rate coding (Figure II.4) while Type 2 networks' firing patterns provide oscillatory phase coding dynamics (Figure II.5).

The fact that the transition from rate coding to phase coding firing patterns occurs over the $\bar{g}_{Ks}$ range when the gain of the neuron (f/I curve) is significantly modulated, points to the importance of this property for switching coding regimes. When a network of high gain neurons is formed, slight variations in synaptic input will result in higher firing rate differences between neurons. This wide, input dependent, firing rate distribution will drive the network firing rate distribution and be reproducible for a given set of inputs or a given network structure. As gain is reduced, frequency differences between neurons will be reduced allowing neuronal properties such as SFA and PRC effects to impact network dynamics in a significant way. For example, it is well-known that networks of periodic oscillators synchronize easier when the frequency range is reduced and that large

variance in frequencies promotes the formation of discrete clusters of synchronization [161–163]

Spike initiation dynamics and the adaptation mechanics of neurons have been suggested as being substrates for coding through integration or coincidence detection[75,164]. While both integrative and coincidence coding can exist with wide firing rate distributions, phase coding relies on neurons being close in frequency while high neuronal gain facilitates rate coding [165]. The importance of co-modulation of neuronal gain and excitability type in transitioning a network from rate to phase coding is an essential result of the present work.

Gain modulation improves signal recognition in a variety of brain regions[166–168]. In many cases gain modulation is attributed to fluctuations in synaptic inputs and synaptic plasticity due to gain modulation being stimulus dependent [169–171]. But changes in ACh tone also change the gain response of neurons [72,172,173]. ACh release is increased when an animal is performing an attentional task and its release is correlated with task performance[174–176].These results point to cholinergic modulation priming neuronal networks to respond with an appropriate rate code to a given cue by increasing the gain of the neurons. This also indicates that rate coding may be better at facilitating representations of sensory information than phase coding.

The Type 2 dynamics of the low ACh state support robust synchronized bursting required for oscillations in population activity[84,85,88]. ACh release is important for the generation

of the theta rhythm in the hippocampus[92,177,178]. But a temporal analysis of both ACh release and theta band power shows that peaks in ACh release lag behind increases in theta power [116]. This suggests that ACh release is actually working to disrupt synchrony within the theta oscillation. Further evidence for the role ACh release could play in reducing synchronous firing is seen in its suppression of sharp wave ripples [92].

Changes in coding modality, in addition to affecting information transfer to downstream targets, would have a profound effect on learning through activity dependent synaptic plasticity. STDP has a strong frequency dependence, even with random spike trains[179]. When spike pairs are presented at a high frequency synapses have net potentiation, but have net depression for low frequency. When networks are in the high ACh rate coding regime, this would lead to highly activated neurons forming a strongly connected cluster within the networks, which would reinforce the specific frequency pattern imposed by an external stimulus. During the low ACh phase coding regime the stable phase relationships would shape synaptic plasticity. The reduction in mean frequency would lead to a net reduction in synaptic weight and the synchronization and resonance properties of neurons in the low ACh state preferentially strengthen connections from neurons with high input to neurons with low input [128,156]. A complicating factor in interpreting the effects of ACh on network coding is that ACh significantly modulates STDP itself, acting as a gate on the LTD component, thus reducing the plasticity effects during low ACh conditions[180].

ACh release is very closely related to the sleep-wake cycle. ACh release is highest during wakefulness and rapid eye movement (REM) sleep and lower during non-REM (NREM) sleep [181]. When the Ks model simulates these levels of ACh it recreates similar changes in spiking dynamics that are seen across these states [87]. Within the context of the effects of ACh on network dynamics, we hypothesize that the high ACh waking state highlights the variance in magnitudes of external inputs to the given circuit in terms of neuronal frequency responses and primes networks to encode these inputs as stable patterns in frequency space subsequently storing this representation within synaptic weights. Elevated firing frequency and representations in frequency space may be important for the rapid encoding of the memory backbone and for transfer of information to other brain regions. In NREM sleep, when no external input is present and firing frequency distributions across neurons homogenize [182], oscillatory dynamics pairs with phase coding to represent stored information as spike time differences between neurons which could facilitate consolidation of stored memories from a small group of neurons with strong synaptic inputs to the network as a whole [114]. Additionally, ACh effects on synaptic plasticity, namely high ACh leads to increases in average synaptic weights and low ACh decreases them, support the synaptic homeostasis hypothesis [156,183], but at the same time the proposed shift in the coding schemes paints a more complex picture of specific roles of sleep cycles. The widening of neuronal firing rate distributions across sleep-wake states also indicates that gain modulation by ACh is shaping network activity [184,185].

The role of ACh level in sleep dependent memory consolidation and synaptic homeostasis suggests that changes in coding modality may be optimized for storage of information in various encoding/behavioral states. Namely, during waking, high ACh conditions lead to enhancing the connections between neurons which receive the most input, forming a tightly connected cluster which forms the kernel of a new memory. In the sleep that follows, cycles of phase coding NREM distributing this kernel throughout the network are paired with cycles of REM reinforcing the distributed memory by re-enhancing connections to the neurons most active during REM bouts.

Thus, ACh modulating the coding regime across behavioral states may facilitate an iterative process by the sleep cycle to tune memory consolidation[114]. Thus, we propose that ACh is a neuromodulator that is critical for memory consolidation throughout the brain. The biophysical changes in neural excitability that I_M governs lead to significant changes in the spiking and oscillatory processes in the brain. The effects of gain modulation in switching between circuit activity that has high or low dependence on network structure or external input pattern may be central to ACh's role in information processing at the network level. Additionally, the dynamic nature of ACh release could allow for a stable network to coordinate information processing functions across various brain states. While ACh has other pathways of neuromodulation, notably through the nicotinic receptor which directly depolarizes neurons [186] we show that the muscarinic effects of changing ACh levels are sufficient to change coding modes.

Chapter III

Acetylcholine-Gated Current Translates Wake Neuronal Firing Rate Information Into a Spike Timing-Based Code in Non-REM Sleep, Stabilizing Neural Network Dynamics During Memory Consolidation

3.1 Introduction

Sleep is critical for memory consolidation, however the exact mechanisms mediating this process are unknown. Combining reduced network models and analysis of in vivo recordings, we tested the hypothesis that neuro-modulatory changes in acetylcholine (ACh) levels during non-rapid eye movement (NREM) sleep mediate stabilization of network-wide temporal firing patterns, with order of neuronal firing dependent on their intrinsic mean firing rate during wake. To that extent we find, in both reduced models and in vivo recordings from mouse hippocampus, that the order of firing among neurons during NREM sleep reflects their relative firing rates during prior wake. Our modeling results show that this remapping of wake-associated, firing frequency-based representations is based on NREM-associated changes in neuronal excitability mediated by an ACh-gated potassium current. We also show that learning-dependent reordering of sequential firing in the hippocampus during NREM sleep, together with spike timing-

dependent plasticity (STDP), reconfigures neuronal firing rates across the network. This rescaling of firing rates has been reported in multiple brain circuits across periods of sleep. Our model results and experimental data both suggest that this effect is amplified in neural circuits following learning. Together our data suggest that sleep may bias neural networks from firing rate-based towards phase-based information encoding to consolidate memories.

I was a primary author on this work which was published and peer reviewed. Experimental data/analysis was obtained through a collaboration with the Aton Lab as described in Section 3.2, my primary contribution was developing the model including parameter selection as well as analysis of the model results. The article describing these results was published in PLOS Computational Biology[187].

3.2 Methods

3.2.1 Experimental Methods

Hippocampal Recordings, Fear Conditioning, and Sleep Deprivation

All procedures were approved by the University of Michigan Animal Care and Use Committee (animal protocol #: 00008333). Male C57BL/6J mice between 2 and 6 months were implanted using methods described previously [115,188]**.** Recording implants (described in more detail in[115] consisted of custom built driveable headstages with two bundles of stereotrodes implanted in bilateral CA1 and three EMG electrodes to monitor nuchal muscle activity. The signals from the stereotrodes were split into local field potential (0.5-200 Hz) and spike data (200 Hz-8 kHz).

Following post-operative recovery, mice either underwent CFC (placement into a novel environmental context, followed 2.5 min later by a 2-s, 0.75 mA foot shock; n = 5 mice), Sham conditioning (placement in a novel context without foot shock; Sham; n = 3 mice), or CFC followed by 6 h of sleep deprivation by gentle handling (a manipulation known to disrupt fear memory consolidation[115,131,189,190] **;** SD; n = 5 mice). Spike data from individual neurons was discriminated offline using standard methods (consistent waveform shape and amplitude on the two stereotrode wires, relative cluster position of spike waveforms in principle component space, ISI ≥ 1 ms) [115,124,131,191,192]**.** Only neurons that were stably recorded and reliably discriminated throughout the entire baseline and post-conditioning period were included in subsequent analyses of network dynamics. 24 h following CFC or Sham conditioning, freezing behavior upon return to the conditioning context was measured to evaluate CFM.

Pharmacogenetic Inhibition of Interneurons

2-3-month-old male Pvalb-IRES-CRE mice were bilaterally injected with either the inhibitory receptor hM4Di (rAAV2/Ef1A-DIo-hM4Di-mCherry; UNC Vector Core: Lot #AV4,708) or a control mCherry reporter (raav2/Ef1A-DIo-mCherry; UNC Vector Core: Lot #AV4375FA) (methods further elaborated in [131]**.** Using the same implant procedures described above, the animals were implanted with stereotrode bundles.

After allowing 4 weeks for viral expression, the animals underwent contextual fear conditioning (as described above). Post-shock, mice were either given an i.p. injection of

either 0.3 mg/kg clozapine-N-oxide (CNO) dissolved in DMSO (to activate the DREADD) or DMSO alone (as a control).

3.2.2 Computational Modeling

Mixed Excitatory-Inhibitory Conductance-based Neuronal Networks

Conductance-based neuronal networks containing both excitatory and inhibitory neurons were modeled using a modified Hodgkin-Huxley formalism[156,158]. The time-dependent voltage V_i of a single neuron is given by

$$C_m \frac{d}{dt} V_i = -I_{Na} - I_K - I_{K_s} - I_{leak} + I_{ext} - I_{Synaptic} + I_{noise} \quad \text{(III.1)}$$

where C_m is the membrane capacitance, I_{ext} is the fixed external input (DC) used to elicit spiking; $I_{ext} \in [1.08,1.2]$ for excitatory cells and $I_{ext} \in [-0.09, -0.08]$ for inhibitory cells; $I_{leak} = 0.02(V_i + 60)$ is the leakage current, and $I_{Synaptic} = \left(\sum_{j \in Excitatory} g_{E-X} S_{ij}\right)(V_i - V_{Excitatory}) + \left(\sum_{j \in Inhibitory} g_{I-X} S_{ij}\right)(V_i - V_{Inhibitory}) \in [-0.09, -0.08]$ is the total summed synaptic input received by a neuron from its pre-synaptic partners and g_{I-X} and g_{E-X} represent the synaptic conductance for connections from inhibitory and excitatory neurons to their post synaptic targets X (values provided below). The synaptic reversal potentials are $V_{Excitatory} = 0\ mV$ and $V_{Inhibitory} = -75\ mV$. Here, $S_{ij} = \exp\left(-\frac{\Delta t_{ij}^{spk}}{\tau_s}\right) - \exp\left(-\frac{\Delta t_{ij}^{spk}}{\tau_f}\right)$ represents the shape of the synaptic current, given the difference in spike timing between the post-synaptic neuron i and the recently fired pre-synaptic neuron j, Δt_{ij}^{spk}, with $\tau_f = 5\ ms$ and $\tau_s = 250\ ms$ or $\tau_s = 30\ ms$ for excitatory synaptic currents and inhibitory synaptic currents, respectively.

The ionic currents are $I_{Na},\ I_K, and\ I_{K_s}$, representing sodium (Na), potassium (K), and muscarinic slow potassium (K_s), respectively. More specifically: $I_{NA} = m_\infty^3 h \bar{g}_{Na}(V_i - E_{Na})$, with $m_\infty = (1 + \exp(\frac{-V_i - 30}{9.5}))^{-1}$ being the activation of the channel and where h, the inactivation, is given by the solution to $\frac{d}{dt}h = (h_\infty - h)/\ \tau_h$, with $h_\infty = (1 + \exp(\frac{V_i + 53}{7}))^{-1}$ and $\tau_h = 0.37 + 2.78\ (1 + \exp(\frac{V_i + 40.5}{6}))^{-1}$; $I_K = g_K n^4 (V_i - V_K)$ with $\frac{d}{dt}n = (n_\infty - n)/\ \tau_n$ where $n_\infty = (1 + \exp(\frac{-V_i - 30}{10}))^{-1}$ and $\tau_n = 0.37 + 1.85\ (1 + \exp(\frac{V_i + 27}{15}))^{-1}$; and $I_{K_s} = g_{Ks} s (V_i - V_K)$ with $\frac{d}{dt}s = (s_\infty - s)/\ 75$ where $s_\infty = (1 + \exp(\frac{-V_i - 39}{5}))^{-1}$,with the time constants being in ms and voltages in mV. The reversal potentials are $V_{Na} = 55\ mV$ and $V_K = -90\ mV$ and the maximal conductances are $g_{Na} = 24\ \frac{mS}{cm^2}$, $g_K = 3.0\ \frac{mS}{cm^2}$.

The slow potassium conductance

$$g_{K_s} = \begin{cases} 0\ \frac{mS}{cm^2} & if\ ACh\ is\ high \\ 1.5\ \frac{mS}{cm^2} & if\ ACh\ is\ low \end{cases} \qquad \text{(III.2)}$$

controls the level of ACh, e.g. during wakefulness (high ACh) or NREM sleep (low ACh). The values thus control the excitability type, where low g_{K_s} (high ACh) yields Type 1 excitability and high g_{K_s} (low ACh) yields Type 2 excitability. Type 1 excitability is characterized by arbitrarily low firing frequencies, high frequency gain as a function of constant input, and a constant advance in the phase response curve whereas Type 2 has a threshold in firing frequency onset, a shallow frequency gain function, and a biphasic phase response curve [158].

The I_{noise} is defined as a short, 1ms step current of an amplitude large enough to elicit single spike on a neuron. The timing of the step current is drawn from a Gaussian distribution so that noise events are applied with a given mean frequency (as noted on Figure III.7). Each simulation was completed using the RK4 integration method with a step size of h = 0.05 ms.

Network Properties

The network used in these studies consists of N=1000 neurons, with $N_e = 800$ excitatory neurons and $N_I = 200$ inhibitory neurons. Connections form a random network with different levels of connectivity dependent on the pairwise pre- and post-synaptic neuron identity: Inhibitory neurons project to 50% of the inhibitory neurons and 30% to the excitatory neurons whereas excitatory neurons project to just 6% of both the inhibitory and excitatory neurons, with self-connections being forbidden in all cases. The initial synaptic weights are $g_{I-I} = 0.0013\ mS/cm2$, $g_{I-E} = 0.0005\ mS/cm2$, $g_{E-I} = 0.00046\ \frac{mS}{cm2}$, and $g_{E-E} = 0.00003\ \frac{mS}{cm^2}$ in Figures III.1 and III.2, but with $g_{E-E} = 0.00001\ mS/cm2$ in Figures III.1-7. For initial engram formation, reciprocal connections among a random subset of 200 excitatory neurons increase their g_{E-E} conductances, constituting the strength of the memory. The effect of the degree of increase in this synaptic strength, and as a function of number of cells affected by this strengthening is investigated in Figure III.2 and elsewhere is kept at 10x.

Separately, to investigate oscillatory pattern formation in a network with no reciprocal excitatory-to-excitatory connectivity (Figure III.1-g-i and Figure III-2.c) we simulated initial

memory formation via changes to the mean external current, I_{ext}, each neuron receives, i.e. the external current was modified from $I_{ext} \in [1.045, 1.1]$. to $I_{ext} \in [1.33, 1.4]$ with input noise of 0.5 hz.

Implementing STDP in the Network

Neural correlates of memory are thought to emerge due to the strengthening and weakening of synaptic strengths in an activity-based manner. Here, we use a symmetric learning rule, implemented via spike timing-dependent plasticity (STDP), that uniformly increases or decreases synaptic weights based on the time-ordering of pre- and postsynaptic pair firings, only in excitatory-to-excitatory connections. If a presynaptic neuron fires before its postsynaptic partner, the conductance increases by an amount $p\exp(-\frac{t_{pre}^{spk}-t_{post}^{spk}}{10})$. Similarly, a weakening of synaptic strength occurs by an amount $p\exp(-\frac{t_{post}^{spk}-t_{pre}^{spk}}{10})$ when a postsynaptic neuron fires before its presynaptic partner. In both cases, if the time difference between spike pairs is too great, the change in synaptic strength will approach zero. On the other hand, highly coincident spike pairs will have a maximal change given by the learning rate $\rho = 10^{-3}$. It should be noted that while the synaptic weight is prohibited from becoming negative, there is no upper-bound set on the synaptic strength, though previous work has shown saturation of synaptic weights given sufficient time [128].

While simulations presented in the main manuscript (Figure III.5) use standard asymmetric STDP rules described above, Figures III. S2 and S3 (in the Appendix at the end of this thesis) use STDP rules symmetrical around the lead/lag of the spike of the

presynaptic neuron, with synaptic strength changes being only positive or negative, respectively.

3.2.3 Statistical Analysis

Analysis of Functional Network Structures through AMD and FuNS

Average Minimal Distance (AMD) [193] was applied to network firing data to determine functional connectivity. AMD calculates the mean value of the smallest temporal difference between all spikes in one neuron and all spikes in another neuron. Analytical calculations of the expected mean and standard deviation of minimal distance is then used to rapidly determine the significance of pairwise minimal distance [194]. Specifically, the first and second raw moments of minimal distance for each node are calculated: $\mu_1^L = \frac{L}{4}$ and $\mu_2^L = \frac{L}{12}$, where L is the temporal length of the interspike interval and we have assumed that (looking both forward and backward in time) the maximum temporal distance between spikes is $\frac{L}{2}$. Over the entire recording interval T, the probability of observing an inter-spike interval of length L is simply $p(L) = \frac{L}{T}$. Then, the first and second moments of minimal distance considering the full recording interval are given as $\mu_1 = \frac{L}{4T}\sum_L L^2$and $\mu_1 = \frac{L}{12T}\sum_L L^3$. Finally, the calculated statistical moments give rise to the expected mean and standard deviation, $\mu = \mu_1$and $\sigma = \sqrt{\mu_2 - \mu_1^2}$, which are used to determine the Z-score significance of pairwise connectivity: $Z = \frac{AMD_{ij} - \mu_i}{\sigma_i}$. Values of $Z_{ij} \geq 2$ represent significant functional connections between node pairs.

Functional Network Stability (FuNS) tracks global changes in network functional connectivity by quantifying similarities in AMD matrices over a recording interval. The procedure is as follows: first, a recording interval is split into n partitions of equal temporal length. Each partition is subjected to AMD functional connectivity analysis, resulting in n functional connectivity matrices, Z.

Similarity between time-adjacent functional networks is determined using the normalized dot product after matrix vectorization. FuNS is then determined by taking the mean of these cosine similarities over the recording interval:$FuNS = \frac{1}{n-1}\sum_{t=1}^{n-1}\frac{<Z_t|Z_{t+1}>}{\|Z_t\|Z_{t+1}\|}$. Thus, FuNS yield insight into how functional connectivity changes over time.

Spectral Analysis, Spike-Field Coherence, and Phase Relationships

Histograms of neuronal firing per unit time were used to calculate the network characteristic frequency, spike-field coherence, and phase relationships of individual neurons to the network signal. First, spike timings were converted into binary spike vectors and then summed to give a network spike vector. Then, the spike vector was convolved with a Gaussian distribution with zero mean and a standard deviation of ~2 ms, giving a continuous network signal. The spectral power was measured by taking the Fourier transform of the excitatory, non-engram signal (i.e. no neurons with artificially strengthened connections were used; Figure III.1). Then, the change in spectral power (e.g., in Figure III.2) was calculated by integrating the frequency-domain signals and taking the relevant percent difference.

Finally, phase relationships of excitatory neuron firing compared to inhibitory local field potentials was calculated (please see Figure III.3A). Peaks in the inhibitory signal acted as the start and end of a given phase and excitatory spike times were used as place-markers of phase between an individual neuron and the signal. The phase of spike occurrence was normalized to give values between 0 and 1.

Burst Detection

We analyzed bursts of activity for firing asymmetry between active neurons. First, recordings of a given interval of length L were segmented into smaller windows of length x (25 ms in CFC, 50 ms in CNO/DMSO, and 100ms in model simulations; with times chosen to maximize number of pairwise co-activations occurring) with windows overlapping by 12.5 ms to increase the sampling of the interval L and to reduce effects of windows onset. Then, the total number of **active neurons**, in each window is determined and used to define a burst-detection threshold: a burst occurs if the activity in a window is significantly greater than the mean background activity, averaged over all intervals of a given vigilance state. Specifically, if a window $\boldsymbol{w_i}$ has a corresponding number of active neurons $\boldsymbol{k_i}$, then the set of windows representing bursts over all intervals is given as $\boldsymbol{B} = \{\boldsymbol{w_i}|\boldsymbol{k_i} \geq \boldsymbol{\mu_k} + \boldsymbol{2\sigma_k}\}$, where $\boldsymbol{\mu_k}$ and $\boldsymbol{\sigma_k}$ are the mean and standard deviation across all w.

Firing Asymmetry Calculation

Next, the pairwise firing asymmetry A is calculated across all detected bursts, where A is an $N \times N$ matrix with entries $\boldsymbol{A_{m,n}} > 0$ if the spikes of neuron m occur before the spikes of

neuron n on average, and $\boldsymbol{A}_{m,n} < 0$ in the opposite case. The exact value of an entry $\boldsymbol{A}_{m,n}$ is given as the normalized sum of fractional differences between the number of spikes of neuron n occurring after and before each spike of neuron m, across all detected bursts B:

$$\boldsymbol{A}_{m,n} = \left(\frac{1}{B_{m,n}}\right) \sum \sum \frac{(T_{n>m} - T_{n<m})}{(T_{n>m} + T_{n<m})} \quad \text{(III.3)}$$

Where $T_{n>m}$ represents the number of spikes of neuron n occurring after a given spike of neuron m, the inner sum is over the number of spikes of neuron m within a given burst, the outer sum is over all bursts, and the normalization factor, $B_{m,n}$, is the total number of bursts where neurons n and m are coactive.

Relating Firing Asymmetry to Phase Coding of Activation Frequency

The rows and columns of A are sorted by neuronal firing rate measured within a given vigilance state (i.e. wake or NREM). After sorting, firing asymmetry of slow firing rate neurons compared to high firing rate neurons will (a) compose the lower triangular matrix of A and (b) will be more positive than the upper triangular matrix of A if faster firing neurons lead slower firing neurons. We thus compared each pairwise entry of $A_{m,n}$ in the lower triangular matrix with its reciprocal $A_{n,m}$ in the upper triangular, $\widetilde{\boldsymbol{A}}_{\boldsymbol{m,n}} = A_{m,n} - A_{n,m}$. If $\widetilde{\boldsymbol{A}}_{\boldsymbol{m,n}} > \boldsymbol{0}$,then the faster firing neuron leads the slower firing neuron on average.

We next determined the significance of each $\widetilde{\boldsymbol{A}}_{\boldsymbol{m,n}}$ by randomizing the timing of each neuron's spikes within each burst, 100 times (i.e. bootstrapping). The value of significance

is then given by the Z-score, $\boldsymbol{Z}(\widetilde{\boldsymbol{A}}_{\boldsymbol{m,n}}) = \frac{\widetilde{\boldsymbol{A}}_{\boldsymbol{m,n}} - \boldsymbol{\mu}(\widetilde{\boldsymbol{A}}_{\boldsymbol{m,n}})_{\boldsymbol{randomized}}}{\boldsymbol{\sigma}(\widetilde{\boldsymbol{A}}_{\boldsymbol{m,n}})_{\boldsymbol{randomized}}}$ Where $\boldsymbol{\mu}(\widetilde{\boldsymbol{A}}_{\boldsymbol{m,n}})_{\boldsymbol{randomized}}$ and $\boldsymbol{\sigma}(\widetilde{\boldsymbol{A}}_{\boldsymbol{m,n}})_{\boldsymbol{randomized}}$ are the mean and standard deviation of the randomized distributions and with $\boldsymbol{Z}(\widetilde{\boldsymbol{A}}_{\boldsymbol{m,n}}) \geq \mathbf{2}$ indicating that neuron m leads neuron n in a significant way (95% confidence interval). In all, we obtain a distribution with $\frac{1}{2}N(N-1)$ elements, where N is number of detected neurons.

Finally, we compare the changes distributions of $\boldsymbol{Z}(\widetilde{\boldsymbol{A}}_{\boldsymbol{m,n}})$ for the investigated cases (Figure III.4 and Figure III.5). For this comparison we take the top 20% of the pairs that fire within the same bursts (as opposed to cells that maybe not active within the same bursts). A positive difference at $\boldsymbol{Z}(\widetilde{\boldsymbol{A}}_{\boldsymbol{m,n}}) \geq \mathbf{2}$ indicates an increase in fast firing neurons leading slow firing neurons within a burst of activity.

Alternatively, instead of calculating the individual pairwise differences in asymmetry, $\widetilde{\boldsymbol{A}}_{\boldsymbol{m,n}}$, a global assessment of asymmetry is achieved by first averaging all the individual asymmetry values below the m=n diagonal (i.e. $< \boldsymbol{A}_{\boldsymbol{m,n}} >$, where $m < n$) and subtracting the average value from above the m=n diagonal (i.e. $< \boldsymbol{A}_{\boldsymbol{m,n}} >$, where $m > n$). Bootstrapping of spike times within bursts can then be used to determine significance of this difference, with positive values greater than or equal to a value of 2 indicating a significant global increase in fast firing neurons leading slow firing neurons within the network (Figure III.4F).

Determining Significance of Firing Asymmetry Distributions

The firing asymmetry Z-score distributions were tested against asymmetries across the same distribution but calculated using randomized spike times. For each mouse, once bursting architecture is determined (i.e. number of bursts given interval), asymmetry was calculated using randomized spike timings. Asymmetries were then used to determine significance distributions as outline above and this process was repeated and then averaged over 25 runs. The averaged Z-score distribution is then compared to the standard, real asymmetry Z-score distribution to determine significance, using a two-sided t-test.

3.3 Results

3.3.1 Memory Stabilization via Synaptic and Input Heterogeneity after NREM Sleep

We used a highly reduced in silico model network (with generic features) to determine whether ACh dependent muscarinic pathway may drive changes in network dynamics at the transition from wake to NREM sleep, in a universal way. We compared the *in silico* results with experimental recordings from hippocampal area CA1 following single-trial contextual fear conditioning (CFC) [195,196] – an experimental model system to investigate how network activity changes during memory encoding affects subsequent network dynamics. We analyzed both in silico and experimental in vivo recordings from CA1 to determine how functional network dynamics were affected by de novo memory formation.

ACh is known to regulate intrinsic neuronal membrane excitability, primarily through regulation of muscarinic receptors - when opened these receptors activate slow,

hyperpolarizing potassium current. These receptors [197] are also present in CA1 [198]. In isolation, during wake-like state, high ACh blocks this current in excitatory neurons, which increases firing frequency responses to excitatory input (i.e. steepness of the Input-Frequency curve) and decreases neuronal propensity to synchronize which is mediated by the shape of the phase response curves (PRC) (i.e., type 1 excitability) [158,199].

Consequently, during wake-like state (high ACh, low conductance of m-current, g_{K_s}), neurons behave as integrators to the incoming stimuli, responding to changes in input by sharply modulating their firing frequency (steep input-firing frequency (IF) curve). Thus, in this regime the neurons respond to the magnitude of their (external or network) input by modulating their frequency[128]. On a network level, this results in highly heterogenous neuronal firing frequencies and reduced synchronizabilty of neuronal spiking.

In contrast, low ACh during NREM sleep-like state allows slow potassium current (m-current) to play a larger role in membrane excitability, leading to spike frequency adaptation, reduced spike frequency response gain (i.e., a flat IF curve), subthreshold oscillations at theta band frequency, increased synchronization capacity (i.e., type 2 excitability) and emergence of slowly moving waves of excitation resembling slow waves [87]. In this case, the neurons tend to spike with similar frequency across wider range of inputs, and lock to intrinsic or extrinsic oscillatory drive, especially if the oscillatory drive occurs at a resonant frequency. This leads to emergence of large-scale slow oscillations,

where the magnitude of cell input is coded via relative phase of firing of neurons rather than frequency [157].

To investigate mechanisms involved in sleep-dependent aspects of memory consolidation, we simulated a reduced neural network model composed of excitatory principal neurons and inhibitory interneurons. For cells in the model, we used a conductance-based formalism (see Section 3.2) incorporating a slow-varying potassium current which acts as a control parameter for neuronal firing dynamics[158]. Here, sleep/wake dynamics are mimicked by switching excitatory neurons from type 2 membrane excitability (NREM sleep) to type 1 excitability (wake), resulting in neuronal excitability change from integrator type response during wake, into resonator type response during NREM sleep. Since the muscarinic response of interneurons to ACh is complex and heterogeneous [66,200] we set inhibitory interneurons in the model to exhibit consistent type 1 dynamics (although permitting type 2 dynamics in interneurons yielded similar results).

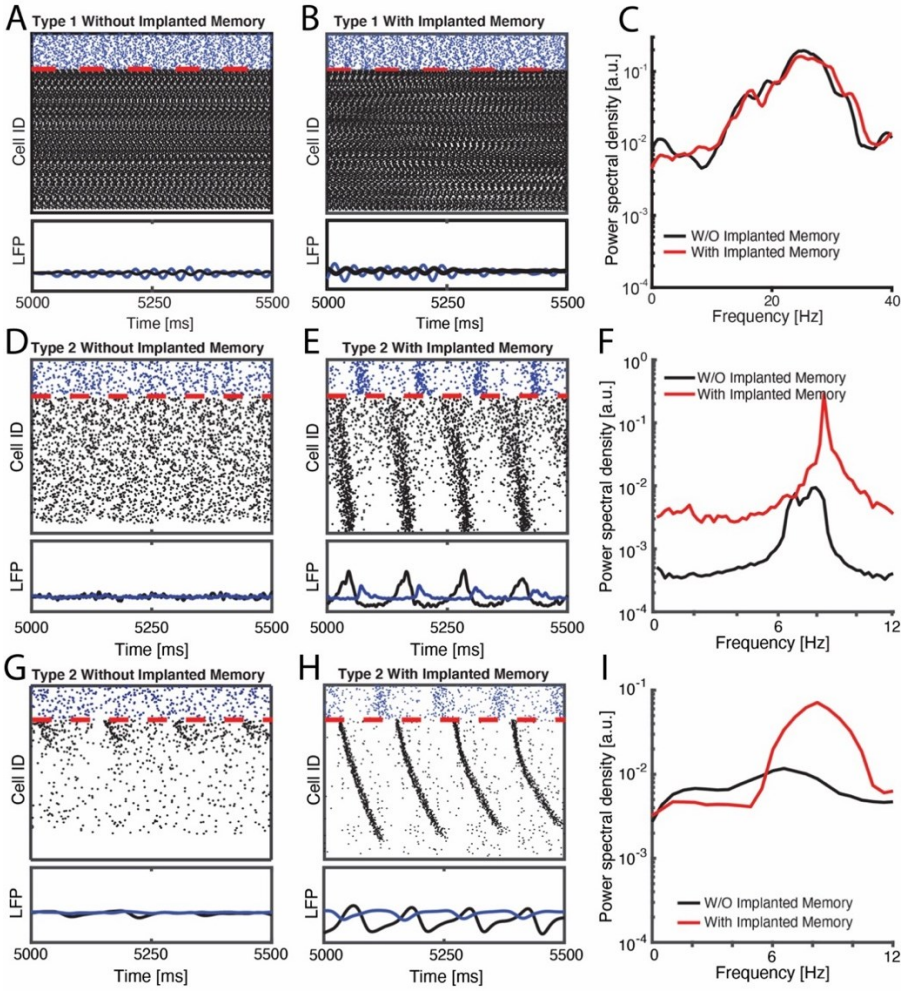

Figure III.1 Type 2 model networks respond to sparse strengthening of excitatiory synapses or increasing excitatory input through emergence of low-frequency rhythms and phase-locking.

SIMULATED DATA: Raster plots (top) and cumulative signal (bottom) generated by inibitory (blue), and excitatory (black) neurons in a REM-like (high-ACh) state before **(A)** and after **(B)** initial memory storage. **C)** Fourier transform of the REM-like excitatory network signal before (black) and after initial memory storage (red) reveal enhanced beta/gamma oscillations. **(D, E)** raster plots (top) and cumulative signal (bottom) of NREM-like (low-ACh) state before **(D)** and after **(E)** initial storage (i.e. 20 fold strengthening of recurrent synapses between pairs of 25% of excitatory engram neurons). **F)** Fourier transform of the NREM-like excitatory network signal before (black) and after initial memory storage (red) reveal enhanced slow oscillations in theta range. **(G, H)** raster plots (top) and cumulative signal (bottom) of NREM-like (low-ACh) state in a network with removed reciprocal excitatory synapses, before **(G)** and after **(H)** initial storage (i.e. 5% increase in the mean external drive, I_{ext}, to excitatory engram neurons). **I)** Fourier transform of the NREM-like excitatory network signal before (black) and after initial memory storage (red) reveal enhanced slow oscillations in theta range. On all rasterplots neurons are order as a function of their frequency in WAKE-like state.

Thus, here the “memory” is represented by a configuration of input patterns (either external to the network [applied via external current, I_{ext}; see Section 3.2] and/or internal ones driven by reciprocal synaptic connectivity), which alter the neurons’ relative frequency of firing during wake-like dynamics, or their relative phase relationships during NREM-like dynamics of the network.

Here we focused on pattern consolidation during NREM-like state in response to the memory trace being acquired during wake-like state. The predictions stemming from this consolidation in the model were closely compared with the in vivo data. To this effect, within the model we divided information storage into two phases. In the first, activation of subset of engram neurons by external input (during wake) results in rapid strengthening of connections between them a process we refer to as “initial storage” hereafter. This process results in strengthened connections between these subset to cells (i.e. network heterogeneity), in the second phase, off-line network reorganization and consolidation is driven by STDP in a NREM-like state which we refer to as “NREM dependent consolidation/reorganization”.

Critically, the recurrent excitatory connections within CA1 may be relatively few compared to other structures (although this is a matter of debate) [201] which could limit the usefulness of our reduced model with more generic synaptic connectivity. To verify that these findings generalize to a network without substantial recurrent excitatory connections, we repeated these experiments in a model network without excitatory-to-excitatory connections but with modulating external excitatory input, I_{ext}, to the excitatory

network neurons. In this scenario, which would mimic learning-associated changes to CA1 excitatory input from CA3 alone.

Within this framework, we first investigated how strengthening excitatory synaptic connections between a limited subset of neurons, or changes in the external drive I_{ext}, events analogous to initial learning, affect network activity patterns during subsequent NREM sleep (i.e. low ACh/high g_{Ks} dynamics). Figure III.1 depicts examples of raster plots, simulated LFPs, and their Fourier transforms for three cases: 1. when the network dynamics simulates waking state (i.e. high ACh dynamics, Figure III.1A-C), 2. When network dynamics simulates NREM sleep state, with memory encoded via strengthening of existing excitatory-to-excitatory connections (i.e. low ACh state, Figure III.1D-F), and 3. when network dynamics simulates NREM state, with memory encoded via modulation of the mean external input to the excitatory cells (Figure III.1G-I). Comparing raster plots (top**)** and simulated local field potentials (LFPs; bottom) for the network when excitatory neurons exhibit type 1 (wake; Figure III.1A, B) and type 2 (NREM, Figure III.1D, E) dynamics, before vs. after initial storage, reveals the emergence of well-defined slow-band oscillations (which are evident in periodic firing patterns of both excitatory and inhibitory neurons in the network) only in NREM-like state (Figure III.1E) but not wake-like state (Figure III.1B). In addition the wake-like network state exhibits oscillatory response in high beta/low gamma oscillatory range (Figure III.1C). Thus only during NREM-like state does the initial storage lead to an increase network-wide low frequency spectral power (Figure III.1F), consistent with previous in vivo work [131,191] The neurons on the y-axis of the plots were ordered so that excitatory neurons receiving the

highest excitatory drive were placed on the top and the ones receiving the lowest excitatory drive were place on the bottom. Please note the order of firing within the oscillatory burst, with the neurons receiving larger excitatory input firing first and the neurons receiving smaller excitatory input firing relatively later within the same burst.

From a dynamical perspective this phenomenon is easy to explain and is universal across biological and physical systems[202]. It is a well-established phenomenon that oscillators exhibiting somewhat different natural firing frequency lock with a phase-shift where intrinsically faster oscillators lead while slower oscillators lag. Here this natural firing frequency is input dependent.

Similar effect is observed when excitatory-to-excitatory connections are missing, and the memory is encoded via strengthening the mean external input to the excitatory cells (Figure III.1G-I). Here however the mechanism is somewhat different, since synchronization cannot be supported via (non-existent) excitatory-to-excitatory connections. The external inputs interacting with subthreshold membrane oscillations trigger excitatory burst, with the relative phase of spiking of a given cell dependent of the magnitude of this input. This burst in turn activates inhibitory burst which resets the excitatory cells for the next cycle.

We note that the frequencies obtained for slow oscillations are primarily in theta band, whereas the frequencies observed in NREM sleep are usually lower [114]**.** This is due to highly reduced nature of the model, as here the detailed differences in peak frequency

between the model and in vivo recordings are due in part to specific cellular resonance properties of neurons in the model network [128]. We show in supplementary material (Figure III.S1 in the Appendix at the end of this thesis) that this frequency can be modulated via, for example, inhibitory network connectivity strength and time constant of activation of inhibitory postsynaptic potentials (IPSPs) associated with additional membrane currents which this model does not take into account.

The critical component here that drives the observed phenomena is mediated via homogenization of spiking frequencies and switch to type II dynamics regulated by activation of m-current due to low ACh levels, that in turn results in temporal organization of the network burst. Thus while resonant frequencies may vary by circuit, we hypothesize that this enhancement of coherent network oscillations (which has been widely reported in both human subjects and animal models following learning) [114] could drive STDP-based information storage in the network.

3.3.2 NREM Hippocampal Network Stabilization In Vivo Predicts Successful Fear Memory Consolidation

Next, we investigated how the magnitude of synaptic strength modifications, or the magnitude of changes of external drive to excitatory cells, taking place during initial learning subsequently affects functional network stability (FuNS) and network oscillations during sleep.

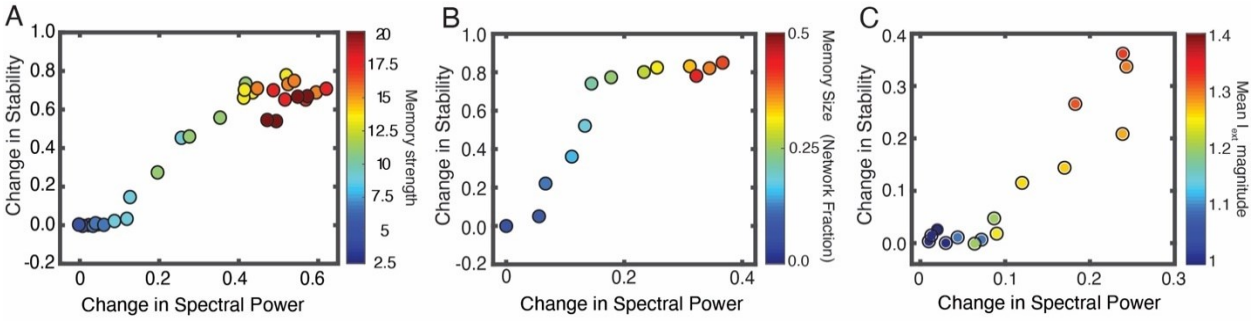

Figure III.2 Memory-driven changes in network stability.

Change in functional network stability (FuNS) and spectral theta power in response to strengthening of subset of reciprocal excitatory-to-excitatory connections **(A)** (color scale corresponds to synaptic multiplier), **(B)** different number of cells undergoing initial synaptic strengthening (color scale corresponds to fraction of cells that had strengthened incoming synapses), **C)** change in mean external current, I_{ext},received by excitatory neurons in absence or reciprocal excitatory-to-excitatory connections. In A the fraction of network th synapses strengthened was 25%; in B the strengthening multiplier was set to 20.

We measured these two quantities as a function of strength of reciprocal excitatory connections between engram neurons, the number of connections that are being strengthened, and separately, in absence of excitatory-to-excitatory connections, as a function of mean external drive, I_{ext}, to excitatory cells. Here, FuNS measures stability of functional connectivity between neurons, using the functional network stability metric (FuNS; see Section 3.2) [128].

First, in silico, we simulated networks in NREM-like state (low ACh, high g_{Ks}), with differential exposure to initial storage (i.e., strengthening reciprocal excitatory connections among subset of engram neurons as described above (Figure III.2A), increasing the subset of neurons that are exposed to such a strengthening (Figure III.2B), or increasing mean external drive, I_{ext}, to the excitatory cells (Figure III.2C). We measured change in theta band power and functional network stability (FuNS; see Section 3.2) as a function of synaptic strengthening within the subset of engram cells (Figure III.2A) and the number of cells undergoing this strengthening (Figure III.2B) or magnitude of mean I_{ext} (Figure III.2C). With increasing memory strength as well as the sub-group size, we observed rapid increase in both FuNS and oscillatory power in the model network (Figure III.2A, B). This suggests that learning in the network directly augmented both network oscillations and stabilization of functional connectivity patterns in subsequent NREM sleep. While the multiplier magnitude may seem unrealistically large one needs to consider the size of the network and sparsity of these connections in the model. With the increased size/connectivity the multiplier will not need to be as high to achieve the same effect.

We have also observed significant increase in both FuNS and oscillatory power in the model network, when the mean value of I_{ext} was increased (Figure III.2C). However, the mean change in stability was not as pronounced for higher levels of I_{ext} as when excitatory-to-excitatory connections were present in the network. That leads us to hypothesize that existence of even sparse excitatory-to-excitatory connectivity within CA1 increases stabilization of the output pattern of excitatory cells.

Next we compared our modeling results with the experimental data. To model effects of post-learning sleep deprivation (SD; high ACh, low g_{Ks}), excitatory neurons were set to type 1 excitability in the presence of an implanted memory. To model interactions between learning and subsequent sleep, NREM (low ACh, high g_{Ks}) was mimicked by setting excitatory neurons to type 2 excitability, in the presence or absence of initial connection strengthening (Learning and Sham, respectively). When the initially strengthened engram was present in networks with type 2 excitability, the network exhibited more stable network dynamics over time (Figure III.3A). Conversely, type 2 “sham” networks (i.e. without initially strengthened engram) and type 1 networks with strengthened engram showed no change in stability.

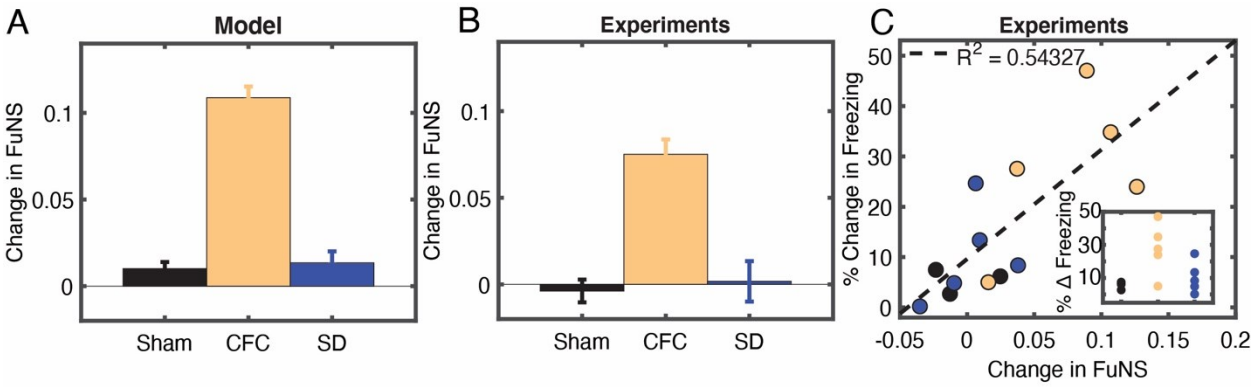

Figure III.3 Functional network stability during NREM after initial exposure predicts future level of memory consolidation.

A) SIMULATED DATA: Model predictions for the change in FuNS in each simulation group: Sham (NREM states without learning; n = 5) and SD (Wake states with learning; n = 5) show only marginal changes in FuNS whereas CFC (NREM states with learning; n = 5) show a maximal increase in FuNS. All error bars represent the standard error of the mean. **B) EXPERIMENTAL DATA**: FuNS analysis of CA1 recordings following CFC or Sham conditioning (Sham conditioned — black [n = 3] , CFC + SD — blue [n = 5], CFC + sleep – yellow [n = 5]). Ad lib sleep post conditioning leads to the greatest increase in FuNS. **C)** EXPERIMENTAL DATA: Change in FuNS for each mouse after CFC predicted its memory performance 24 h later (% freezing; raw values shown as inset). Line indicates best fit to data with $R^2 = 0.54$.

We next tested how these features are affected during sleep-dependent consolidation of CFM in vivo. Mice either underwent single-trial CFC (placement into a novel environmental context, followed 2.5 min later by a 2-s, 0.75 mA foot shock; n = 5 mice), sham conditioning (placement in a novel context without foot shock; Sham; n = 3 mice), or CFC followed by 6 h of sleep deprivation (SD; a manipulation known to disrupt fear memory consolidation [131,189,190] ; n = 5 mice). We measured changes in FuNS in these recordings after each manipulation by quantifying FuNS on a minute-by-minute basis over the entire pre- and post-training 24-h intervals and calculating their respective difference within each animal. Consistent with previous findings [203]**,** we observed a significant increase in FuNS over the 24 h following CFC during NREM sleep (Figure III.3B). In contrast, no change in NREM FuNS was seen in Sham mice or following CFC (during recovery NREM sleep, which is insufficient for CFM consolidation) in SD mice.

Group differences in NREM FuNS were reflected in the behavior of the mice 24 h post-training, when context-specific fear memory was assessed (inset Figure III.3C, inset). Mice allowed ad lib sleep following CFC showed significantly greater freezing behavior when returned to the conditioned context than did Sham or SD mice. Moreover, CFC-induced changes in NREM-specific FuNS for individual mice predicted context-specific freezing during memory assessment 24 h later (Figure III.3C). Thus, successful consolidation of a behaviorally-accessible memory trace in vivo is accompanied by increased NREM FuNS in the CA1 network.

Together, these results led us to hypothesize that oscillatory patterning could promote successful STDP-based consolidation of a hippocampal memory trace. We focus on this phenomenon in the following sections.

3.3.3 Temporal Organization of Firing in Network Oscillations is a Predictor of Sleep-Dependent Firing Rate Reorganization via STDP

A series of recent studies have demonstrated that neuronal firing rates are renormalized across a period of sleep, with highly active neurons in a circuit reducing their firing rates, and sparsely firing neurons increasing their firing rates [123,124,204] Sleep is essential for these firing rate changes, which do not occur across a period of experimental sleep deprivation[124]. We hypothesized that this phenomenon results from STDP driven by neurons phase-locking their firing to NREM sleep oscillations. Specifically, we predict that neurons that are highly active during wake will fire at an earlier phase within an oscillation than neurons with sparser firing.

To test this, we first calculated phase of firing of every excitatory neuron with respect to inhibitory LFP oscillations in silico (see Figure III.4A and Section 3.2). Figure III.4B illustrates the relationship between model neurons' phase of firing calculated during type 2 dynamics as a function of the normalized frequency during type 1 dynamics. We observed that the fastest firing neurons during waking (type 1) fire earlier in the phase of the excitatory network oscillation during NREM sleep (type 2). This suggests that neurons take on a phase-based, temporal coding strategy during NREM network oscillations which reflects differences in firing rate present during wake.

As previously mentioned, this is a universal phenomenon where generalized oscillators having faster natural frequency precede those with lower natural frequency when the two oscillators are coupled and their phase evolution is locked [202]. Here, during wake (high ACh state) the neurons exhibit type 1 dynamics - characterized by reduced capacity to synchronize[205], and relatively larger natural frequency differences (due to steepness of the Input current-spiking Frequency (I/F) curve) [157]. This effectively prevents neural synchronization with neurons that get higher input firing with higher frequency. Upon the switch to NREM like dynamics (low ACh state) the neurons switch to type 2 dynamics, which in contrast, is characterized by higher synchronizing capacity and reduced (but still present) natural frequency mismatch, due to flattened I-F curve. This dynamical state allows neurons to synchronize with the lead/lag pattern determined by the relative magnitude of the input individual neurons receive. Thus, as long as relative input patterns across wake sleep cycle stay the same the frequency during wake will be mapped onto the relative phase during NREM sleep.

To investigate whether this universal phase-locking phenomenon can be observed experimentally, we compared in silico and in vivo network dynamics during wake and during NREM, for CFC and sham situations. In silico sleep-dependent pattern consolidation was modeled through standard spike timing dependent plasticity (STDP) [20,126,206]. To that effect, we developed a metric to measure frequency-dependent phase-of-firing relationships between pairs of CA1 neurons by quantifying their spike timing asymmetry within bursts of activity (for a full description, see Section 3.2). Briefly,

in CFC and Sham hippocampal recordings, we first detected network bursts of firing across CA1 during NREM sleep. Within these bursts, we calculated the frequency dependent firing asymmetry between neurons -i.e., whether, statistically, neurons which fire faster during wake also show more advanced (i.e., leading) firing phase during NREM sleep. Namely, for each recording, we defined an asymmetry matrix A, an NxN matrix whose rows and columns were ordered by the relative firing rate of neurons during wake (Figure III.4, see Section 3.2 for details)

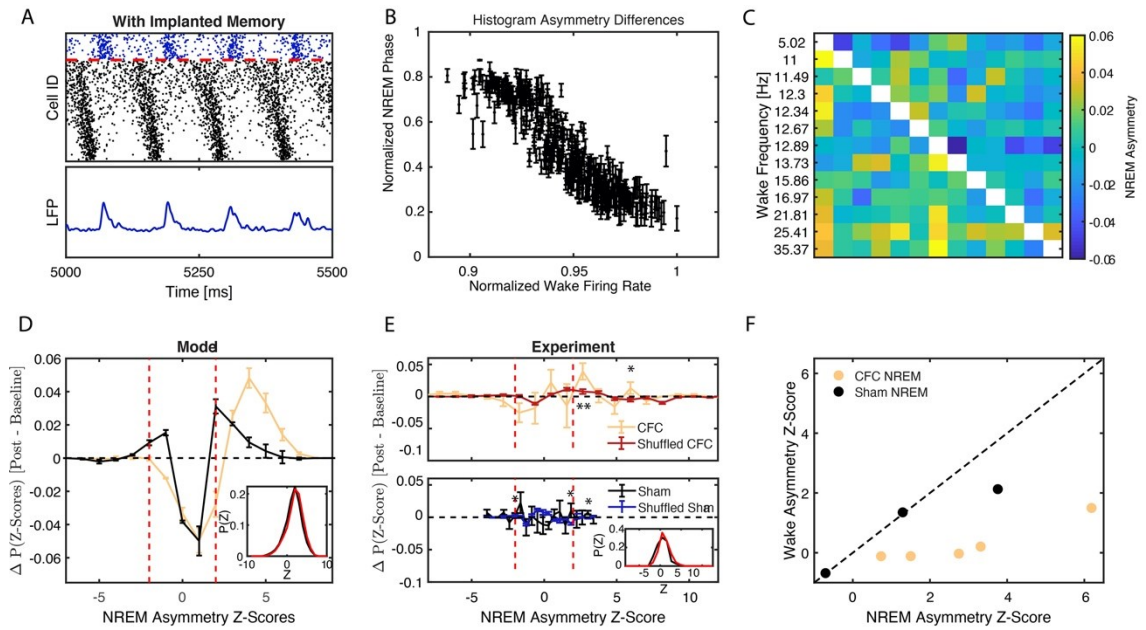

Figure III.4 Mapping relative firing frequency distributions during wake onto firing phase relationships during NREM sleep.

A) MODEL DATA: Calculation of mean phase of firing relative to oscillatory signal generated by inhibitory population; peaks in the inhibitory signal are used as the starting points of the phase calculation. **B) MODEL DATA:** Normalized phase of firing in NREM versus normalized wake frequency of excitatory neurons reveals that the neurons firing with the highest frequency align with an earlier phase of the excitatory network population whereas slower firing neurons align with later phases. **C-F)** Analysis of NREM firing asymmetry reveals enhanced wake frequency-dependent temporal relationships between neurons after learning. **C) EXPERIMENTAL DATA:** Formation of a pairwise firing asymmetry matrix of CA1 neurons' activity recorded from a representative mouse during post-CFC NREM. Rows and columns have been arranged by wake frequency; color denotes pairwise firing asymmetry as defined in the section 3.2. **D) MODEL DATA:** Weighted average of differences in distributions (see inset for a representative example scenario; black—baseline, red—post) of pairwise Z-scores for models with type 2 dynamics and learning (yellow) and with type 2 dynamics and no learning (black). **E) EXPERIMENTAL DATA:** Weighted average of differences in distributions (see inset in bottom panel for example of representative mouse; black—baseline, red—post) of pairwise Z-scores for NREM of CFC mice (top, yellow) and Sham mice (bottom, black), compared to differences in distributions calculated on random spike data following CFC (red, top) or Sham (blue, bottom) bursting architecture. **F) EXPERIMENTAL DATA:** Significance (Z-score) of global NREM network asymmetry vs. that of global wake asymmetry calculated for individual CFC (yellow) and sham (black) mice. Strong asymmetry is observed in NREM sleep but not in wake. ed dashed lines in (D, E) represent the significance cutoff of |Z|>2. Error bars denote SE of repeated simulations (D) or SE across all experimental animals (E). $p<0.05$, ** $p<0.001$ using two sided test.

We determined the significance, Z_{ij}, of asymmetry for every pair, A_{ij}, via bootstrapping and compared the normalized histograms of Z_{ij} (see representative examples from simulated data, Figure III.4D inset) from a network undergoing STPD when: 1) an engram was partially strengthened (initial storage - model CFC, Figure III.1D) and 2) when it was not (model sham, Figure III.1C). The distributions show stronger skewing towards significant (Z > 2) asymmetry pairs after NREM state STDP (with respect to baseline dynamics), for CFC-like engram strengthening (Figure III.4D – yellow line**)** in a sham (no engram strengthening) condition (Figure III.4D – black line).

We next compared in silico results to the experimental distributions obtained from wake and NREM for CA1 recordings from experimental CFC and Sham groups, and found similar results (Figure III.4E). Figure III.4E**,** shows the experimental differences between baseline and post-learning distributions for CFC (Figure III. 4E, top panel) and Sham (Figure III. 4E, bottom panel). Significance values for these distributions were calculated by comparison with randomized distributions ("shuffled CFC" and "shuffled sham"), where the bursting architecture between non-randomized and randomized sets was conserved (see **Section 3.2**). Greater significance occurs for positive Z-values following CFC (Figure III.4E; top - yellow line) as compared to sham (Figure III.4E; bottom - black line), indicating that there is a shift in asymmetry during fear memory consolidation.

These distributions qualitatively resemble the ones obtained in silico (Figure III.4D) and show that consolidation after CFC increases the number of neuron pairs with consistently

significantly asymmetric firing patterns (Z > 2) during NREM (Figure III.4E; top - yellow line), as compared to sham (Figure III.4E; bottom- black line). This indicates the presence of a phase-coding mechanism during NREM sleep, which is sensitive to neuronal and network activity changes caused by initial storage in wake.

To ensure that the shift in pairwise Z-score distributions is not a simple reflection of firing frequency differences between neuronal pairs in NREM, we measured global asymmetry across the network during NREM as a function of firing frequency during wake, for every animal separately. To do this we calculated a mean asymmetry score by subtracting the mean asymmetry of the upper triangle and lower triangle of the asymmetry matrix (Figure III.4C). We then subjected the result to bootstrapping to estimate its significance. We next reversed the calculation and repeated the asymmetry calculation now for burst-ordering detected during wake, as a function of firing frequency during NREM (i.e., calculation that would indicate reverse hypothesis - relationship between phase coding in wake and frequency coding in NREM). These results are depicted in Figure III.4F, where we plot the significance of NREM asymmetry vs. wake asymmetry. We observe that following CFC (but not sham conditioning), all animals have higher significances for NREM asymmetry as compared to the reversed wake asymmetry.

Based on this relationship, we hypothesized that due to the resulting firing phase relationships in NREM, STDP in this context would cause: 1) excitatory connections from high-firing to low-firing neurons to be strengthened, and 2) connections from low-firing to high-firing neurons to be weakened.

3.3.4 Network Oscillations Promote Temporal Coding During Sleep

We hypothesize that via STDP, network oscillations - which are naturally augmented during post-learning NREM sleep - play a crucial role in driving memory consolidation. To test this, we next investigated how disruption of network oscillations affects phase-coding mechanisms. In our model neural network, following the experimental manipulation [191] we first prevented a fraction of inhibitory neurons from firing in the network after initial storage (i.e. partial engram strengthening; Figure III.5A-D). We observe that disruption of progressively larger fraction of inhibitory neurons decreases the numbered of neurons entrained into oscillatory dynamics (Figure III.5A-D).

We next measured the effect that the complete disruption of inhibitory firing (Figure III.5A) has on post-learning firing asymmetry (Figure III.5E). Here we measured differences in distribution of asymmetry of Z-score values between the cases when inhibition was intact (Figure III.5D) and fully disrupted (Figure III.5A). With intact inhibitory neuron activity, the model exhibited significant positive firing asymmetry as compared to disrupted inhibition.

We also analyzed the firing asymmetry of CA1 recordings from mice expressing the inhibitory DREADD (Designer Receptor Exclusively Activated by Designer Drugs) hM4Di in parvalbumin-expressing (PV+) interneurons. These mice were treated with either a vehicle (DMSO) or the hM4Di activator clozapine-N-oxide (CNO, to activate hM4Di and suppress PV+ interneuron activity) immediately following CFC. Previous work has shown that CA1 network oscillations and CFM consolidation are both disrupted by post-CFC inhibition of PV+ interneurons [131,191]**.** We found that disruption of PV+ interneuron

activity with CNO reduced firing rate-associated firing phase asymmetries during post-CFC NREM network bursts relative to DMSO-treated mice, which have normal CA1 oscillations and CFM consolidation (Figure III.5F, black trace). Similar to what was done for CFC vs. Sham data (Figure III.5D), we compared Z-Score distribution to another based on randomized spike times within bursts following DMSO vs. CNO architecture (Figure III.5F, blue trace); we find that the peaks at positive extreme values of the distribution are significant, indicating a greater asymmetry shift in that direction. Thus, for both network models in a type 2 regime and the CA1 network during NREM sleep in vivo, disruption of interneuron-driven oscillations impairs temporal coding.

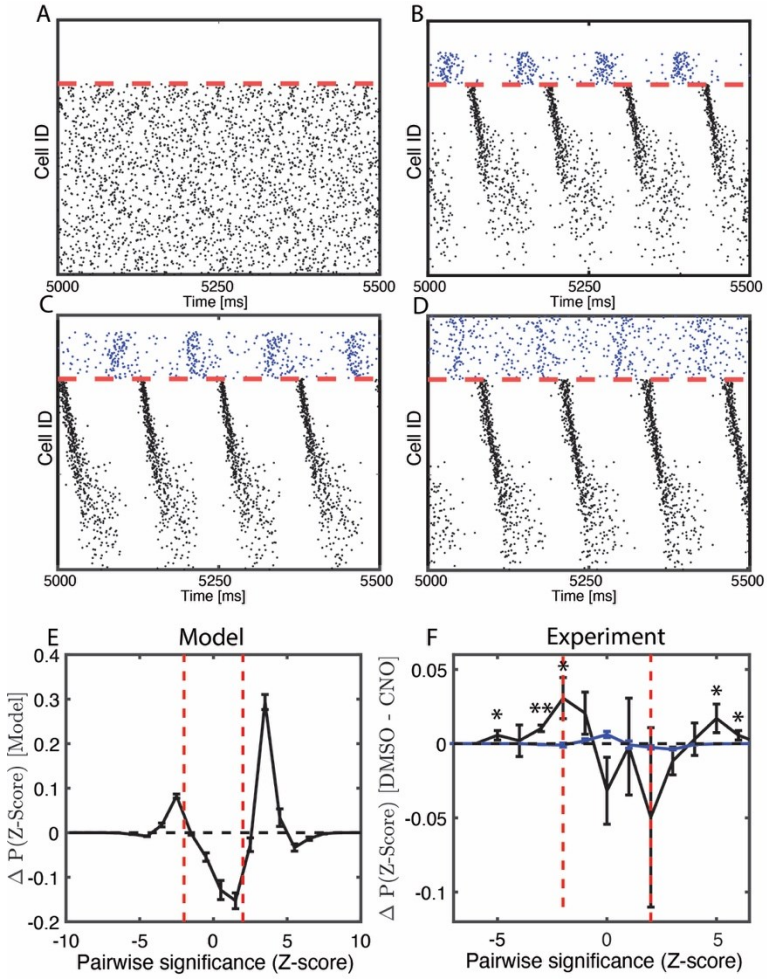

Figure III.5 Disruption of network oscillations diminishes spike timing relationships between neurons. A, B) MODEL DATA: Simulated raster-plots; **A-D)** NREM-like network dynamics for the progressively larger disruption of inhibitory firing. **E)** Weighted sum of differences in model asymmetry significance distributions after consolidation (unperturbed model in (**D**) minus model without inhibition in (**A**)). **F**) **EXPERIMENTAL DATA:** Difference in experimental asymmetry significance distributions, shown as the black trace, for CA1 recordings for mice expressing the inhibitory DREADD hM4Di in PV+ interneurons, treated with either DMSO (analogous to the full model network) or CNO (analogous to reduced network inhibition); compare to randomized spike times used to estimate significance of these values, shown in blue. Error bars denote SEM of repeated simulations (E) or SEM across all experimental animals (F). * $p < 0.05$; ** $p < 0.01$ using a two-sided t-test.

3.3.5 Frequency-Dependent NREM Firing Asymmetry Affects Network Reorganization through STDP

We next examined whether firing rate reorganization occurs during NREM sleep via STDP in the context of firing asymmetries described in the sections above. First, we compared in silico firing rate reorganization between type 2 excitatory networks with and without firing in inhibitory neurons, when synaptic strength could evolve over time using an STDP-like plasticity rule. We examined the changes in wake neuronal firing frequencies after an interval in these two scenarios. In the model with normal inhibitory neuron firing, STDP-based synaptic changes in a type 2 (NREM) regime led to a simultaneous increase in the firing rates of principal neurons with the lowest baseline activity and decrease in the firing rates for the most active neurons (Figure III.6A). We color-coded neurons based on their relative change in frequency across sleep (Figure III.6A top). As shown in Figure III.6 (bottom), neurons which fire faster (vs. slower) during baseline wake-like dynamics (i.e. high ACh, low g_{Ks}; type 1 dynamics) also fire earlier (vs. later) in the oscillation NREM-like dynamics (i.e. low ACh, high g_{Ks}; type 2 dynamics), consistent with Figure III.4, and experience a decrease (vs. increase) in firing rate due to STDP. Some neurons did not fire during NREM and so did not show a firing frequency change due to STDP (black points in Figure III.6A) – this represents selective cell recruitment into the memory engram. Here, this initial firing frequency-dependent frequency change is driven by changes of overall synaptic input (green) to the said cells (Figure III.6B). The cells exhibiting decrease in firing frequency also exhibit overall

decrease in their synaptic input, however their output (black) is significantly strengthened due to timing of firing asymmetries (Figure III.4B). Disruption of network oscillations

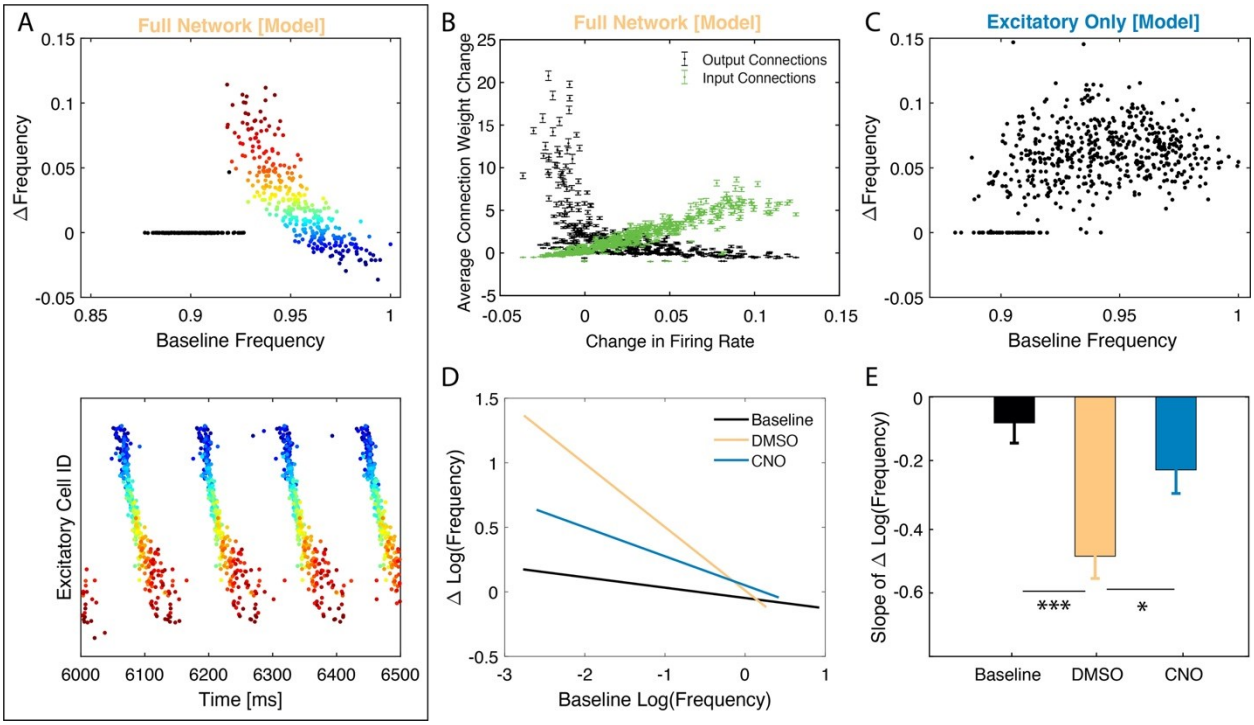

Figure III.6 NREM dependent reorganization differentially affects frequency of firing neurons during wake-like dynamics – model prediction and experiment.

SIMULATED DATA: A) Top: Changes in individual neurons' firing frequency (normalized to baseline) observed during wake-like dynamics recorded across post-learning NREM sleep as a function of normalized baseline firing frequency (top). Conditions comparable to Figure 5D. Colors represent baseline frequency. Bottom: Snapshot of the corresponding raster plot in NREM sleep at the onset of consolidation. Neurons are color-coded based on their baseline frequency during wake like dynamics and the color is conserved in the raster plot. Black data points (top) are for neurons which did not fire during NREM sleep. Of the neurons that are consistently active, those with initially lower frequency increase their frequency whereas neurons with initially higher frequency decrease their frequency. **B)** Average connection weight change for a given neuron vs its frequency change during wake-like dynamics, observed in A. Neurons that increase their firing rate do so due to increased synaptic input, at the same time their mean strength of output connections decreases. **C)** Change in firing frequency (normalized to baseline) as a function of normalized baseline firing frequency in the absence of inhibition. Conditions comparable to Figure 5A. Unlike the full-network condition (with inhibition), firing frequency changes homogenously across baseline firing rates. **EXPERIMENTAL DATA: C)** Best fit lines of the change in log firing rates vs the initial log firing rate, comparing baseline recordings (solid lines; composite n = 11) to post recordings (dashed lines) for the first 6 hours post CFC for mice expressing the inhibitory DREADD hM4Di in PV+ interneurons, treated with either DMSO (Yellow; n = 3; analogous to the full model network) or CNO (Teal; n = 3; analogous to reduced network inhibition), and wild type mice with post-CFC SD (Blue; n = 5). D) Slope comparison of change in log firing rates for DMSO, CNO, and SD baseline and post-CFC recordings. Analysis of covariation revealed statistically significant slope differences between DMSO and CNO (* indicates $p < 0.05$), and DMSO and Baseline (*** indicates $p < 0.0001$).

via inhibitory neuron silencing disrupted the relationship between firing rate changes across the type 2 regime and baseline firing rates for principal neurons (Figure III.6C).

We compared these results with data recorded from the hippocampus of mice with and without DREADD-mediated disruption of PV+ interneuron activity [131,191]. We measured changes in firing frequency across a six-hour time interval at the start of the rest phase (i.e., starting at lights on), either at baseline (i.e., the day before CFC) or in the hours following CFC. Firing rate changes for each neuron were calculated for mice treated with either DMSO or CNO as a function of their baseline firing rate. The resulting best-fit lines (Figure III.6D) reveal that while CA1 neurons show a relatively low degree of firing rate reorganization across baseline rest, following CFC reorganization is more dramatic. The greatest degree of reorganization is seen after CFC in the control (DMSO) condition, with less-dramatic firing rate changes seen in mice with disrupted CA1 PV+ interneuron activity (CNO) (Figure III.6D, E).

Comparing the slopes of firing rate vs. firing rate change relationships in CA1 for post-CFC recordings (Figure III.6E), we found significantly weaker reorganization of firing rates in CNO-treated mice relative to DMSO-treated mice. This reorganization of firing rates across the network is an important prediction of the model, as it suggests a possible universal network-level correlate of sleep-based memory consolidation in vivo.

Here we have used a standard asymmetric STDP rule, where synapses are strengthened when presynaptic neuronal firing leads firing in the postsynaptic neuron, and are

weakened when presynaptic neuronal firing follows firing in the postsynaptic neuron. However, in some circumstances STDP rules can vary, leading to coincident firing leading to either potentiation or depression, regardless of order of firing [119]. An unanswered question is how the network would be altered by state transitions with various STDP conditions, thus we tested the effects of NREM sleep with potentiation-only (see Figure III.S2 in the Appendix at the end of this thesis) and depression-only (see Figure III.S3 in the Appendix at the end of this thesis) STDP rules. For potentiation-only STDP the relationship between initial firing rate and firing rate change is reversed - with initially faster-firing neurons firing even faster after a period of NREM sleep. With a depression-only STDP rule, the relationship is similar to that presented in Figure III.5D**,** although all frequency changes are negative across NREM. As neither of these relationships is observed experimentally (Figure III.5D), this suggests that asymmetrical STDP rules alone can explain firing rate changes across NREM sleep in CA1.

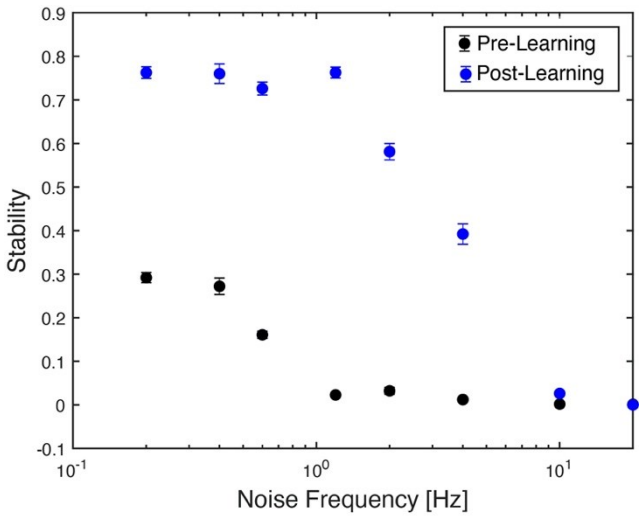

Figure III.7 STDP driven NREM-like memory consolidation results in an increased stability of the network dynamics across wide range of noise levels in the network.
Black dots – dynamics of the network prior STDP driven NREM-like memory consolidation. Blue dots - network dynamics post STDP driven NREM-like memory consolidation.

Finally, we set out to quantify effects of sleep-dependent consolidation. As mentioned before, the “memory” is represented by a configuration of input patterns (external to the network (I_{ext}, see Section 3.2) and/or internal ones driven by synaptic connectivity, which exemplify themselves via relative frequency of firing during wake-like dynamics, or relative phase relationships during NREM-like dynamics of the network. FuNS measures the robustness of the of the functional network connectivity which is exemplified via stability (over time) of the locking of the firing patterns between the neurons. Thus, sleep-dependent consolidation of the memory should result in an increased FuNS as compared to the unconsolidated dynamics. We investigated FuNS for consolidated and unconsolidated network dynamics for different frequency of noise fed into the network (Figure III.7). The stability of the consolidated (post-learning; Figure III.7 blue dots) dynamics is significantly higher than that of unconsolidated one (pre-learning; Figure III.7 black dots) except for the highest levels of noise when both cases are unstable.

3.4 Discussion

Sleep is vital for successful memory consolidation across organisms and different types of memories (e.g., those mediated by network activity in hippocampus vs. sensory cortex[207]). Similarly, recent experimental advances have shown that oscillatory dynamics in neural circuits–associated with sleep play a vital role in memory consolidation[191,192,208]. In the hippocampus, CFM consolidation relies on ad lib sleep in the hours immediately following CFC[110,209]. Consolidation of CFM is associated

with enhanced delta- (0.5–4 Hz), theta- (4–12Hz), and ripple-frequency (150–200 Hz) hippocampal network oscillations in the hours following learning [191].

Here, we observe that, during NREM sleep, representation coding undergoes functional remapping from a frequency-based coding of information predominant during wake (and particularly, during learning) to a timing-based representation predominant during sleep. Further, we argue that temporal organization of neuronal firing by network oscillations expressed during NREM sleep promotes feed-forward synaptic plasticity (i.e., STDP) from highly active neurons to less active ones. This process in turn promotes recruitment of additional neurons into the engram–the “systems consolidation” underlying long-term memory storage.

Our reduced model demonstrates that changing ACh level during wake and NREM sleep can play here a key role as it mediates changes in neuronal excitability, leading to highly heterogenous in frequency, asynchronous network-wide spiking during wake, and homogenized in frequency, temporally locked network-wide spiking during NREM sleep. Specifically, we show that the initial encoding of memories in a network (e.g. in the CA1 network during CFC) augments low frequency network oscillations (Figures III.1 and III.2). The augmentation of these oscillations occurs in a NREM sleep-like, low-ACh, type 2 network state. In this state, neurons are less responsive to input (i.e. the input-frequency curve flattens [128]), and they exhibit higher propensity to synchronize to periodic input (i.e., network oscillations). This locking to network oscillations leads to more stable firing relationships between neurons. This may occur via strengthening of excitatory-to-

excitatory connections in the network, or if they are not available via increased external input from other modalities (e.g. CA3 in hippocampus). We observe this increase in functional network stability (i.e. increase in FuNS) both in our hippocampal network model after introduction of either, a synaptically-encoded memory or via increasing external input (Figure III.2), and in the mouse hippocampus in vivo following single-trial CFC (Figure III.3).

Our previous and current data show that sleep-associated FuNS changes in CA1 following CFC is a salient feature of network-wide dynamics that accompanies successful memory consolidation (Figures III.3–III.6) [115,124,191,209]. We find that increased FuNS is associated with stronger low-frequency oscillatory patterning of the network, and predicts which experimental conditions will support, disrupt, or rescue fear memory consolidation (Figure III.3C). This increased stability, in turn, mediates mapping between firing rates during wake and relative phase-of-firing during NREM sleep (Figure III.4A and III.4B)–such that firing of neurons with higher baseline firing frequency leads those with lower baseline firing frequency. We showed that this frequency-vs. timing relationship is also detected in experimental data recorded from CA1 during NREM sleep (Figures III.4C, III.4E and III.4F). Moreover, when network oscillations are abolished by blocking inhibitory neuron activity (Figure III.5) the frequency/timing relationship is disrupted, indicating that oscillations do play central role in this process.

We hypothesize that this mechanism allows for recruitment of diversely firing populations of neurons (with their firing frequencies distributed over 3 orders of magnitude) into the

engram during sleep mediated memory consolidation, which is thought to be critical to the network operations underlying hippocampal function [123,210]. Homogenization of firing frequencies during sleep together with increased synchronization propensity and universal organization of the network bursts where intrinsically high firing frequency neurons lead the slow firing frequency ones, allows STDP-like mechanisms to recruit the low firing cells into the engram by linking them with the high frequency ones.

High-density electrophysiological recordings confirm that the most pronounced effect of sleep, and especially NREM sleep, on cortical firing rates is a narrowing of the firing rate distribution [123,204]. Other experimental findings found similar mean firing frequency dependent temporal ordering; Fernandez-Ruiz et al. [127] reported that the average rank order of a neuron's within-ripple sequence was negatively correlated with that neuron's baseline firing rate calculated from the entire sleep—wake session. More generally it was found that spiking during the NREM slow oscillation reveals an intrinsic temporal separation between high and low firing rate units, such that neurons with higher firing rates tend to spike before those with lower firing rates at the DOWN->UP transition [211].

Finally, when synaptic strength in the model is allowed to evolve through STDP, we observe this reorganization of firing rates across NREM sleep—with sparsely firing neurons increasing heir firing rate substantially, and highly active neurons decreasing their firing rate. These results are also observed in CA1 during sleep-dependent CFM consolidation (Figure III.6). We again observed a disruption of these effects when the oscillatory network activity is reduced via manipulations of interneurons. Similar sleep-

associated firing rate changes have been reported in neurons recorded from various neural circuits[123,124,182]. Moreover, this network reorganization results in increased network stability indicating increased robustness of the memory trace (Figure III.7) in terms of their temporal representation. This last result agrees with number experimental studies that found that neurons having widely different intrinsic firing frequencies act differentially within the activated engram and possibly play different coding roles. It was reported that such a activation sequence is composed of fast-firing subset of pyramidal neurons having low spatial specificity and limited activation change across sleep-experience-sleep cycle, and a slow-firing, highly plastic subset that elevated their association with ripples, and showed increased bursting and temporal coactivation during postexperience sleep [212,213]. Cognitively, these high activity principal cells were shown to form a core of each memory, with low activity cells joining as co-motives across the behavioral events [210].

Taken together, our results suggest a universal mesoscopic network mechanism underlying what is commonly referred to as systems memory consolidation. They also provide support for that while the brain may be biased towards firing rate based code during waking experience, the increased bias towards firing phase-based information coding in the context of network oscillations in sleep could play an instructive role for memory storage. This mechanism would mitigate the aforementioned limitations of rate based coding in the brain [114]. At the same time, it is clear that the two coding schemes are able to co-exist depending on the specific spatio-temporal attributes of the cognitive tasks.

We also note limitations of the presented model. Here specifically, we do not consider sequential activation of place cells as animal traverses through different locations in an environment. These would naturally impose sequential activation also in the waking activity pattern. We have however shown previously that such sequences can be also represented and stored during low ACh states [128].

Our model also does not take into account the emergence of theta band oscillation observed during REM sleep–a high ACh state. We hypothesize that the mechanism generating these oscillations is different, resembling higher frequency PING-like [214] mechanism, with these oscillations playing very different cognitive role. It was found experimentally that during REM, unlike NREM, the firing frequencies become even more heterogenous [182] which could be caused by increased steepness of the I-F curve.

This, being highly reduced, model does not take into account a number of known network, cellular and molecular pathways. Here we focus on highlighting only one possible role of changing ACh levels to explain experimental data in a highly generic network. Because of this the frequencies of slow oscillations obtained in NREM are generally higher than those observed experimentally [114]. We show in Figure III.S1 that the specific frequency of the slow oscillations can be manipulated by changing connectivity properties in the model. While this is a clear limitation, we don't believe that this shift in observed slow

oscillation frequencies bears effect on the results shown here.

Finally, ACh is not the exclusive player in terms of the changes in neuromodulation at the transitions between wake and NREM sleep [215]. Adenosine for example, can directly regulate ACh release via A1 receptors targeting cholinergic centers, but also regulate the potassium current via G-protein inwardly rectifying potassium (GIRK) channels augmenting the described cholinergic effect. Adenosine agonists are known to decrease wakefulness and increase sleep, tend to increase deeper stages of SWS, and increase slow wave activity or delta power. Conversely, adenosine receptor antagonists increase wakefulness and decrease sleep [216]. It was shown in in vitro conditions, that adenosine enhance slow oscillations of single neurons in the absence of other modulatory input [216,217]. Understanding more closely the interactions, and differential roles of the two mechanisms would be a focus of another study.

Although the present study is focused here on computational model results to predict data from the CA1 network during CFM consolidation and highlight the role ACh can play in this process, we believe that the mechanisms outlined here may be universally true. For example, sleep, and sleep-associated network oscillations, are required for consolidation of experience-dependent sensory plasticity in the visual cortex[115,192,218], and disruption of other hippocampal oscillations during sleep disrupts consolidation of other forms of memory [127]. Moreover, similar frequency-dependent changes in neuronal firing rates are also observed across periods of sleep in the visual cortex [124] and frontal cortex[123]. Based on these and other recent data linking network oscillations in sleep to

many forms of memory consolidation, this suggests a unifying principle for sleep effects on cognitive function, and one that could reconcile discrepant findings on how sleep affects synaptic strength [207]. It also provides an expanded and possibly alternative explanation of the role of sleep in memory management than what is often proposed [183]. Here we show that NREM sleep facilitates both increases and decreases in neuronal firing rates in the context of network reorganization, while at the same time recruiting heterogeneous neuronal populations during systems memory consolidation.

While the form of learning modeled here is not reliant on sequential neuronal activation during memory encoding, one possibility is that a similar mechanism may be associated with consolidation of memories for events during which neurons are sequentially activated [219–221]. Future studies will be needed to examine how temporal patterning of neuronal during post-learning NREM sleep relates to previously-studied “replay” of firing sequences reported in structures like the hippocampus during sleep following sequential spatial tasks. One possibility is that sequential replay presents a special case of NREM-dependent patterning of firing based on prior wake firing rates, as described here.

Chapter IV

Modeling Cortical Synaptic Effects of Anesthesia and Their Cholinergic Reversal

4.1 Introduction

General anesthetics work through a variety of molecular mechanisms while resulting in the common end point of sedation and loss of consciousness. Generally, the administration of common inhalation anesthetics induces decreases in synaptic excitation while promoting synaptic inhibition. Animal studies have shown that, during anesthesia, exogenously induced increases in acetylcholine-mediated effects in the brain can elicit wakeful-like behavior despite the continued presence of the anesthetic. Less investigated, however, is the question of whether the brain's electrophysiological activity is also restored to pre-anesthetic levels and quality by such interventions. Here we apply a computational model of a network composed of excitatory and inhibitory neurons to simulate the network effects of changes in synaptic inhibition and excitation due to anesthesia and its reversal by muscarinic receptor-mediated cholinergic effects. We use a differential evolution algorithm to fit model parameters to match measures of spiking activity, neuronal connectivity, and network dynamics recorded in the visual cortex of rodents during anesthesia with desflurane *in vivo*. We find that facilitating muscarinic receptor effects of acetylcholine on top of anesthetic-induced synaptic changes predicts

reversal of the neurons' spiking activity, functional connectivity, as well as pairwise and population interactions. Thus, our model results predict a possible neuronal mechanism for the induced reversal of the effects of anesthesia on post synaptic potentials, consistent with experimental behavioral observations.

I was the primary author on the article describing these results that was published in PLOS Computational Biology[222]. Experimental data was collected in previous work in the Hudetz Lab.

4.2 Methods

4.2.1 Experimental Data

Experimental results were based on the analysis of data collected in previous studies; for an in depth description refer to the original study [223]. Briefly, rats were surgically implanted with a multishank, 64 contact microelectrode array in the visual cortex (V1). After a post-surgery recovery period, they were placed in a cylindrical anesthesia chamber for administration of inhalation anesthetic. Desflurane was applied in the sequence of 8, 6, 4, 2, and 0% inhaled concentrations for 45 to 50 min at each level. Neural activity was recorded during the duration of the experiment and subsequently processed to extract multiunit spiking information. For this study, we analyzed unit spiking activity collected during the 0, 2, 4 and 6% desflurane exposure sessions and chose not to model 8% due to the confounding mechanism leading to the burst suppression phenomena normally present at this level of anesthesia[224,225].

4.2.2 Model Formation and Network Design

Neuron Modeling

The computational neuron model was based on the standard Hodgkin–Huxley modeling paradigm with parameters chosen to better account for the firing characteristics of cortical pyramidal neurons as established in previous studies [156,226,227]. In summary the neurons were modeled with coupled differential equations to account for nonlinear changes in voltage as a response to both tonic input and non-periodic input from connected neurons. A visual reference for the voltage response can be seen in Figure IV.1. For the remainder of the section a description of the model will be given for completeness including the parameters used in the model and structure of the governing equations.

Excitatory and inhibitory neurons are modeled using the Hodgkin-Huxley formalism [9] with parameters selected based on a model that emulated properties of both cortical pyramidal neurons and inhibitory interneurons [228,229]. The neuron model contained sodium, delayed rectifier potassium, slow M-Type potassium and leak currents as described in the following equations:

$$\frac{dV}{dt} = -g_{Na} m_{\infty}^{3} h(V - E_{Na}) - g_{Kd} n^{4}(V - E_{k})$$

$$-g_{Ks} z(V - E_{k}) - g_{L}(V - E_{L}) + I_{noise} - I_{syn} + I_{DC} \quad \text{(IV.1)}$$

$$\frac{dX}{dt} = \frac{X_{\infty}(V) - X}{\tau_{X}(V)} \; for \; x = \{h, n, z\} \quad \text{(IV.2)}$$

$$m_{\infty}(V) = \frac{1}{1 + e^{\left(\frac{-V-30}{9.5}\right)}} \quad \text{(IV.3)}$$

$$h_{\infty}(V) = \frac{1}{1 + e^{\left(\frac{V+53}{7.0}\right)}} \quad \text{(IV. 4)}$$

$$n_{\infty}(V) = \frac{1}{1 + e^{\left(-\frac{V+30}{10}\right)}} \quad \text{(IV. 5)}$$

$$z_{\infty}(V) = \frac{1}{1 + e^{\left(-\frac{V+39}{5.0}\right)}} \quad \text{(IV. 6)}$$

$$\tau_h(V) = 0.37 + \frac{2.78}{1 + e^{\left(\frac{V+40.5}{5.0}\right)}} \quad \text{(IV. 7)}$$

$$\tau_n(V) = 0.37 + \frac{1.85}{1 + e^{\left(\frac{V+27}{15}\right)}} \quad \text{(IV. 8)}$$

$$\tau_z(V) = 75 \quad \text{(IV. 9)}$$

In the above, *V* is the membrane voltage while *m, n, h* and *z* represent the unitless gating variables of the ionic current conductances. I_{syn} is the synaptic current input to the cell from other neurons in the network and has units of $\mu A/cm^2$. I_{noise} is a noise input consisting of randomly occurring brief current pulses with average frequency of 0.1 Hz, a duration of 2 ms and strength of 4 $\mu A/cm^2$. This noise input was sufficiently strong to generate an action potential in the absence of any other inputs. I_{DC} is a biasing constant current input of -0.77 $\mu A/cm^2$. E_{Na}, E_K and E_L are the reversal potentials for sodium, potassium, and leak currents, respectively, set to E_{Na} = 55 mV, E_K = −90 mV, E_L = −60 mV.

This neuron model, with the slow M-type K+ current, was developed to model the muscarinic-receptor effects of acetylcholine in cortical pyramidal neurons [158]. The

properties of this neuron model when g_{Ks} = 0 mS/cm^2 describe a neuron under high levels of acetylcholine while g_{Ks} = 1.5 mS/cm^2 represents a low acetylcholine state.

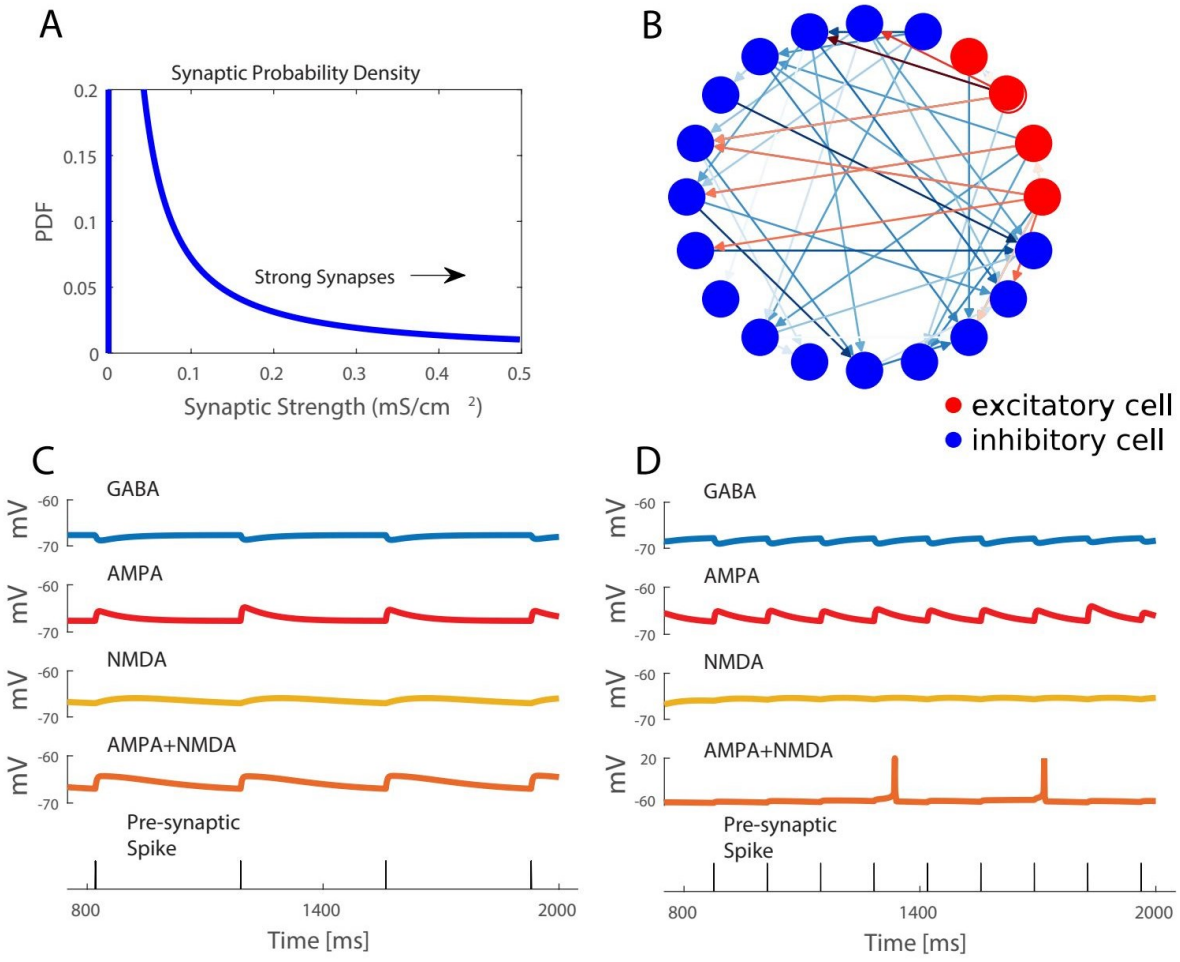

Figure IV.1 Network structure is populated by lognormal distributed random connection strengths
A) Synaptic strengths in model networks varied according to a lognormal distribution with a minority of connections being mediated by strong synaptic strengths, while weak synaptic strengths constitute majority of connections **B)** Simulated network consists of 200 inhibitory and 800 excitatory cells connected randomly with 10% probability. Connection color reflects the log of synaptic strength. **C, D)** Postsynaptic potential time courses in response to synaptic currents mediated by different receptors. Excitatory currents are modeled with both AMPA and NMDA mediated currents. Bottom panel shows timing of presynaptic spikes, for simplicity both inhibitory and excitatory presynaptic neurons are shown with the same spike times.

Network Design

We constructed E-I networks with 800 excitatory and 200 inhibitory neurons (Figure IV.1B). Neurons were connected randomly with 10% probability. Synaptic strengths followed a log normal distribution, as suggested to occur in cortical networks (Figure IV.1A) [230] .The distribution was defined by parameters $\mu = -20.0, \theta = 9.4,$ and characterized by the equation:

$$PDF_{Log}(X) = \frac{1}{x\theta\sqrt{2\pi}}\left(e^{-\frac{(\ln x - u)^2}{2\theta^2}}\right) \quad \text{(IV. 10)}$$

μ and θ are defined such that they are the mean and standard deviation of the logarithm of x if the logarithm of x was normally distributed. This connectivity distribution was chosen such that ~0.2% of excitatory connections would elicit an action potential in a post-synaptic cell in the absence of other inputs for our parameter values representing the wake state. The value of 0.2% was determined by experimental data in which cross correlogram analysis showed a 0.2% "strong" connection probability among a local population of neurons [139].

Synaptic currents mediated by AMPA, NMDA and $GABA_A$ receptors were included in the network such that excitatory synaptic currents were given by $I_{exc} = I_{AMPA} + I_{NMDA}$ and inhibitory synaptic currents by $I_{inh} = I_{GABA}$. All synaptic currents were modeled with a double exponential function of the form

$$I_X = P_x\, B_x\, V_{0.5}\, g_{\log} \left(e^{-\frac{t-t_{spike}}{\tau_{Xs}}} - e^{-\frac{t-t_{spike}}{\tau_{Xf}}} \right) (V - E_{\mathrm{x}}) \qquad (\mathrm{IV}.11)$$

where X indicates the receptor type (AMPA, NMDA or $GABA_A$), t_{spike} is the time of the presynaptic spike and g_{log} is the synaptic conductance drawn from the lognormal distribution.

Reversal potential E_x was set at −75 mV for inhibitory synapses and 0 mV for excitatory synapses. The term g_o will be used to refer to $B_x\, V_{0.5}\, g_{\log}$ .Time constants τ_{Xs} and τ_{Xf} governed the fast rise and slow decay of the synaptic current and were set as follows:

$$t_{\mathrm{AMPAf}} = t_{\mathrm{NMDAf}} = t_{\mathrm{GABA_Af}} = 0.2\ ms \qquad (\mathrm{IV}.12)$$

$$t_{\mathrm{AMPAs}} = 3.0\ ms\ , t_{\mathrm{NMDAs}} = \ 200.0\ ms,\ \ t_{\mathrm{GABA_As}} = 5.5\ ms \qquad (\mathrm{IV}.13)$$

The NMDA synaptic conductance was additionally gated by the post-synaptic voltage [231,232] described by the additional pre-factor B_x:

$$B_{\mathrm{AMPA}} = B_{\mathrm{GABA_A}} = 1 \qquad (\mathrm{IV}.14)$$

$$B_{\mathrm{NMDA}}(V) = \frac{1}{1 + e^{-\frac{V+10}{3.57}}} \qquad (\mathrm{IV}.15)$$

Fig IV.1C, D illustrates time courses of the synaptic currents. Additionally, to account for event-to-event variability, a variability pre-factor $V_{0.5}$, randomly chosen uniformly from [0.5, 1], modulated the synaptic current induced by each pre-synaptic spike. Finally, the scaling factors P_{x} simulated anesthetic effects on synaptic conductances. Values of P_{x} for each receptor type were optimized to fit multiple measures of network dynamics for each

level of anesthesia. Values are listed in Tables IV.1 and IV.2 that show average parameter values for optimizations performed on ten different network realizations, and the specific parameter values used for the presented analysis of results, respectively.

4.2.3 Measures and Metrics

We used several different measures to quantify the changes between network states and dynamics under different levels of anesthesia observed in the experimental data and simulated in the neural network models.

Integration and Complexity

We computed the information theoretic measures Complexity C(X) and Integration I(X) to quantify changes in the entropy of the network [233]. I(X) is a generalization of mutual information that measures the amount of total entropy of a system that is accounted for by the interactions among its elements. I(X) is zero when system elements are statistically independent [233]. C(X) measures the total entropy loss due to interaction of system elements, or, equivalently, the difference between the sum of the entropies of the individual elements and the entropy of the entire system. C(X) is low for systems with independent elements or with highly synchronous elements.

To compute these measures, the total spiking activity from an experimental recording or a network simulation was partitioned into patterns by binning spike trains into 1 ms time bins and constructing vectors for each time bin containing a 1 at the neuron index if the

neuron spiked within that time bin and a 0 if there was no spike (columns in Figure IV.2). The set X of unique vectors, representing patterns of spiking activity within a bin, that occurred across the data set were identified. Additionally, discretized spike vectors $X_i, i = 1, \dots, N$, were constructed for each cell (rows in Figure IV.2).

To compute integration and complexity only a subset of neurons were considered. 60 neurons were selected at random from both the experimental data and the simulation. I(X) and C(X) were computed by taking 3 random intervals of 6s, computing the measure on each set of intervals, and then averaging the measure outcomes across the three sets.

Integration was computed as

$$I(X) = \sum_{i=1}^{N} H(X_i) - H(X) \qquad \text{(IV.16)}$$

where $H(X_i) = -\sum_k p_k log p_k$ is the entropy based on the probability of a spike occurring in the i^{th} cell, and $H(X) = -\sum_j p_j log p_j$ is the entropy based on the probability of occurrence of a spike pattern vector.

Complexity was computed as

$$C(X) = H(X) - \sum_{i=1}^{N} H(X_i | X - X_i) \qquad \text{(IV.17)}$$

Here, $H(X_i)$ is the entropy of the spike train belonging to neuron i while $H(X)$ is the entropy of the set of spike vector for the entire interval. $H(X_i|X - X_i)$ is the conditional entropy where X_i is the new spike vectors neglecting the ith unit and is conditioned on the spike train of the ith unit. The metric is discussed greater detail in original study [233].

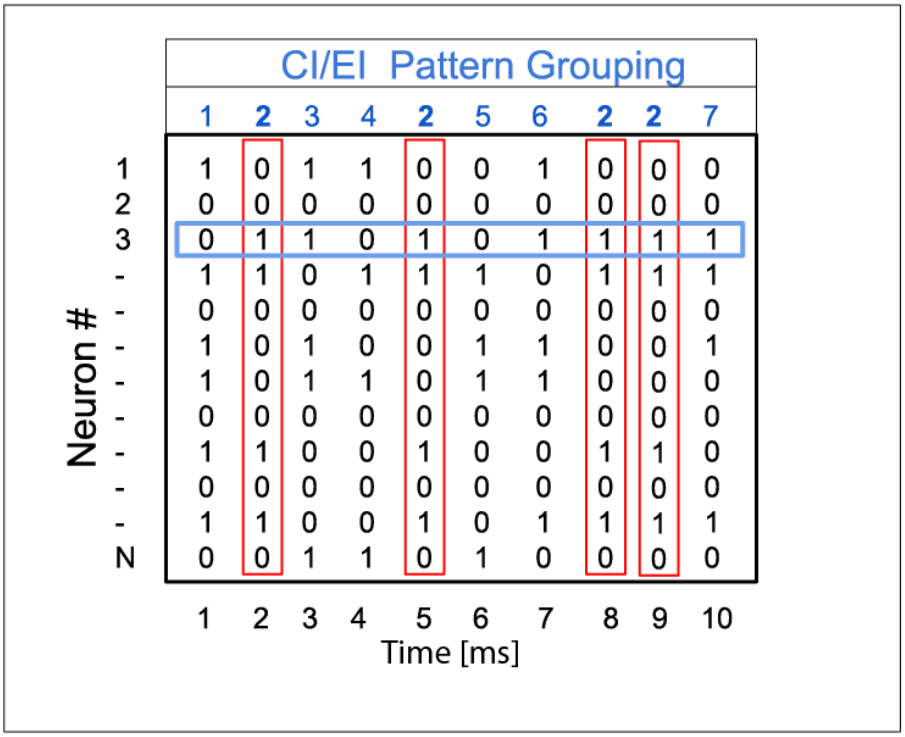

Figure IV.2 Binned spike patterns for complexity and integration measures.
To compute entropy metrics complexity (C(X)) and integration (I(X)), spike trains were binned in 1 ms bins. H(X) in equation (16)/(17) is computed according to unique patterns associated with column vectors (red vectors) while $H(X_i)$ is the entropy associated with a single neuron spike train (blue vector).

Mean Phase Coherence

We computed mean phase coherence to quantify the average phase relation between spike times of pairs of neurons in experimental recordings and network simulation. The pairwise mean phase coherence is given by

$$\sigma_{i,j} = \left| \frac{1}{N} \sum_{k=1}^{n} \left(\exp\left(i2\pi \frac{t_{j,k} - t_{i,k}}{t_{i,k+1} - t_{i,k}} \right) \right) \right| \qquad (\text{IV}.18)$$

where $t_{j,k}$ is the time of the k^{th} spike of the j^{th} neuron and $t_{i,k}, t_{i+1,k}$ are times of successive spikes of the i^{th} neuron. Network mean phase coherence is the average of $\sigma_{i,j}$ over all pairs of neurons.

For two neurons i and j, the mean phase coherence is 1 when the spike times of neuron j always occur at the same relative phase in the cycle defined by two subsequent spikes of neuron i. Conversely, pairwise mean phase coherence is zero when spikes of neuron j occur at random phases of the neuron i spike cycle for the entire set of neurons i spike times, due to averaging of phases.

Functional Connectivity Probability and Strength

Functional connectivity probability and strength were determined through cross correlogram analysis on spike trains [234] between pairs of neurons with minimum average spike rate of 1 Hz. Since experimental recordings contained on average ~60 eligible units, these measures for the simulated networks were computed based on spike trains of 60 eligible neurons. For each pair of cells, spike trains were segmented into 40 ms intervals centered on each spike of the designated “reference” cell of the pair and discretized into 1.3 ms bins. Cross-correlations of discretized segments between the “reference” and “comparison” cell for every “reference” cell spike were summed to form cross correlograms (Figure IV.3).

Significance of correlations was determined by comparison to a constructed “jittered” dataset. The jittered data set was formed by randomly “jittering” spike times of the “comparison” cell by [–5, 5] ms and then computing the cross correlogram. This was repeated 100 times for the jittered data set. The global confidence band for excitatory (inhibitory) connectivity was computed by taking the 97% confidence interval associated with the global peak (trough) of the jittered data set. A significant connection was determined when the standardized peak (trough) of the original cross correlogram was greater (less) than 2 times the 97% confidence interval when measured from the mean (blue/red) [139,234,235]. The standardized peak was formed by dividing the peak amplitude by jittered mean and standard deviations of the cross correlogram.

Excitatory connectivity strength was determined by taking the difference in the peak height within 0 and 5.2 ms (first four bins) and the jittered mean and dividing it by the

jittered standard deviation. The inhibitory strength was computed in a similar manner by looking at the trough of the cross correlogram within 0 and 5.2 ms.

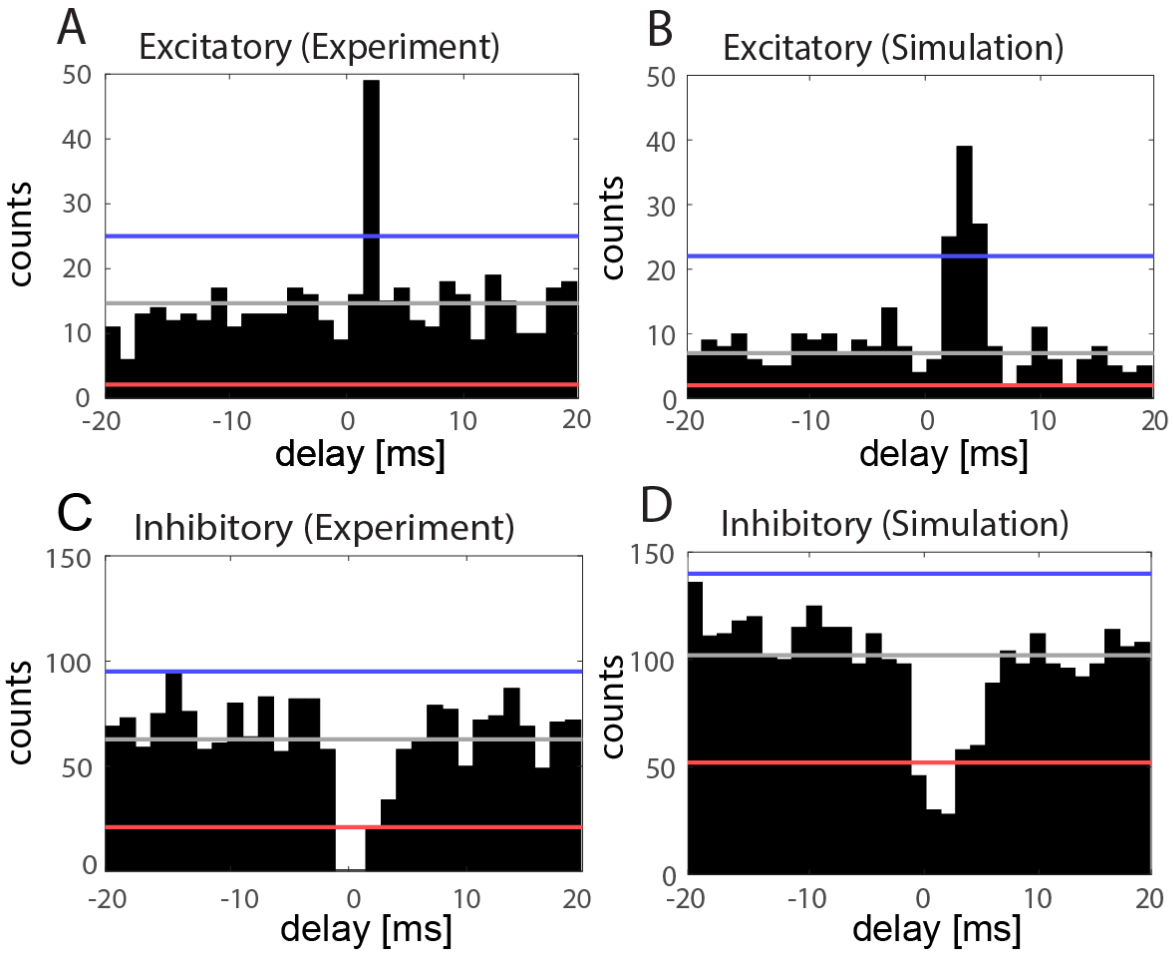

Figure IV.3 Cross Correlogram computes coincident spike relations by summing relative spike times of reference and comparison neurons.

A-D) Cross correlograms between example pairs of "reference" and "comparison" cells, centered at spike times of the "reference" cell, from the experimental recordings (left column) and simulated networks (right column). Significance bands were computed from a jittered data set of "comparison" cell spike times (gray line = mean of jittered data set, red line = excitatory significance, blue line = inhibitory significance, see text). **A-B)** Example cross correlograms showing significant excitatory connections between cell pairs. **C, D)** Example cross correlograms showing significant inhibitory connections between cell pairs.

Excitatory connectivity strength was determined by taking the difference in the peak height withing 0 and 5.2 ms (first four bins) and the jittered mean and dividing it by the jittered standard deviation. The inhibitory strength was computed in a similar manner by looking at the trough of the cross correlogram within 0 and 5.2 ms.

4.2.4 Parameter Optimization

Network model parameters were optimized using an evolutionary algorithm to fit measures of network frequency, mean phase coherence, integration and complexity computed from the experimental unit spiking data collected during the 0%, 2%,4% and 6% desflurane exposure sessions. The optimized parameters were the synaptic conductance scaling parameters $P_{AMPA}, P_{NMDA}, P_{GABA}$ (A series) and, additionally to those, the maximal conductance of the M-type K+ current g_{Ks} (B series). The algorithm is similar to typical differential evolution procedures[236,237]. Briefly, from a population of 30 agents (parameter sets), at each generation the 10 agents with highest cost function values were replaced with 10 new parameter sets constructed by an evolutionary algorithm described below (Figure IV.4A). The stopping criteria was 100 generations without change in the lowest cost function (*L(X)*) value across the population of 30 agents. The stopping criteria was chosen as it supports a finite run time in stochastic search and has been used in similar implementations[238,239].

The initial population of 30 parameter sets representing the 0% anesthetic state was chosen from the 256 parameter sets generated by assigning parameter values from the following sets: $P_{AMPA}, P_{NMDA} \in \{0.5, 1.0, 1.5, 2.0\}$, $P_{GABA} \in \{2.5, 5.0, 7.5, 10.5\}$ and $g_{Ks} \in \{0.3, 0.7, 1.1, 1.5\}\, mS/cm^2$. We initially searched for boundary parameters that achieved

balanced network dynamics and followed this by the above parameter scan within those bounds. The parameter scan was then followed by our algorithmic fitting procedure. Model networks with fixed connectivity structure and synaptic strength g_0 values were simulated with each parameter set for 20 s and frequency, mean phase coherence, integration, and complexity measures were computed based on spiking activity excluding the initial 1s, to avoid initial transients . The cost or loss function, $L(X)$, based on these measures, $x =$ frequency, MPC, I(X) and C(X), compared values computed from simulations, x_{sim}, and experimental data, x_{exp}, at 0% anesthetic state as follows:

$$L(X) = \sum_x m_x,$$
$$m_x = \left(\frac{x_{exp} - x_{sim}}{x_{exp}}\right)^2 \qquad \text{(IV. 19)}$$

Here, the 20 lowest cost parameter sets were kept and each parameter value was randomly varied uniformly by 10% of its value to avoid duplicate values. The final 10 parameter sets were then constructed using the differential evolution algorithm.

Similar to typical differential evolution procedures [236,237] we set a cross over probability CR = 0.8 and a differential weight DW that was randomly varied between [0,2]. From the subpopulation of 20 parameter sets, 10 randomly chosen sets, a^k $(k = 1, \dots, 10)$, formed the basis for 10 newly created sets, e^k $(k = 1, \dots, 10)$. For each set a^k, 3 different sets b^k, c^k and d^k were chosen that were different from a^k and each other. Then, for each element $i = 1, \dots, 4$ in the set, a random number ρ_i from the uniform distribution [0,1] was chosen. If ρ_i was less than CR, a new parameter value e_i^k was generated as $e_i^k = b_i^k + DW\left(c_i^k - d_i^k\right)$; otherwise $e_i^k = a_i^k$.

This was done for each element in the new agent and was repeated until 10 new agents were created. After this was done the 10 new agents were simulated and then the 30 total parameters were evaluated for their cost. The 10 with the highest cost (worse fit) were then rejected and the process was repeated.

We performed 2 parameter optimizations, A-Series and B-Series, to parse out potentially different effects of anesthetic modulation on synaptic conductances only (A series) and of combined modulation on synaptic conductances and cholinergic effects (B series) (Figure IV.4 B,C). In both scenarios, populations A1/B1 were the result of optimizing $P_{AMPA}, P_{NMDA}, P_{GABA}, g_{Ks}$ to the experimental 0% anesthetic case. In the A-series, P_{NMDA}, P_{GABA} were optimized while in the B-series, $P_{NMDA}, P_{GABA}, g_{Ks}$ were optimized to the 2%, 4% and 6% anesthetic cases. Optimizations for the 6% anesthetic case, A4/B4, were initiated from parameter values constrained by experimental reports of 20% average decrease in NMDA-mediated synaptic signaling and 40% increase in GABA-ergic synaptic signaling under desflurane [155,240]. These initial values were randomly varied uniformly by +/- 5% to generate variability in the event of parameter convergence. In the optimizations for the 2% and 4% anesthetic cases, A2/B2 and A3/B3, respectively, the initial population for A2/B2 was A1/B1, and the initial population for A3/B3 was A4/B4.

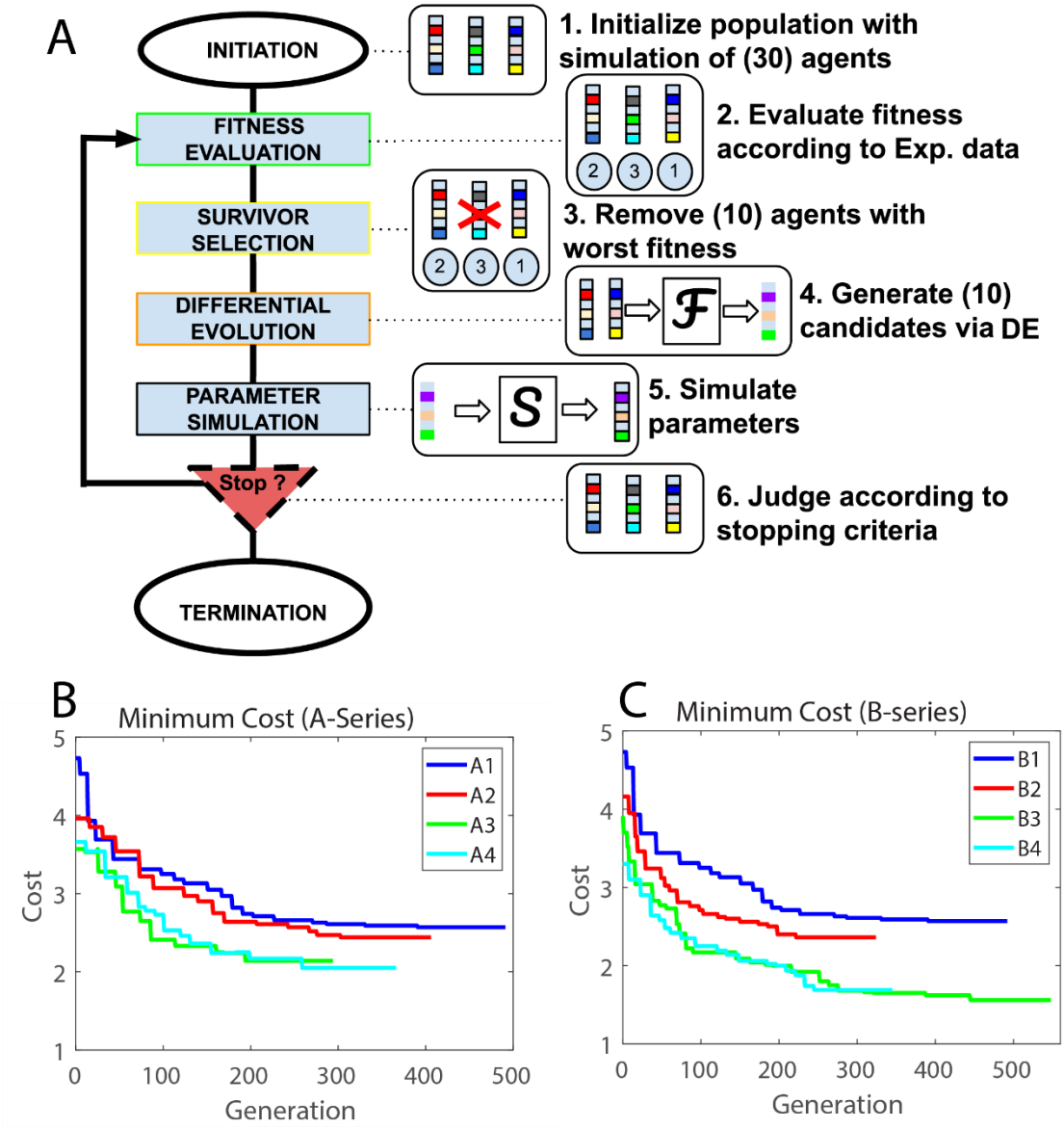

Figure IV.4 Parameter search fine-tuned through Differential Evolution algorithm
A) Evolutionary algorithm procedure, differential evolution, was used to optimize model parameters. For each generation, 10 agents (parameter sets) with the highest cost function from the population of 30, were chosen for replacement. Algorithm was repeated until stopping criteria of 100 generations without change in lowest cost function value across the population was met. **B,C)** Lowest cost function values across the parameter set populations at each generation for the A-series (B) and B-series (C) parameter optimizations. Population A1/B1, A2/B2, A3/B3 and A4/B4 were optimized to experimental data from the 0%, 2% ,4% and 6% anesthetic cases, respectively. The optimizations for A1 and B1 were identical. In the A-series (A2-A4), P_{NDMA}, P_{GABA}, were optimized and in the B-Series (B2-B4), P_{NDMA}, P_{GABA}, g_{Ks} were varied.

.

Simulation of ACh Reversal

To validate robustness of the parameter optimization, we ran our optimization for 10 network realizations, keeping the network structure fixed for all anesthetic levels. The average and error (SEM) for the optimized parameters across these 10 networks is shown in Table IV.1. Table IV.2 lists the parameter values with the lowest cost function for one of these optimization runs that we used in our model analysis.Simulated cholinergic reversal (AR1-AR4/BR1-BR4) was modeled by decreasing the value of g_{Ks} from the values in A4/B4 to 0.4 mS/cm^2 such that there were 4 values in the reversal series.

Statisical Analysis

The effects of desflurane and ACh-modulated M-current were tested using RM-ANOVA with the level of intervention as fixed factor on each of the metric for both experimental data and the simulation results. When the effect of the treatment was significant, the individual effects were further examined using individual paired t-tests with Bonferroni correction at $\alpha = 0.0167$ for testing the anesthesia effect (four levels) and $\alpha = 0.0125$ for testing the reversal effect (five levels). To compare trends, additional tests with linear regression were done on the expermental data as well as the A-series/B-series and the cholinergic reversal results, at $\alpha= 0.05$. Statistical analyses were conducted in Excel.

Functional Connectivity Analysis

Functional connectivity was determined via cross-correlogram analysis where the connectivity strength (significance) was determined by comparing the peak within 0 to 5 ms lag of the cross-correlogram to the jittered mean and standard deviation of the cross correlogram. Mean was formed from mean of 100 jittered correlograms and the standard deviation from the jittered means [234,235]. The connectivity strength was recorded for each pair wise connection and then used to determine the cosine similarity between the two simulations by computing the dot product of the pairwise connectivity strengths for different anesthesia levels. This was converted to a Z-Score by comparing average cosine similarity between two anesthesia levels (10 network average) to the cosine similarity between two anesthesia levels created in the same manner from jittered time-series (jittered time lag peak compared to jittered mean and standard deviation).

	P_{NMDA}	P_{GABA}	P_{AMPA}	g_{Ks}		P_{NMDA}	P_{GABA}	P_{AMPA}	g_{Ks}
A-Series (±SEM)					B−Series(±SEM)				
A1	**1.69**±0.05	**3.92**±0.51	**1.27**±0.07	**0.98**±0.08	B1	**1.69** ± .0.05	**3.92** ± .0.51	**1.27** ± .0.07	**0.98** ± .0.08
A2	**1.41**±0.03	**4.32**±0.44	**1.27** -	**0.98** -	B2	**1.63** ± .0.07	**5.51** ± .0.33	**1.27**−	**1.07** ± 0.03
A3	**1.22**±0.12	**8.13**±1.21	**1.27** -	**0.98** -	B3	**1.47** ± .0.06	**6.35** ± .0.94	**1.27**−	**1.23** ± 0.02
A4	**1.09**±0.09	**10.61**±1.91	**1.27** -	**0.98** -	B4	**1.36** ± .0.09	**8.17** ± .1.41	**1.27**−	**1.17** ± 0.06

Table IV.1 Parameter optimization for simulated anesthetic concentrations when performed on 10 different network realizations.

A/B-series describe optimal values determined by the differential evolution algorithm fitting network connectivity parameters obtained when repeating the optimization for 10 total networks. Optimization includes A-Series, when ACh effects are assumed constant and B-Series, when ACh effects are allowed to change with anesthetic concentration. The scaling factors P_x scale the effects of synaptic conductances mediated by the x receptor (x = NMDA, GABA and AMPA). A1-A4/B1-B4 denote optimal parameter sets fit to experimental recordings at varying anesthetic concentrations (0%, 2%, 4%, 6% desflurane, respectively). P_{AMPA} is only fit for the 0% anesthetic case A1/B1. Error displayed is SEM.

	P_{NMDA}	P_{GABA}	P_{AMPA}	g_{Ks}		P_{NMDA}	P_{GABA}	P_{AMPA}	g_{Ks}
A-Series					B−Series				
A1	**1.64**	**3.98**	**1.22**	**0.97**	B1	1.64	3.98	1.22	0.97
A2	**1.43**	**4.61**	**1.22**	**0.97**	B2	1.57	5.12	1.22	1.10
A3	**1.12**	**8.51**	**1.22**	**0.97**	B3	1.42	6.02	1.22	1.24
A4	**1.07**	**9.41**	**1.22**	**0.97**	B4	1.27	8.13	1.22	1.18
A-Series Reversal					B−Series Reversal				
AR1	**1.07**	**9.41**	**1.22**	**0.81**	BR1	1.27	8.13	1.22	0.98
AR2	**1.07**	**9.41**	**1.22**	**0.67**	BR2	1.27	8.13	1.22	0.79
AR3	**1.07**	**9.41**	**1.22**	**0.53**	BR3	1.27	8.13	1.22	0.60
AR4	**1.07**	**9.41**	**1.22**	**0.40**	BR4	1.27	8.13	1.22	0.40

Table IV.2 Parameter values for simulated anesthetic concentrations and cholinergic reversal results.

Parameters from initial fit used to simulate anesthetic effects and cholinergic reversal. A/B-series describe optimal values of initial fit determined by the differential evolution algorithm for network connectivity parameters obtained when ACh effects are assumed constant (i.e., g_{Ks} is constant; A-Series) and when ACh effects are allowed to change with anesthetic concentration (B-Series). P_x denotes scaled changes in synaptic conductance's mediated by the x receptor (x = NMDA, GABA and AMPA) as described in Table 1. A/B-Series Reversal (AR/BR series) represent simulated anesthetic reversal, obtained by increasing ACh effects (decreasing g_{Ks} from A4/B4 levels) while keeping all other parameters constant.

4.2.5 Simulations

Custom C++ code was developed for numerical simulations which was run on the Great Lakes High Performance Cluster. For the evolutionary algorithm each model simulation was run for 20s. The stopping criteria was met when the lowest minimum cost remained unchanged for 100 generations. To check the robustness of the current parameter set, 10 additional generations were run with model simulations of 80s and an increased crossover probability (CR=0.9). We detected no change in the minimum cost parameter set. For the results shown in Figures IV.5-7 each simulation was simulated for 150000 ms or 150 s. The length of this runtime was necessary to result in enough spike times to calculate metrics based on cross correlograms. Results in Figures IV.7 and IV.8 are for 10 simulation runs in which network connectivity was randomized across runs but maintained for the different simulated anesthetic levels. In this way, each of the 10 simulation runs corresponds to a unique simulated experiment. On each run the voltage and gating variables were subject to random initial conditions independent of the network seed. On initialization V was uniformly varied between [-72,-32] mV, n between [0.2,0.6], z between [0.2,0.3] and h between [0.2, 0.6] while m was initialized at 0 for all runs. The equations were integrated using the 4^{th} order Runge Kutta method.

4.3 Results

4.3.1 Modeling Anesthetic Induced Synaptic Changes via Genetic Algorithm Parameter Search

We constructed a reduced, biophysical, neuron network model to investigate how synaptic-level changes, mediated by the anesthetic desflurane, affect network-level

dynamics compared to data measured in the visual cortex *in vivo*, and, separately, howcholinergic neuromodulatory changes at the cellular level may reverse these anesthetic effects. The network consisted of excitatory and inhibitory neurons interacting via synapses mediated by excitatory AMPA and NMDA receptors and inhibitory $GABA_A$ receptors (see section 4.2; FigureIV.1). Acetylcholine (ACh) neuromodulation of the excitability of excitatory cells was simulated as amus-carinic receptor-mediated variation in the conductance of the slow, hyperpolarizing current.

We used an evolutionary algorithm (see section 4.2, Figure IV.4) to identify optimal synaptic connectivity parameter sets (Table IV.1/Table IV.2) that most closely match multiple quantitative measures of network activity recorded under different desflurane concentrations. This allowed us to objectively find two sets of parameter modifications that fit model results to the experimental data. Namely, in one set of optimized parameters, we allowed the algorithm to optimize the inhibitory $GABA_A$ connectivity strength and excitatory NMDA connectivity strength while keeping AMPA connectivity strength constant as simulated anesthetic concentration was increased (Table IV.1/Table IV.2, A-Series). In the second set, in addition to varying the above parameters, we allowed cholinergic effects to vary with simulated anesthetic concentration (Table IV.1/Table IV.2, B-Series). The optimization cost function was based on fitting measures of network frequency, mean phase coherence, and information theoretic measures of integration and complexity, and the parameter sets were validated using measures of synaptic connection probability and strength, as well as network functional connectivity (see section 4.2, Figure IV.10). Optimizations were conducted separately for each anesthetic

level, i.e., parameter values A1/B1 were optimized to data recorded for 0% desflurane concentration, A2/B2 for 2% desflurane, A3/B3 for 4% desflurane and A4/B4 for 6% desflurane.

In each optimization run we kept the network structure fixed. Particularly, when optimizing across the A-series/B-series we maintained a single network to guarantee that the cost or loss function monotonically decreased across generations. To check for robustness, we optimized parameters for 10 independent network realizations. For each network optimization, the initial pool of parameters seeding the search was kept the same. Table IV.1 reports mean and standard error of obtained parameter values of the 10 optimization runs. Table IV.2, on the other hand, represents the best fit optimized parameter set that was subsequently used to identify anesthetic effects on the dynamics of the network.

With synaptic connectivity parameters fixed at their levels corresponding to 6% desflurane concentration, we then simulated the reversal of the anesthetic effects by increasing AÇh effects as mediated by the muscarinic receptor dependent M-type K+ current (specifically, decreasing its conductance g_{Ks}; Table IV.2, AR/BR-Series).

The synaptic connectivity parameter values determined by the evolutionary algorithm mirrored experimentally identified effects of desflurane on excitatory and inhibitory synaptic currents [139,155,241](See section 4.2, Figure IV.4). Specifically, in the A-series parameters, there was a decrease in the effects of NMDA receptor-mediated current while there was an increase in the effect of GABA-mediated current in response to increases

in anesthesia (Tables IV.1/Table IV.2). A similar trend was obtained in the B-Series with the added result that decreasing effects of acetylcholine (increasing g_{Ks}) correlated to the effects of increased anesthesia except for the change from B3 to B4. Interestingly, the optimization predicted that, in the B-Series, to offset the decrease in neuronal excitability due to decreasing ACh level (i.e., increased g_{Ks}) with anesthetic concentration, the increase in $GABA_A$ synaptic efficacy was smaller than that obtained in the A-Series, and similarly, the NMDA synaptic efficacy was systematically higher as compared to the A-Series.

Figure IV.5 shows example raster plots comparing experimental spike timing data collected under the varying desflurane concentrations with model results for the optimized A- and B-Series parameter sets, as well as the simulated ACh-induced reversal of anesthetic effects. The model raster plots show similar qualitative trends for increasing simulated anesthetic concentration as the experimental data, specifically spiking patterns change from asynchronous with higher spiking frequencies at simulated 0% desflurane concentration (A1/B1) to a lower frequency, more synchronized firing pattern for simulated 6% desflurane concentration (A4/B4). Furthermore, the simulated ACh reversal (AR1/BR1 – AR4/BR4) reverses those trends.

In the following sections, we analyze how specific characteristics and measures of network dynamics, including frequency distributions and profiles, mean phase coherence, information theoretic measures, and excitatory/inhibitory connectivity probability, computed for the experimental data for progressively increased desflurane levels are

reproduced in the optimized model networks. These measures were then computed for simulated increasing levels of cholinergic modulation to analyze the recovery of network dynamics during ACh-induced reversal of anesthetic effects.

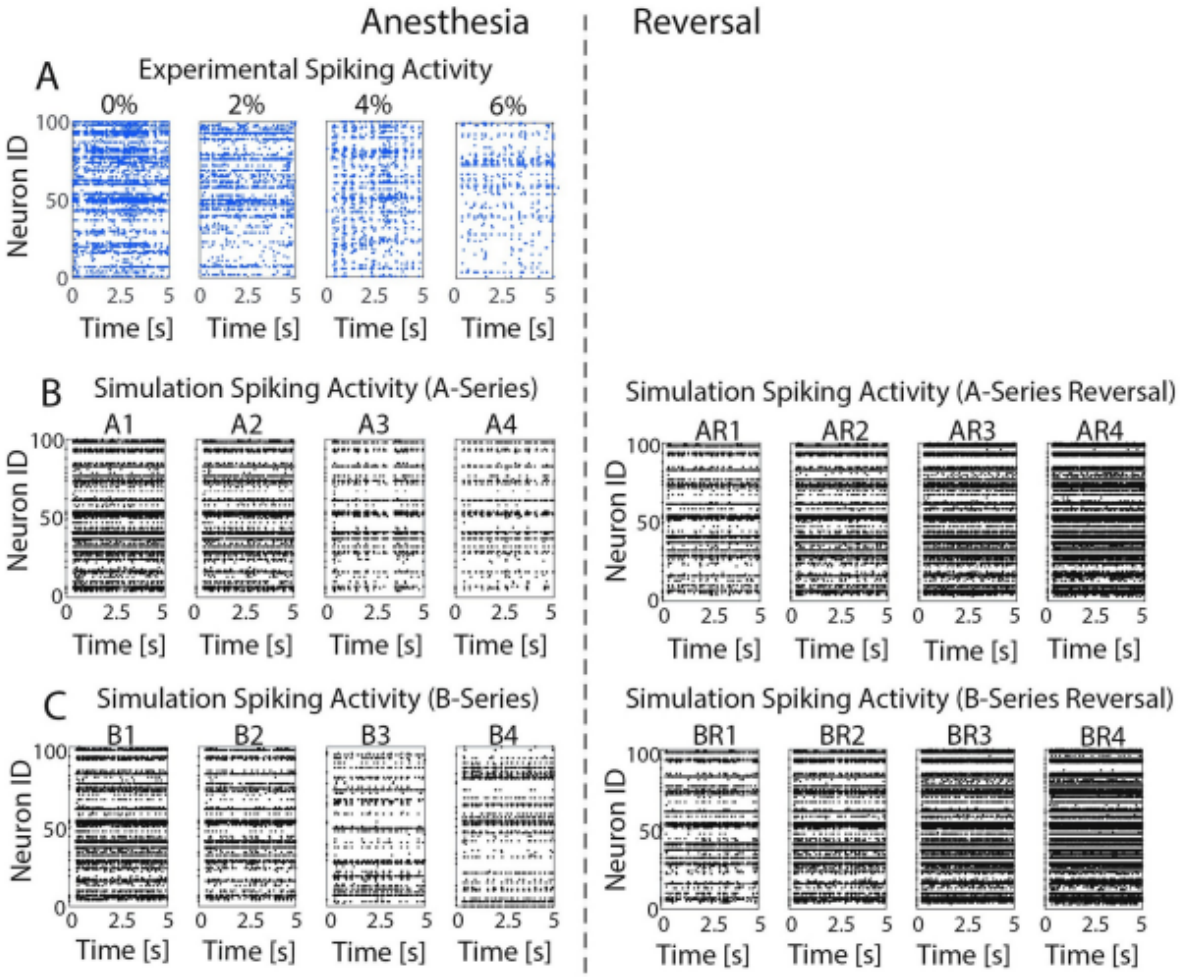

Figure IV.5 Changes in anesthesia level lead to transitions from high frequency asynchronous to low frequency synchronous spiking patterns

A) Raster plots of experimentally recorded neuronal activity in response to changes in desflurane levels. For higher concentrations of desflurane (**6%**), oscillatory synchronous network activity can be seen in spiking dynamics. For lower levels of anesthetic, oscillations are not apparent and asynchronous activity dominates. **B)** Raster plots for simulated anesthetic effects in optimized model networks for constant g_{Ks} (A series) and the simulated ACh-induced reversal of anesthetic effects (A series reversal). **C)** Raster plots for simulated anesthetic effects in optimized networks with changing g_{Ks} (B-series) and its reversal (B series reversal). In both B) and C), simulated anesthetic reversal shows reinstatement of asynchronous from synchronous spiking patterns. Simulation results based on best fit parameters (lowest cost optimization when averaged across anesthesia levels).

4.3.2 Anesthetic Effects on Network Dynamics and their Predicted ACh-Induced Reversal

Spike Frequency Decreases in Response to Anesthesia and Recovers in Response to Decreased M-Current.

We first characterized the changes in the mean neuronal spike frequency as well as the shape of the neuronal spike frequency distributions as a function of anesthetic level in the optimized model networks (Figure IV.6 and Figure IV.7A). We observed that the neurons generally fired less, in both experimental data and the simulations, as a function of anesthetic concentration. Also, the spread of neuronal firing frequencies decreased significantly with increased anesthetic level, with the loss of the right skew observed in the wake cases (0%, A1 and B1). Spike frequency decreased as a function of desflurane levels for both parameter series, (A and B series, without and with ACh changes, respectively), with a similar frequency drop, irrespective of the implemented ACh changes that affect neuronal excitability in the B series. In predicted ACh-induced reversal, the rightward skew in frequency distributions was recovered, and the B series showed stronger recovery in mean spike frequency as compared to the A series. This is because, as mentioned above, accounting for cholinergic changes on neuronal excitability under desflurane anesthesia predicts that synaptic changes are less severe. Namely, in the B series, $GABA_A$ synaptic strength was not as high, and NMDA synaptic was not as low compared to the A series.In the experimental data, anesthesia reduced excitatory firing frequency in a dose dependent manner ($p<0.05$, correlation test). This was likewise observed in both A- and B-series simulations ($r_E = -0.97$, $r_A = 0.-95$,$r_B=-0.99$, $P_E <0.0001$,

P_A <0.0001, P_B<0.0001). Moreover, firing frequency in the awake state showed a significant difference between all subsequent anesthesia states (p<0.0167,Bonfer- roni) for the experiment as well as for the A- and B-series. Likewise, when comparing firing rates in all of the subsequent reversal states to the highest anesthesia state (e.g. A4 to AR1-AR4) a significant difference was found (p<0.0125, Bonferroni). As anticipated, the reversal simulation had positive firing rate correlations for both A- and B- series (r_{AR}=0.89,r_{BR} = 0.93, P_{AR} <0.0001, P_{BR}<0.0001).

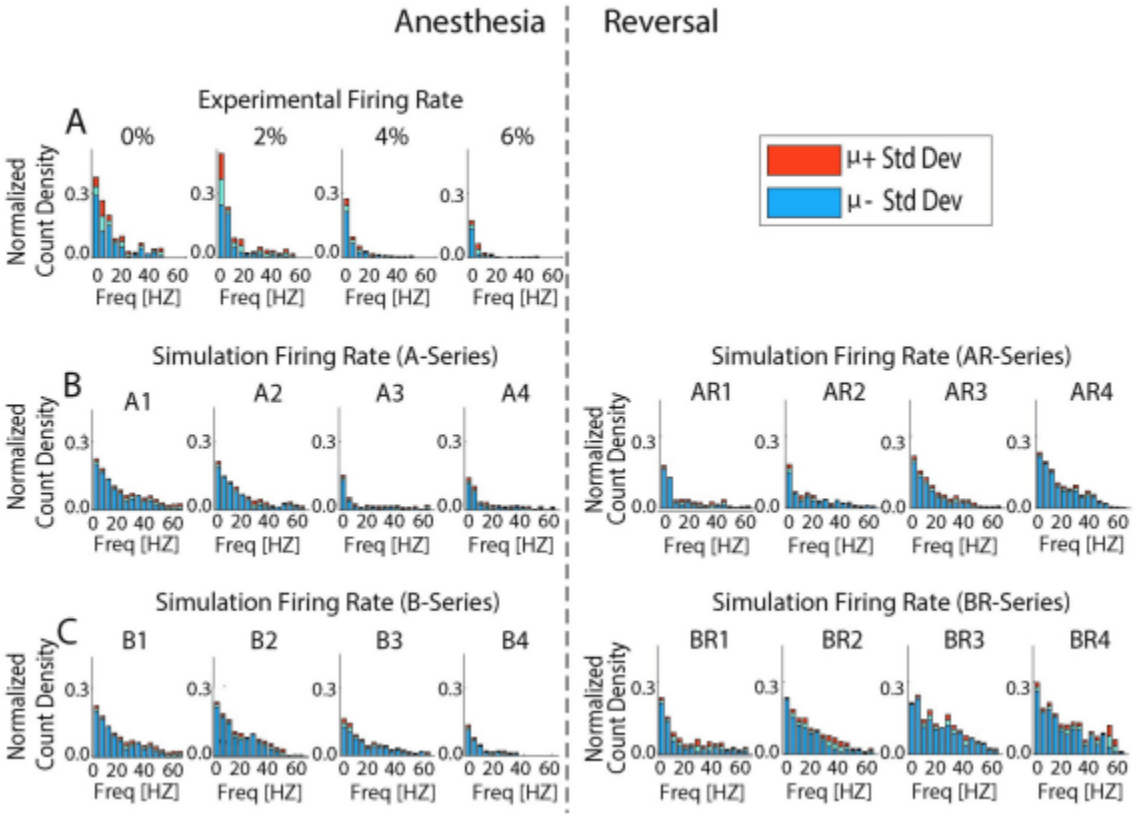

Figure IV.6 Firing rate distributions for different levels of anesthetic concentration.

A) Changes in experimentally recorded firing rate distributions under increasing desflurane concentration (0, 2, 4, and 6%) show increased right skewness for the awake state in comparison to anesthetic states. The bins were normalized by the total number of spikes relative to the awake case (0%). **B) and C)** Firing rate distributions in optimized networks for A (B) and B (C) series parameter sets. Simulated networks show similar trends in frequency distributions when compared to experiment. The predicted ACh-induced reversal shows reinstatement of the right skew. The bins were normalized by the total number of spikes relative to the awake case A1/B1. Upper/Lower bound show histogram standard error. Results based on lowest cost fit parameters.

Neurons Phase Lock for Increasing Anesthesia and Decohere with Decreased M-Current.

In both experimental and simulated results, the common feature was an increase in network synchronization as a function of increased desflurane levels. Mean phase coherence (MPC) measures the consistency of the relative phase that neurons fire with respect to each other thus taking into account non-zero time lag synchrony. Anesthesia increased MPC (Figure IV.7B) in the data and both simulation series (r_E = 0.64, r_A = 0.81, r_B = 0.71, P_E = 0.0052, P_A <0.0001, P_B <0.0001). Moreover, MPC in the awake state showed a significant difference between all subsequent anesthesia states (p<0.0167, Bonferroni) for the data as well as for the A- and B-series (Figure IV.7B).

The anesthetic reversal with increased levels of ACh (i.e. decreased g_{Ks}) led to decreases in MPC. The reversal data for experiment and simulation showed an overall positive trend (rAR=0.50, rBR = -0.52, PAR = 0.0003, PBR = 0.0001); however, a significant difference between the means of individual levels was only present between the highest reversal state and the deepest level of anesthesia for the B-series (B4 and BR4, P<0.0125, Bonferroni) and between the two highest states and the deepest anesthesia for the A-series (A4 and AR4/AR3, P <0.0125, Bonferroni).

Information Theoretic Metrics Decrease in Response to Anesthesia and Increase with Smaller M-Current.

We computed the information theoretic measures network integration (I(X)) and complexity (C(X)) for both experimental data and simulated network activity. Integration I(X) is a generalization of mutual information that measures the amount of total entropy of a system that is accounted for by the interactions among its elements. Integration is zero when system elements are statistically independent [233]. Complexity , on the other hand, measures the total entropy loss due to interaction of system elements, or, equivalently, the difference between the sum of the entropies of the individual elements and the entropy of the entire system. Complexity is low for systems with independent elements or with highly synchronous elements.

Integration and complexity displayed similar changes in both the experiment and simulation with increasing anesthetic concentration (Figures IV.7C and IV.7D). Both displayed negative trends for simulated anesthesia and positive trends for reversal. For the experiment a statistical difference was only found between 0% and 6% for the complexity ($P<0.0167$, Bonferroni) while no significant difference was found for experimental integration. For the simulation, the B-series complexity showed significant changes between B1 and B4, the A-series additionally had differences between A1 and all levels of anesthesia complexity ($P<0.0167$, Bonferroni). Complexity showed significant negative correlation with level of anesthesia for both A and B series as well as the experiment ($re = -0.73$, $r_A = -0.96$, $r_B = -0.75$, $P_E <0.0002$, $P_A<0.0001$, $P_B<0.0001$). The reversal simulation complexity displayed a positive linear trend for both AR and BR-series ($r_{AR} = 0.76$, $rBR = 0.62$, $P_{AR} <0.0001$, $P_{BR} <0.0001$) with significant differences between A4 and all reversal states for the A-series and between B4 and all reversal states with the

exception of BR1 for the B-series ($P<0.0125$, Bonferroni). Consistent correlations were seen for integration ($r_E = -0.55$, $r_A = -0.82$, rB = -0.76, $P_E = 0.0165$, $P_A < 0.0001$, $P_B < 0.0001$) and its reversal ($r_{AR} = 0.47$, $r_{BR} = 0.76$, $P_{AR} = 0.0006$, $P_{BR} < 0.0001$). For the integration simulation, a signifi- cant difference was seen between the awake case and all anesthetic states in the A series and between the wake and highest anesthetic state for the B-series ($P<0.0167$, Bonferroni). For the reversal, significant differences were seen between B4 and all reversal states for th B-series and between A4 and all reversal states with the exception of AR1 for the A-series ($P<0.0125$, Bonferroni).

A difference in trends between the A and B series simulations is indicated by the signifi- cantly more precipitous drop in the measures for the A-series with increasing anesthetic level. This could be due to the differences in network connectivity parameters (i.e., NMDA and $GABA_A$ synaptic strengths) obtained for the two series. Specifically, lower NMDA synaptic efficacy and higher GABA synaptic efficacy leads to effective disconnection of the neurons in the A-series networks, resulting in lower integration and complexity measures.

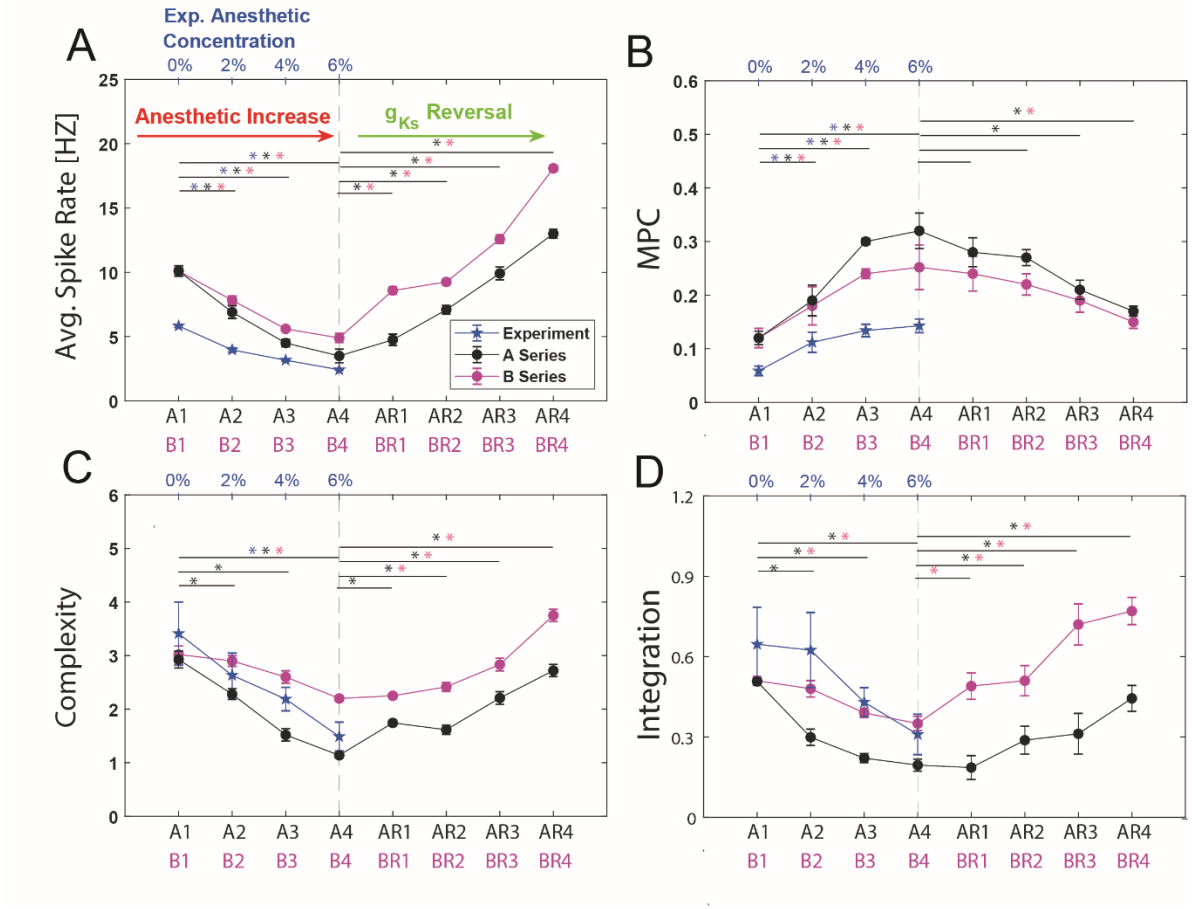

Figure IV.7 Characterization of anesthetic effects on network dynamics and their simulated ACh reversal.

Measures of network dynamics computed from experimental data and optimized model networks as a function of anesthetic concentration and simulated reversal level: **A)** Average spike rate **B)**. Mean Phase coherence **C)** Complexity C(X) **D)** Integration I(X). A1-AR4/B1-BR4 (x-axis) denote simulated anesthetic concentration levels and reversal states obtained in optimized networks with corresponding parameters listed in **Table 2**. Black line denotes simulations with A-series parameter sets (g_{Ks} constant) and pink line denotes simulations with B-series parameter sets (changing g_{Ks}). Blue line (with corresponding axis labels on the top) denotes measures computed from experimental spiking data at different desflurane concentrations. All calculations were made for 6s intervals and then averaged over 5 intervals. Error bars are +/-SEM based on 10 network realizations. Results from lowest cost fit parameters.

Simulated M-current mediated reversal acted to increase both these measures (Fig 4C and 4D; AR/BR series). In the B-series reversal, both measures recovered to values greater than the simulated waking values A1/B1. This was presumably due to the higher NMDA and lower GABAA synaptic efficacies that lead to significantly stronger excitatory interactions between the neurons in the B-series simulations, increasing integration and complexity.

Connectivity Strength Decreases in Response to Anesthesia and Increases with M-Current mediated Reversal.

We estimated network excitatory and inhibitory synaptic strengths, as well as network excitatory and inhibitory connection probabilities, in the optimized networks and compared them directly to these same measures computed from the experimental data. These excitatory and inhibitory network connectivity measures were computed using cross correlogram analysis as described in the section 4.2 (Figure IV.3) and based on previous works [139,234,235].

The optimized networks displayed similar decreases in the strength of excitatory network connectivity with increased levels of anesthetic as observed in the experimental data (Figure IV.8A). When testing for statistical significance via a correlation test we found that anesthesia reduced excitatory strength. The excitatory strength had a significant negative correlation with anesthesia treatment (r_E = -0.79, r_A = -0.81, r_B = -0.77, P_E <0.0001,

P_A<0.0001, P_B <0.0001). The wake state showed a significant difference between all subsequent anesthesia states (P<0.0167, Bonferroni) for the experiment as well as for the A- and B-series. Excitatory strength in the reversal simulation had positive correlations for the A- and B-series (r_{AR} = 0.43, r_{BR} = 0.46, P_{AR} = 0.0018, P_{BR} = 0.0008). For the reversal, the A-series only showed differences between A4 and AR2 whereas the B-series showed differences across all reversal states (P<0.0125, Bonferroni). Both the A-series and B-series results followed similar trajectories, with the A series results reporting somewhat smaller excitatory connectivity strength values. This can be due to the fact that the evolutionary algorithm returned significantly lower NMDA efficacy for the A-series, compared to the B-series. On the other hand, excitatory network connectivity probability is very similar for both parameter series as the structural connectivitiy density of excitatory synapses is the same in all model networks (see section 4.2).

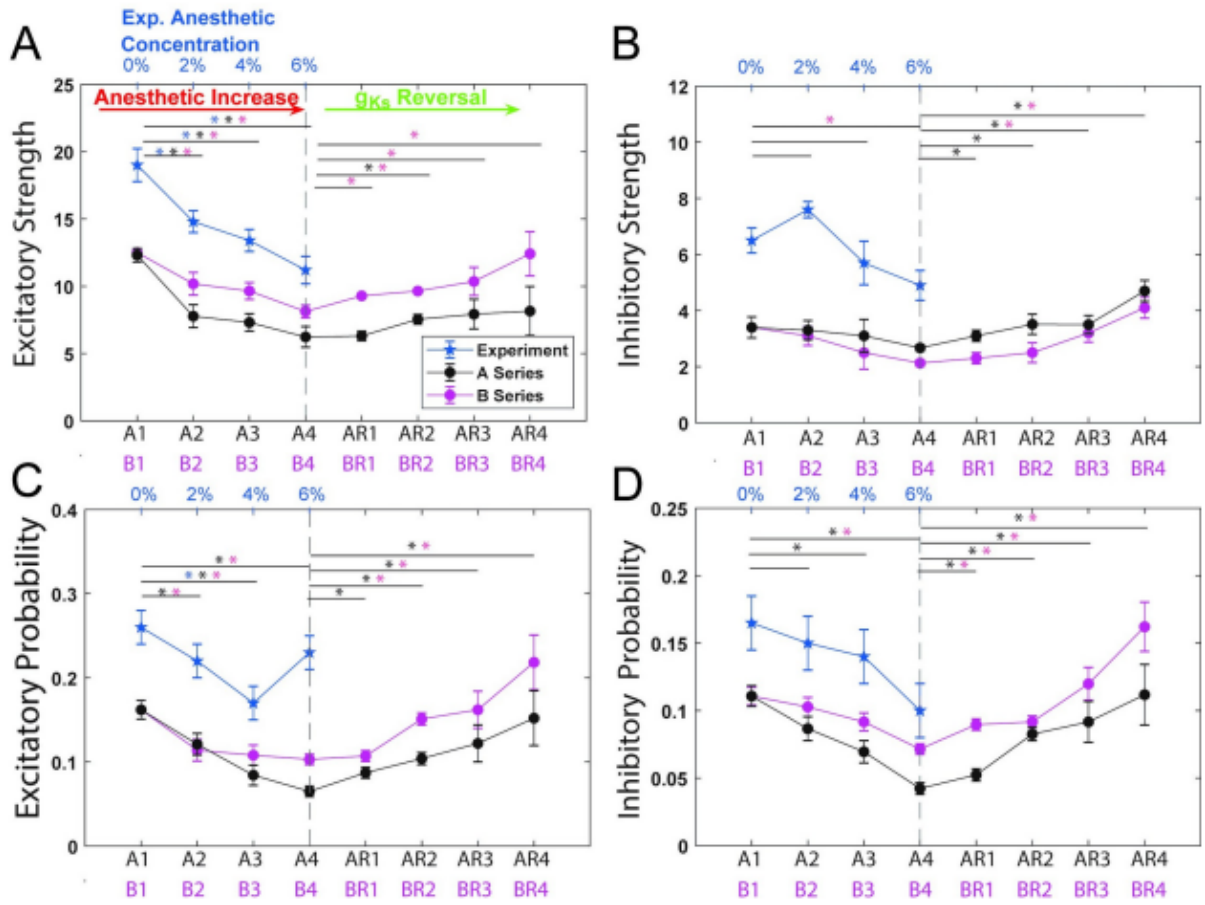

Figure IV. 8. Characterization of anesthetic effects on network connectivity and their simulated ACh reversal.

Measures of network connectivity computed from experimental data and optimized model networks as a function of anesthetic concentration and simulated reversal level: **A)** network excitatory connectivity strength, **B)** network inhibitory connectivity strength, **C)** network excitatory connectivity probability, **D)** network inhibitory connectivity probability. A1-AR4/B1-BR4 (x-axis) denote simulated anesthetic concentration levels and reversal states obtained in optimized networks with corresponding parameters listed in **Table 2**. Blue line (with corresponding axis labels on the top) denotes measures computed from experimental data, black (pink) line denotes measures computed from A-series (B-series) network simulations. In these measures, the presence of a significant connection was determined through cross correlogram analysis as described in section 4.2. Error bars of +/-SEM based on 10 network realizations for best fit optimization.

We found a significant correlation in excitatory probability in the A-series and B-series but not in the experiment. A significant difference was found between all subsequent anesthesia states and the wake state (A1/ B1) for A- and B-series simulations ($P<0.0167$, Bonferroni). The experiment, A-series and B-series had negative correlations but only the A- and B-series demonstrated a significant correlation ($r_A = -0.87$, $r_B = -0.55$, $P_A <0.0001$, $P_B = 0.0053$). Differences were found between all reversal states and A4/B4 except between B4 and BR1 ($P<0.0125$, Bonferroni). The reversal simulation had positive correlations for both A- and B-series ($r_{AR} = 0.54$, $r_{BR} = 0.59$, $P_{AR} <0.0001$, $P_{BR} <0.0001$).

The experimental data, as well as simulation results for both the A and B series networks, showed decreases in inhibitory network connectivity strength and probability as a function of anesthetic concentration. Inhibitory strength showed negative correlations with increasing anesthetic but with a significant correlation only for the B-series ($r_B = -0.54$, $P_B =0.0003$).

There was only a significant difference between the awake state B1 and B4 ($P<0.0167$, Bonferroni). The reversal simulation had significant correlations for both A- and B-series ($r_{AR} = 0.50$, $r_{BR} = 0.61$, $P_{AR} = 0.0002$, $P_{BR} <0.0001$). A significant difference was seen between A1 and all reversal states in the A-series and between B1 and B3, B4 for the B-series ($P<0.0167$, Bonferroni). This seems a counterintuitive result since $GABA_A$ synaptic efficacies increase with desflurane level, and were explicitly modeled as such in our

networks. However, this result may be a consequence of decreases in excitatory network synaptic strength and connectivity probability. Namely, inhibitory cells receive less excitatory drive, subsequently firing fewer spikes and, thus, limiting their effect on postsynaptic targets. Inhibitory probability had significant negative correlations for the simulation A-series and B-series as well as the experiment (r_E = -0.49, r_A = -0.82, rB = -0.71, P_E = 0.021, P_A<0.0001, P_B <0.0001). Only the simulation showed significant differences between the mean of the wake state and the subsequent anesthetic states. The A-series showed a significant difference between A1 and A3 and A4 while the B-series only showed a difference between B1 and B4 (P<0.0167, Bonferonni). The reversal simulation had positive correlations for both A- and B-series (r_{AR} = 0.67, r_{BR} = 0.57, P_{AR} <0.0001, P_{BR} <0.0001). The reversal simulations showed significant differences between the deepest state of anesthesia and all of the reversal states. This means that there was a significant difference between A1 and AR2-AR4 for the AR series and B1 and BR2-BR4 for the BR-series (P<0.0125, Bonferonni). Additionally, we observed that the strength of network inhibitory connectivity in the A-series networks was generally stronger than in the B-series networks. This observation agrees with the fact that the $GABA_A$ conductance is higher in the A-series parameters than in the B-series. Counterintuitively, network inhibitory connectivity probability was lower and more variable in the A-series networks com-pared to the B-series networks.

Effects of ACh-induced Anesthetic Reversal on Network Functional Connectivity

The results discussed above report trends observed for measures of average network activity, such as frequency, mean phase coherence, integration and complexity, as well as network connectivity strength and probability. And while M-current mediated reversal reinstated these network-level measures, the measures do not account for recovery of functional connectivity in the network which would contribute to information processing. In this section, we investigate how M-current mediated reversal affects the relative frequency profile of individual neurons with respect to other neurons in the network and also look at effects of reversal on the cellular- level functional connectivity. These measures specifically assess whether the internal dynamic structure of network activity is reinstated during the ACh reversal.To accomplish this, we first compared the firing rate of each neuron (or unit) in the experimental data and in the optimized networks at each level of anesthetic concentration to its firing rate in the waking state (Figure IV.9 and Figure IV.S1 in the Appendix at the end of this thesis). In the figure panels, the x-axis represents firing frequency of individual cells for different anesthetic levels and the y-axis represents the firing frequency for the same cells in the non-anesthetic (0% or A1/B1) conditions. In this figure each plot shows neurons from 10 different optimizations on a single network structure (neurons from 10 different parameters all on same network). Each dot shows the firing rate of a neuron in the 0% on the y axis and the comparison anesthetic level on the x axis. For the experimental data, mutliple units can be potentially detected on a single electrode. This led to potential ambiguity in neurons assigned across different anesthetic levels. To address this issue, neuron identity was based on firing rate in the 0% case. Namely, for units recorded on each electrode, the fastest firing units for 0% anesthesia were given the same ID as the fastest firing units in the 6% case. The

results showing an overall linear relationship (Figure IV.9 and Figure IV.S1) indicates preservation of relative frequency ordering between the neurons. Deflection of the slope of the linear relationship towards vertical indicates the decrease in absolute firing frequency observed for different anesthetic levels.

We observed that, generally, in both experiments and simulation results the relative frequency of the neurons was preserved, i.e. neurons that fired at higher frequencies as compared to other cells in non-anesthetic conditions retained higher firing frequencies at the different anesthetic levels, albeit absolute frequencies decreased. Conversely, neurons that maintained lower firing frequencies (relative to other cells) in the non-anesthetic state continued firing at lower relative frequencies in the anesthetic conditions. Qualitatively similar results were observed for A-series networks (Figure IV.9) and B-series networks (Figure IV.S1 in the Appendix at the end of this thesis).

Importantly, during the simulated ACh-induced reversal (AR-series in Figure IV.9C; BR-series in Figure IV.S1 in the Appendix at the end of this thesis), the relative relationship between firing frequencies of neurons remained the same, with individual cell frequencies increasing back towards their non-anesthetic values as evidenced by the slope of the linear relationship for higher reversal states tending towards one. This result suggests that individual cells return to roughly the same firing rates during ACh-induced reversal as they exhibited in the simulated waking state. The relationship between firing frequencies had a signficant linear relationship in the simulation (Figure IV.9B and Figure IV.9C) with all relationships displaying significant positive correlation ($P<0.0001$). The

experimental relationship (Figure IV.9A) also had a positive significant relationship ($R_{0,2\%}$ = 0.51, $R_{0,4\%}$ = 0.46, $R_{0,6\%}$ = 0.52, $P_{0,2\%}$ = 0.0124, $P_{0,4\%}$ = 0.0271, $P_{0,6\%}$ = 0.0092).

Further, to explore detailed changes in cellular-level functional connectivity in the optimized networks, we created functional adjacency matrices from the estimated pairwise excitatory connectivity strengths at all simulated anesthetic and reversal conditions, measured via identification of the peak/trough of the spiking cross correlogram as described in thesection 4.2. We then calculated the cosine similarities between the created functional adjacency matrices obtained for each anesthetic and reversal level (Figure IV.10). A cosine similarity of 1 indicates that the functional adjacency matrices are identical, whereas cosine similarity of zero indicates that they are uncorrelated. We then calculated the Z-score of the cosine similarity matrix by comparing the cosine similarity for simulated spike trains with the cosine similarity of connectivity computed from jittered spike trains as described in the Methods. Having a high Z-score indicates how the functional connectivity differs from random. The analysis was performed on experimental data as well as A-series and B-series fits, on all measured excitatory connections. Supplementary Figure IV.S3 shows example of functional connectivity observed for an individual experiment, simulation and its reversal.

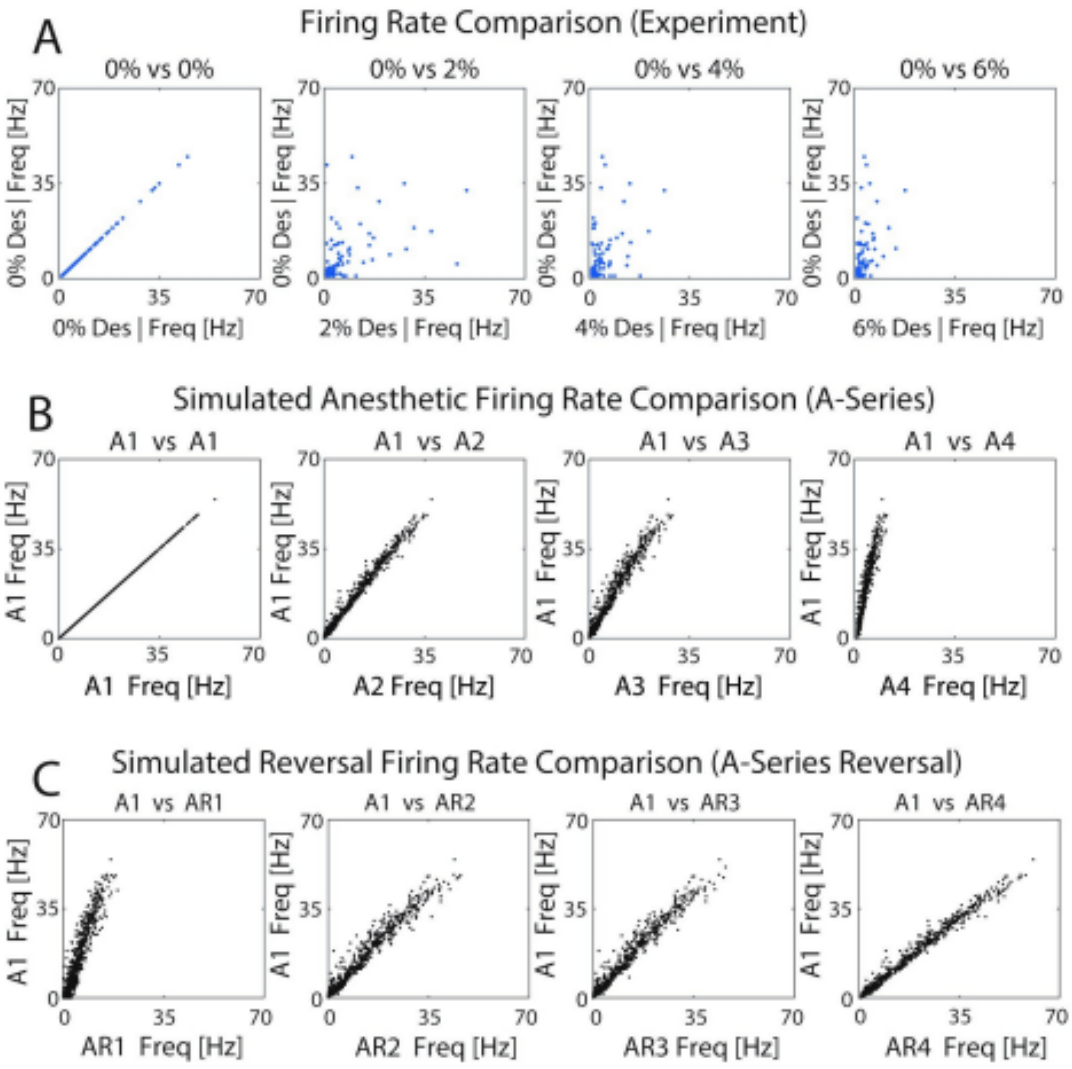

Figure IV.9 Effects of anesthetic concentration and simulated ACh-induced reversal on relative profiles of neuronal firing frequency.

Each panel depicts the firing frequency of each neuron in a given anesthetic/reversal state (x-axis) compared to its firing frequency in the non-anesthetic condition (0% desflurane or A1) (y-axis) **A)** Units recorded in the experimental data; **B,C)** Neurons in A series optimized networks and reversal.

We observed that the functional network similarity matrices, for experimental data as well as model results, became less correlated with each other with increasing anesthetic levels (Figure IV.1). At the same time, for the model data, M-current mediated reversal resulted in a significant increase in the correlation between the baseline non-anesthetic adjacency matrix (A1 or B1) and the fully reversed functional adjacency matrix (AR4 and BR4). The experimental data had similar behavior with increased similarity between the 0% and 2% anesthesia states when compared to the similarity between 0% and 4%, 6%. The interesting feature of the experimental data is that 6% and 4% had increased similarity when compared to each other than with other anesthetic states (Figure IV.10). This was not seen in the simulation.

In summary, our model results showed that multiple measures of network connectivity (Figures IV.8 and 10) increased with ACh-induced simulated reversal suggesting that increases in cellular excitability, mediated by muscarinic effects of ACh, can reinstate network dynamics dictated by synaptic connectivity.

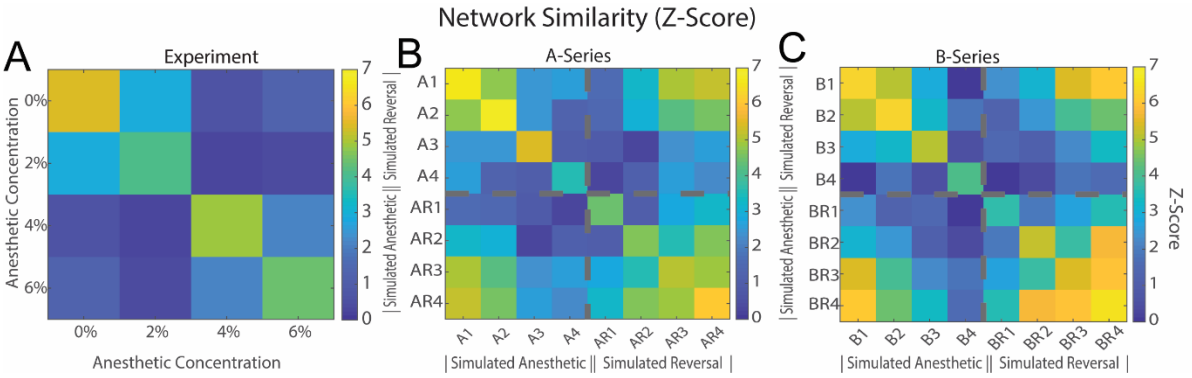

Figure IV.10 Effects of anesthetic concentration and ACh-induced reversal on the similarity between cellular functional connectivity.

Cosine similarity Z-Score was computed for every pairwise functional connection between neurons. **A)** Experimental functional connectivity was computed between the highest firing neuron for each electrode with similarity computed across different levels of anesthesia**. B,C)** Functional network similarity computed for simulated anesthesia and reversal. Z-Scores were computed comparing the Network similarity to mean and standard deviation of similarities for distributions randomly jittered +/- 5 milliseconds. Each is averaged over ten runs.

4.4 Discussion

The goal of this investigation was to simulate the multisynaptic effects of an anesthetic and the modulating effect of muscarinic ACh receptor activation in a neuronal network model. To do this, we applied a computational model of a network of excitatory and inhibitory neurons and used a differential evolution algorithm to fit model parameters to match measures of spiking activity, neuronal connectivity, and network dynamics recorded in the visual cortex of rodents during anesthesia with desflurane in vivo.

We first examined if excitatory and inhibitory synaptic changes typically produced by the inhalational anesthetic desflurane led to neural network behavior similar to experimentally observed neuron activity as characterized by various measures including population firing rate, phase coherence, monosynaptic spike transmission, and the information theoretic measures integration and complexity. Second, we investigated if an exogenously induced increase in the level of ACh acting on muscarinic receptors and the M-current could reverse the effect of the anesthetic as suggested by prior behavioral experiments.

Simulation of the Anesthetic Effect

We simulated the effect of anesthetic desflurane on the neuronal network by reducing the response of excitatory synapses and facilitating that of inhibitory synapses. General anesthetics commonly potentiate GABAergic synaptic receptor transmission through

modification of inhibitory post synaptic potential (IPSP) amplitude and duration, as well as through inhibition of glutamatergic receptor excitatory post synaptic potential (EPSP) amplitude and duration. The relative strength of these effects depends on the class of anesthetic[135,153]. Desflurane inhibits binding at NMDA receptors while potentiating postsynaptic inhibition at $GABA_A$ receptors. Some anesthetics, but not desflurane, also suppress AMPA receptors. The effect of anesthetics on nicotinic and muscarinic receptors is more diverse. Some anesthetics also modify the activity of cholinergic neurons projecting to the cortex [150]. Regarding its electrophysiological effects, desflurane has been shown to decrease average spike rate, excitatory and inhibitory monosynaptic transmission, and population measures of neuronal interactions in the cortex [139,242]. These changes in neuronal activity observed in vivo have not been directly linked to the corresponding synaptic effects observed in vitro.

In our study we found that potentiation of inhibitory GABAergic and inhibition of excitatory glutamatergic NMDA synaptic receptors do indeed lead to graded decreases in population activity and increases in synchronization, as quantified by firing rate and mean phase coherence, as well as measured decreases in integration and complexity. Additionally, we were able to recover changes in functional network connectivity which matched changes seen in literature [243,244]. The simulation results were robust; although only a few of the measures (frequency, MPC, I(X) and C(X)) were used for optimization of model parameters via the differential evolution algorithm, the results held for a wide range of non-fitted measures within limits that produced physiologically reasonable spiking behavior. The correlation test, when giving significance for the

experiment and the simulation, gave the same sign of correlation for each metric. Specifically, this validates that our model correctly accounts for the same trends observed in the experiment in response to anesthesia. Moreover, the parameter fits obtained for increasing levels of anesthetic matched in their relative magnitudes to the reported anesthetic induced changes in synaptic efficacy.

Understanding the Mechanism of Anesthesia through Computational Modeling

The cellular mechanism of anesthetic action with respect to loss of awareness has been a subject of intense investigation. Computational models are actively used to make progress in this area of research. Because differing classes of anesthetics elicit different effects on synaptic receptor subtypes, many modeling approaches aim to determine how nuanced changes in receptor binding and synaptic activity lead to changes in neural or electroencephalographic activity. For example, in mean field models, GABAergic and glutamatergic synaptic changes are attributed to a single parameter that maps to different concentrations of general anesthesia [245]. Other modelling approaches seek to understand the mechanism of specific anesthetic agents; for example, the effects of propofol have been studied through the modeling of both $GABA_A$ and $GABA_B$ amplitude/duration and the effects on cortical synchrony and EEG rhythms [151,246]. Enflurane and isoflurane are other commonly modeled anesthetics where the roles of both glutamatergic receptor binding and GABAergic effects are taken into consideration[246–248] . Anesthetic action effected through post synaptic potential (PSP) changes, from a modelling perspective, is a relativity robust explanation supported by its effectiveness across modelling paradigms. These include “mean field” models as well as

networks of “integrate and fire”, “Izhikevich “and “HH” neurons, which all show reduced activity and changes to population synchrony when modeling anesthetic effects on synaptic receptors [247,249,250].

Our study is distinguished from former computational models of anesthetic effects by the independent consideration of the effects on $NMDA_R$ and $GABA_R$ through PSP changes, as well as of cholinergic influence through changes in the muscarinic M-current. We also used a more biologically realistic log-normal distribution for synaptic weights[230]. Because we had access to experimental spike data, we were able to directly fit our model to empirical data at graded levels of anesthesia and then test our hypothesis regarding cholinergic anesthesia reversal.

Anesthetic Effects on Spike Synchrony

A common brain signature of general anesthesia is the loss of global functional connectivity between specialized regions of the cortex while local populations show increases in neural synchrony [243,251,252]. Cellular and network mechanisms leading to neural synchrony have been studied extensively in the field of computational neuroscience [253–255]. A set of possible network wide mechanisms are the PING (pyramidal interneuron network gamma) class of mechanisms, where stable, synchronous activity patterns emerge when inhibition periodically shuts down excitation in the network [214,226,256–258]. The propensity of neural network synchrony can also

depend on intrinsic cellular excitability properties, an example being changes from Type 1 to Type 2 membrane excitability. Type 1 and Type 2 neural excitability describe the well-characterized differences in spike generation dynamics that can generally occur between different types of neurons, and can occur in the same neuron under different pharmacological conditions, such as changing ACh levels. Type 2 dynamics originate from increased competition between depolarizing and hyperpolarizing currents as compared to Type 1 [158]. These differences exemplify themselves in the onset and steepness of firing frequency-input (i-f) curves and the shape of phase response curves (PRCs) which in turn determine synchronization of the networks. Neurons exhibiting Type 1 excitability respond more rapidly with higher firing frequency changes to changing stimulus magnitude as compared to Type 2 cells, and also decreased propensity to synchronize stemming from the shape of their PRC curves [85,157,259].

Thus, as also discussed below, ACh can play a double edged role in affecting network synchrony via the muscarinic receptor system. On one hand, decreasing levels of ACh during increased anesthesia levels can promote synchrony, as it has been shown that activation of the K+ M-current mediates the transition from Type 1 to Type 2 membrane excitability [76], while on the other hand, the increase of ACh-mediated effects during reversal can offset the decreasing synaptic efficacies with higher cellular responses (increasing steepness of i-f curve). In our modelling results simulated anesthetic effects and M-current mediated reversal, we show that we can evoke transitions between high frequency asynchronous population behavior and low frequency synchronous activity via both mechanisms: by potentiation of IPSPs and inhibition of EPSPs, and ACh-mediated

modulation of cell excitability. For higher levels of anesthesia, while both the simulations and the experimental data showed increasing MPC, simulated networks exhibited a larger increase. This could be due to the fact that our model only represents local network interactions, without incorporating the existence of external inputs that could additionally desynchronize network activity leading to decreased MPC. For example, in the visual cortex, there are non-local network inputs possibly preventing a high level of synchronization in the locally recorded network activity and reflected in lower MPC values in the experimental data. However, overall, our model results demonstrate that it is possible for the population synchronization observed in response to anesthesia to develop in response to changes in PSP alone or to concurrently active cellular mechanisms.

Predicting Anesthesia Reversal by ACh

Prior experimental studies demonstrated that the behavioral expression of the anesthetic state can be reversed by stimulating the cholinergic system of the brain by various means in vivo and in vitro in both humans and animals[148,150,260,261]. To date, no modelling study has attempted to simulate the reversal of neuronal effects of anesthesia by modulating the interaction between cholinergic and other synaptic effects. In this work we demonstrated that ACh limited to act only via blocking the muscarinic slow potassium M-current can reverse the general anesthetic effect on spiking dynamics and population activity, via mechanisms described above. Specifically, we showed that decreasing the influence of the M-current under simulated anesthesia leads to an increase in firing rate and neural interaction measures, showing a population wide reversal of anesthesia-

induced synaptic changes. This finding suggests a possible cellular mechanism for the induced reversal of anesthesia effects on PSPs consistent with experimental studies[144,262].

The role of muscarinic ACh receptors in affecting the state of the animal depends largely on the type of general anesthetic used. Desflurane exerts a nonlinear effect on muscarinic ACh receptor activation in a concentration-dependent manner [138]. We also showed that the addition of decreasing acetylcholine influence via the muscarinic pathway during anesthesia (B series) leads to similar reversal endpoints to those with altering NMDA and GABA synaptic changes alone (A series). The choice to model changes in anesthetic ACh influence (B series) in addition to synaptic changes alone (A series) was made to generalize the effects of common inhalational anesthestics which can affect both the cholinergic as well as the glutamatergic and GABAergic pathways (Figure I.4). By considering solely the effect of changes on IPSPs via $GABA_R$ and EPSPs through $NMDA_R$ we show that not only can changes in population activity (firing rate, synchronization and entropy), be accomplished without changes in cholinergic influence but that increasing cholinergic influence alone can reverse these effects. This demonstrates that cortical cholinergic presence has the potential to mitigate the general effects of inhalational anesthesia. In many cases, however, such as for the effects of desflurane, inhalational anesthesia can affect muscarinic and nicotinic ACh receptor binding and for this reason we decided to model the cooperative effects from changes in synaptic EPSP/IPSP and cellular excitability changes via the M-current. In the case of cholinergic reversal,

however, this confounded the role of ACh, as the changes in ACh due to anesthesia could be argued to be trivially reversed in the reversal states.

In this study, we used measures of synaptic functional connectivity, computed from average pairwise correlations of neuron spiking, to quantify changes in overall network behavior in both anesthesia and reversal conditions. We showed that the cosine similarity in the functional connectivity matrix increased for the full reversal state when compared to the high anesthetic state. This means that specific neuron to neuron functional connectivity was highly correlated between the awake and reversal states but not the anesthesia states. This suggests that the functional topology of a network can be reversed through a different receptor pathway than is used to achieve the state of anesthesia. Likewise, the population measures of integration and complexity were increased by the cholinergic decrease in M-current. In fact, prior experimental studies showed that muscarinic receptor activation could reverse isoflurane-induced changes in electroencephalogram cross entropy a quantity related to brain functional complexity presumed to be associated with the conscious state [262,263].

In the past, anesthesia reversal has been achieved by a variety of drugs and methods of administration in experimental studies. For example, microinjection of nicotine into the thalamus led to the recovery of the righting reflex in rodents anesthetized by sevoflurane [148], and a similar reversal from isoflurane was observed in response to microinjection of histamine into the basal forebrain [264]. Unlike general anesthesia, however, the

mechanisms for induced reversal may be specific to the type of anesthetic agent used. An example of this can be seen when comparing the effects of the $GABA_A$ antagonist, gabazine, on the effects of propofol as well as ketamine [265]. The application of gabazine led to wake-like responses when rats were sedated with propofol, which acts through potentiation of $GABA_A$ receptors, but gabazine was ineffective when used during administration of ketamine, which has been known to act through modulation of NMDA receptors. These previous studies suggest that the phenomena of induced reversal can be demonstrated in controlled rodent studies, but a similar effect has been suggested in human studies [266]. Another example is the clinical case where a patient's use of Ritalin, a central nervous system stimulant, led to complications achieving sedation under the standard general anesthetic dose [267]. In rodents, Ritalin was found to cause emergence from sedation induced by isoflurane [268].

Our results predicting cholinergic recovery of neuronal population dynamics, inter-neuronal functional connectivity and complexity lends support to the evidence that the brain state altered by anesthesia is at least partially reversible. In clinical use, the effects of anesthesia can linger after the drug is no longer administered [269]. For this reason, there are both translational and phenomenological motivations to investigate induced recovery from anesthesia. Our study gives insight into the synaptic and network mechanisms by which central nervous system changes caused by anesthesia can be mitigated by the administration of a functional agonist.

Chapter V

Conclusion

5.1 Summary

In this dissertation, we investigated the impact of ACh on memory formation and anesthetic action by modelling cholinergic influence on neuronal excitability and population activity in neuronal networks. In Chapter II we explored how changes in ACh tone, through changes of neuronal excitability, can alter the ability for the network to encode rate and phase information. We found that in high ACh conditions, high gain is beneficial in widening the firing rate distribution for a given range of synaptic inputs. Low SFA allows neurons to persist in firing to maintain a representation in frequency space and low synchrony facilitated by Type 1 PRC, prevents a reduction in frequency variation. For phase coding under low ACh conditions, low gain reduces frequency variation in the network, while a Type 2 PRC induces increased synchronizability for phase locking to persist. Thus, reductions in ACh level provide two dynamical substrates for phase coding: (1) near uniformity in firing rates across the network, and (2) the ability of neurons to collectively organize into network-wide synchronous behavior.

This theoretical work was applied to memory formation and anesthetic action (Chapters III and IV). In Chapter III we explored how cholinergic influence affects learning through

phase remapping of neuronal frequencies during the transition from waking to NREM sleep states. In this work, we implemented a neuronal network with spike time dependent plasticity and showed that remapping of wake-associated, firing frequency-based representations is based on NREM-associated changes in neuronal excitability mediated by the ACh-gated slow potassium current (m-current). We also showed that learning-dependent reordering of sequential firing in the hippocampus during NREM sleep, together with spike timing-dependent plasticity (STDP), reconfigures neuronal firing rates across the network. This rescaling of firing rates has been reported in multiple brain circuits across periods of sleep.

Our reduced model demonstrates that changing ACh levels during wake and NREM sleep can play a key role in memory consolidation. We found that increased functional network stability (FuNS) is associated with stronger low-frequency oscillatory patterning of the network and predicts the degree of fear memory consolidation. This increased stability, in turn, allows for structural network reorganization which facilitates recruitment of new cells into memory representations. Namely, when synaptic strength in the model is allowed to evolve through STDP, we observed this reorganization of firing rates across NREM sleep—with sparsely firing neurons increasing their firing rate substantially, and highly active neurons decreasing their firing rate. These results are also observed in CA1 during sleep-dependent CFM consolidation. We again observed a disruption of these effects when the oscillatory network activity was reduced via manipulations of interneurons.

In Chapter IV we investigated the role of cholinergic influence on the function and reversal of the anesthetic mechanism of action. In our neural network models, we used a differential evolution algorithm to fit synaptic parameters to match network dynamics recorded *in vivo* in the visual cortex of rodents during anesthesia with desflurane. We found that potentiation of inhibitory GABAergic and inhibition of excitatory glutamatergic NMDA synaptic signaling does indeed lead to graded decreases in population activity and increases in synchronization, as quantified by firing rate and mean phase coherence, as well as decreases in network integration and complexity measures. Additionally, we were able to recover changes in functional network connectivity which matched changes seen in literature [243,244].

Additionally, we showed that decreasing the influence of the m-current, mimicking increased cholinergic tone, under simulated anesthesia leads to an increase in firing rate and neural interaction measures, showing a population wide reversal of anesthesia-induced synaptic changes. This finding suggests a possible cellular mechanism for the induced reversal of anesthesia effects on PSPs consistent with experimental studies [144,149]. We also found that considering muscarinic receptor effects of acetylcholine in addition to anesthetic-induced synaptic changes predicts reversal of the neurons' spiking activity, functional connectivity, as well as pairwise and population interactions.

Taken together, our results suggest that acetylcholine, by affecting neuronal properties, can play a critical role as a universal mesoscopic network mechanism capable of regulating network dynamics across cognitive states and underlying what is commonly referred to as systems memory consolidation.

5.2 Future Directions

Our modelling work was primarily conducted using simplified neuronal models. This was apropos for our theoretical work but could use augmentation in applied studies. In the future, more comprehensive models that take into account cortical architecture, thalamocortical interactions and a broader array of cellular mechanisms will help to fully understand the complex roles of cholinergic modulation in producing observed neuronal network and behavioral effects under learning conditions and under anesthesia. For our model of memory consolidation, while the form of learning modeled here is not reliant on sequential neuronal activation during memory encoding, one possibility is that a similar mechanism may be associated with consolidation of memories for events during which neurons are sequentially activated [58– 60]. Future studies will be needed to examine how temporal patterning of neuronal activity during post-learning NREM sleep relates to previously studied “replay” of firing sequences reported in structures like the hippocampus during sleep following sequential spatial tasks. One possibility is that sequential replay presents a special case of NREM-dependent patterning of firing based on prior wake firing rates.

Finally, I note that while we investigated cholinergic influences on neural network dynamics, the direct causal role of the ACh-induced dynamic network changes on memory consolidation remains uncertain. To show causality, future experiments would need to directly link a disruption of the cholinergic signaling with learning deficits.

Appendix

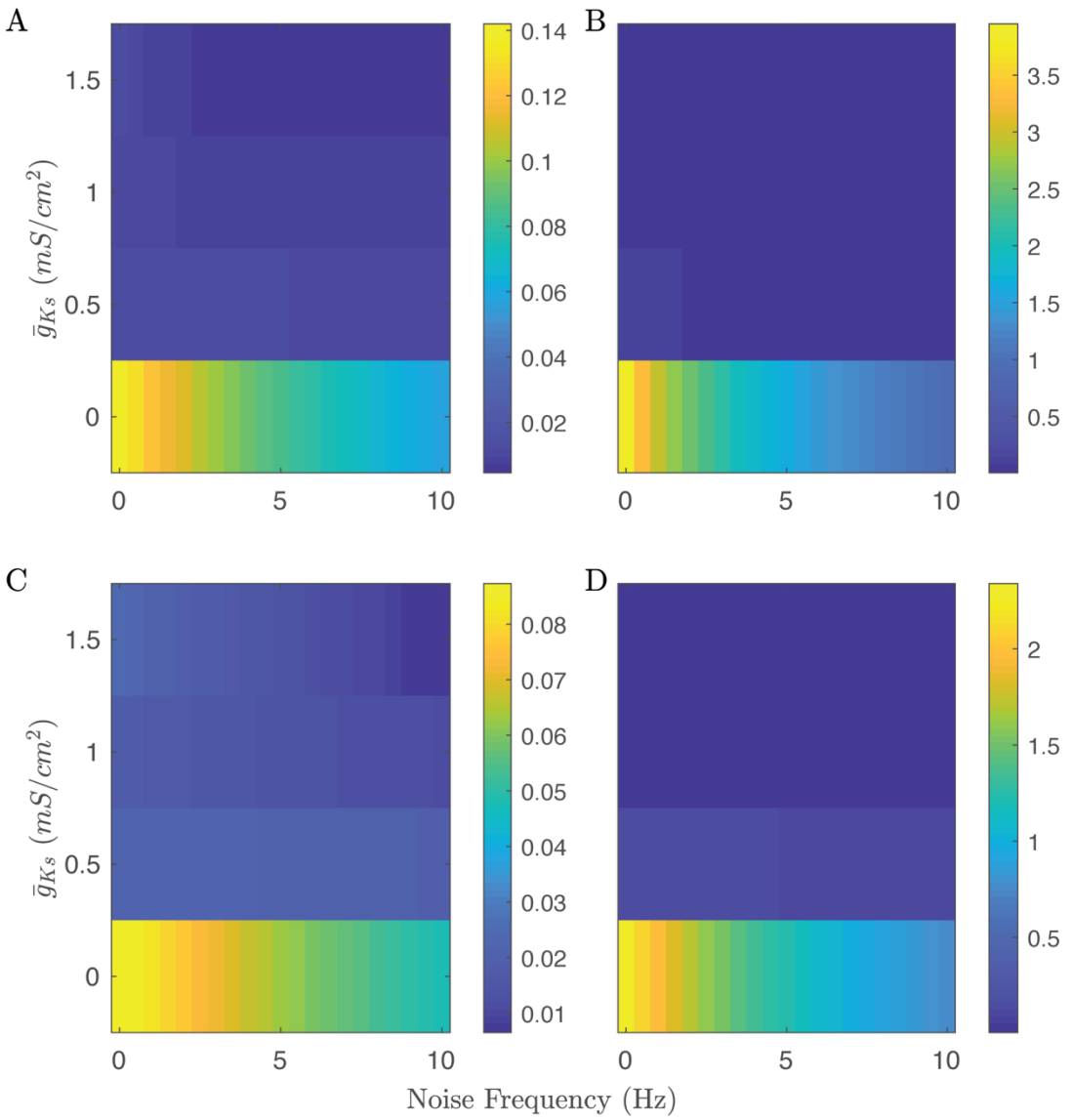

Supplementary Figure II.S1 Network frequency similarity scores for increasing noise with external input patterns (A&B) and on different networks (C&D). Low $\bar{g}_{Ks}$ networks rate code better than high $\bar{g}_{Ks}$ networks over all noise levels (A) NS_{Freq} and (B) $\widetilde{NS}_{Freq}$ are shown for input patterns. (C) NS_{Freq} and (D) $\widetilde{NS}_{Freq}$ for varying network structure.

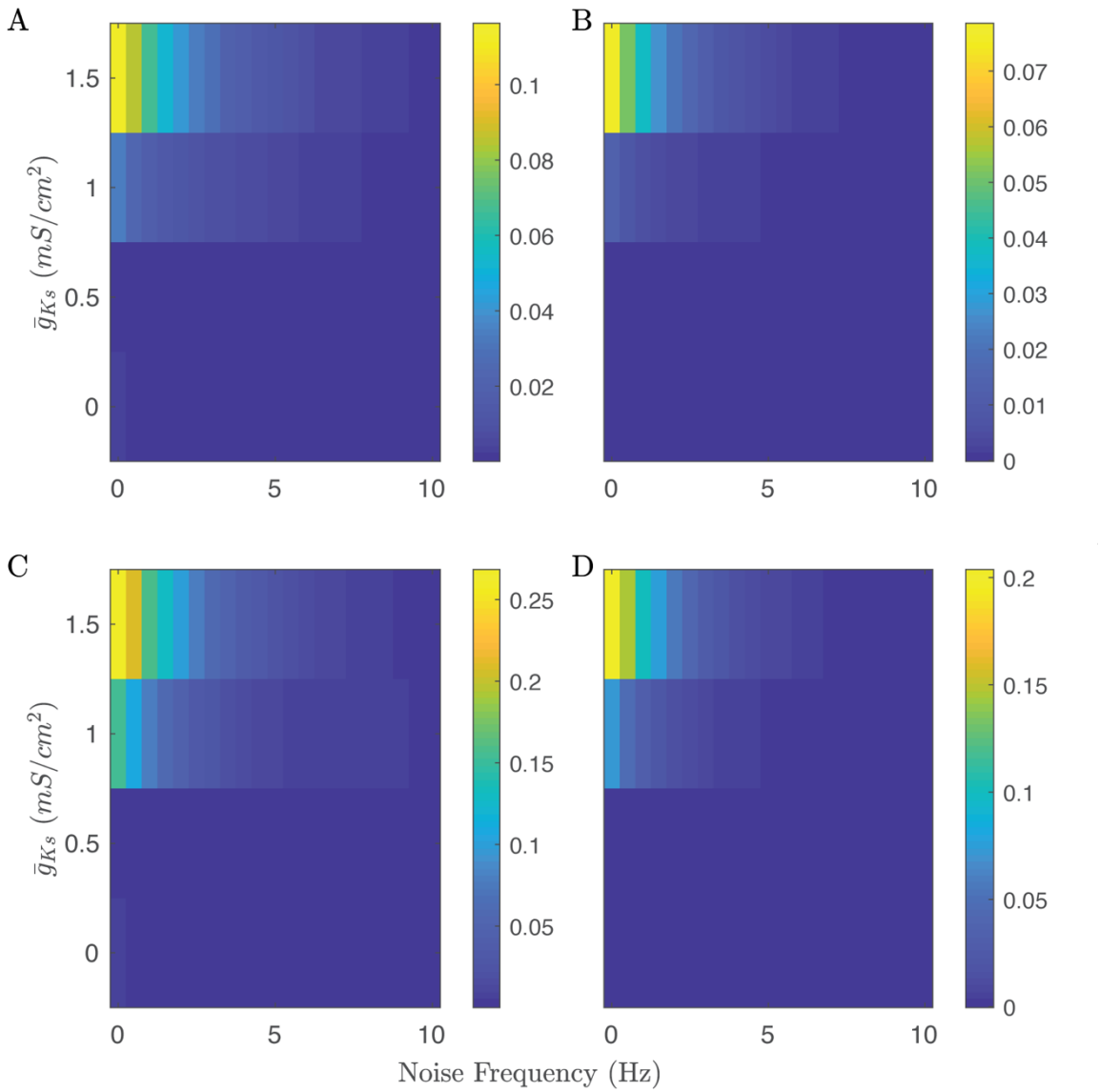

Supplementary Figure II.S2 Network phase similarity scores for increasing noise for external input patterns (A&B) and different network structures (C&D). High $\bar{g}_{Ks}$ networks phase code better than low $\bar{g}_{Ks}$ networks, but phase coding overall is highly noise dependent. (A) NS_{Phase} and (B) $\widetilde{NS}_{Phase}$ for input pattens. (A) NS_{Phase} and (B) $\widetilde{NS}_{Phase}$ for for network structures.

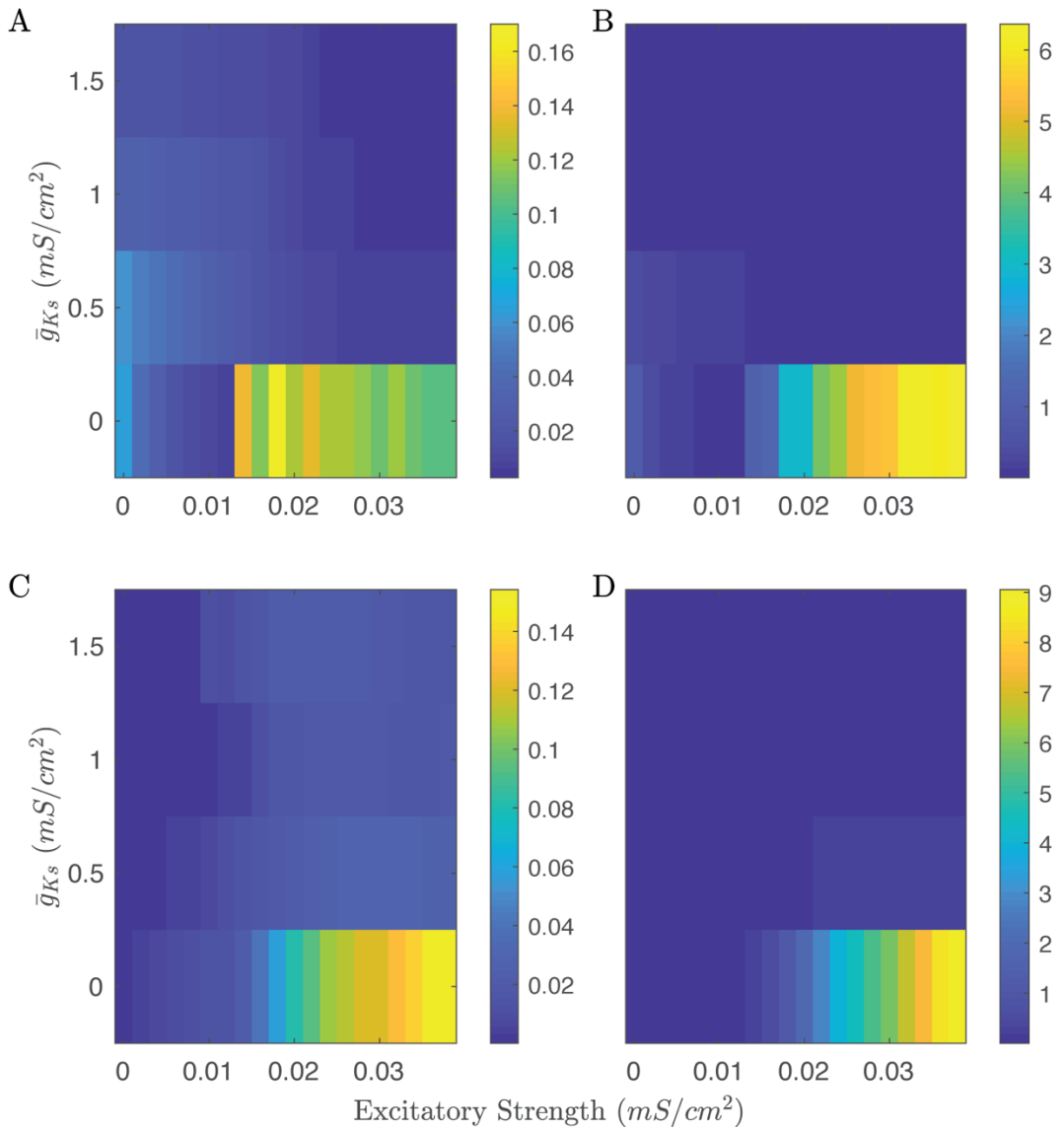

Supplementary Figure II.S3. Network frequency similarity scores for increasing excitatory coupling with external inputs (A&B) and network structures (C&D). Low $\bar{g}_{Ks}$ networks rate code better than high $\bar{g}_{Ks}$ networks with increasing performance as coupling increases. (A) NS_{Freq} and (B) $\widetilde{NS}_{Freq}$ for input patterns. (C) NS_{Freq} and (D) $\widetilde{NS}_{Freq}$ for network structures.

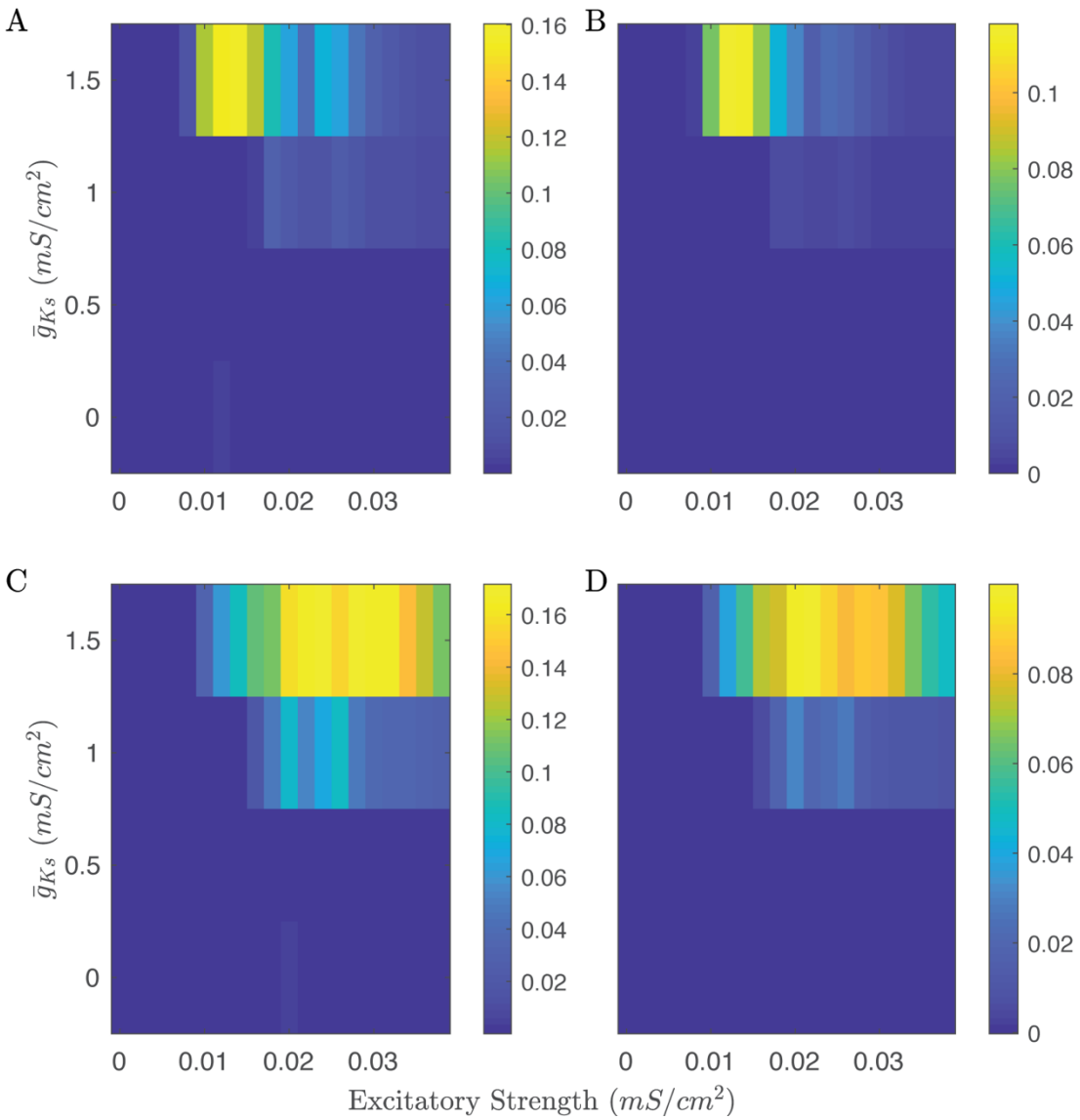

Supplementary Figure II.S4. Network phase similarity scores for increasing excitatory coupling with varying inputs (A&B) and network structures (C&D). High $\bar{g}_{Ks}$ networks phase code better than high $\bar{g}_{Ks}$ networks once coupling reaches a sufficient level and decreases for vary strong coupling. (A) NS_{Phase} and (B) $\widetilde{NS}_{Phase}$ for input patterns. (C) NS_{Phase} and (D) $\widetilde{NS}_{Phase}$ for network structures.

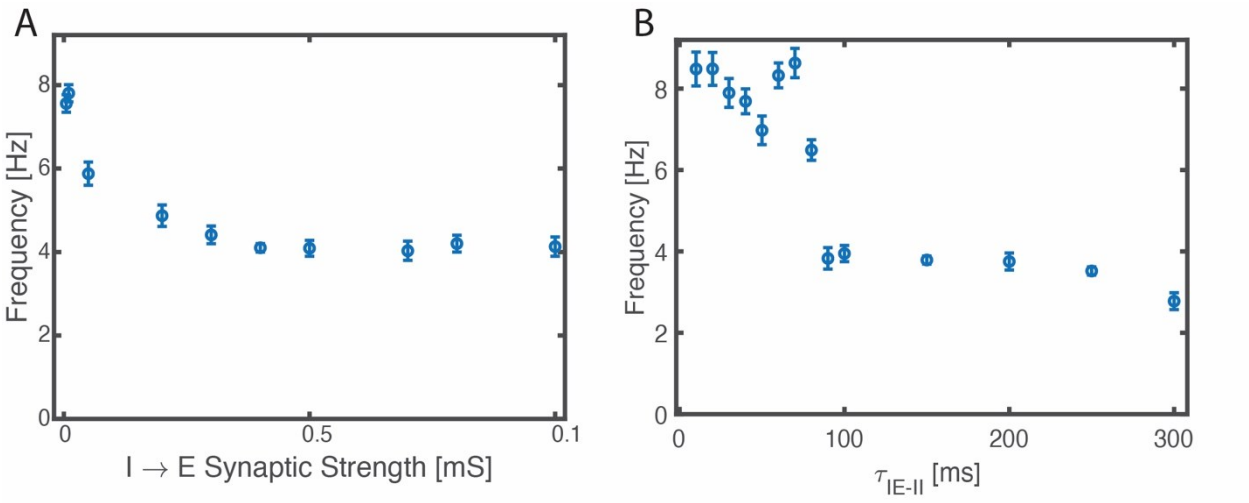

Supplementary Figure III.S1 Frequency dependence on Time constant and Synaptic Strength.

The peak frequency of slow oscillations during NREM sleep like state, can be regulated via strength of inhibitory connectivity to excitatory cells (A) as well as time constants regulating decay of inhibitory postsynaptic currents (B). The specific frequency of slow oscillations during NREM sleep like state does not affect the observed dynamic and structural network reorganization.

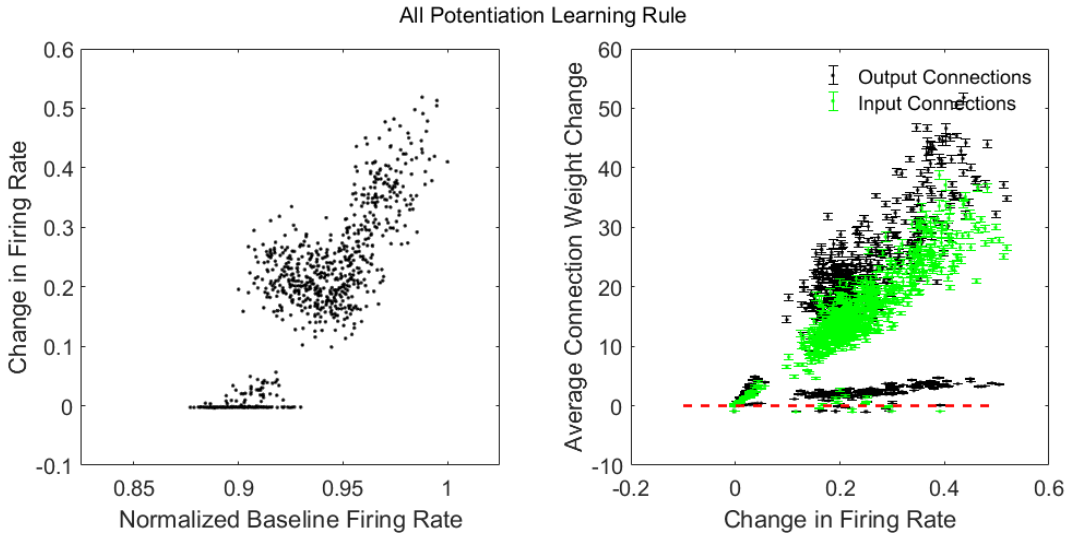

Supplementary Figure III.S2. Effects of all-potentiating STDP Frequency dependence on Time constant and Synaptic Strength.

Left: change of spiking frequencies as a function of the initial spiking frequency of the cell. **Right:** relationship between change of neuronal input (green) and output (black) and spiking frequency change.

.

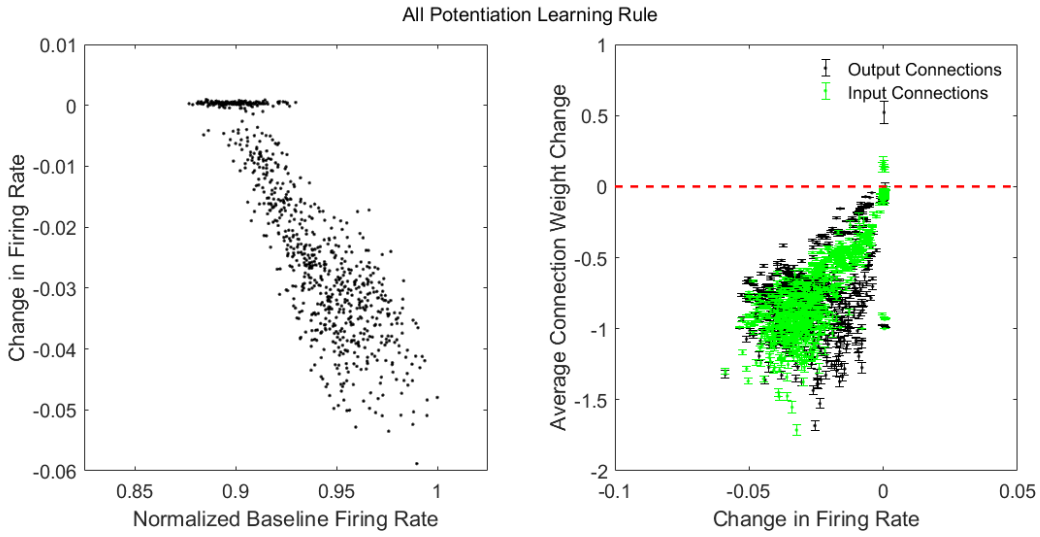

Supplementary Figure III.S3. Effects of all-depressing STDP

Left: Change of spiking frequencies as a function of the initial spiking frequency of the cell. **Right:** Relationship between change of neuronal input (green) and output (black) and spiking frequency change.

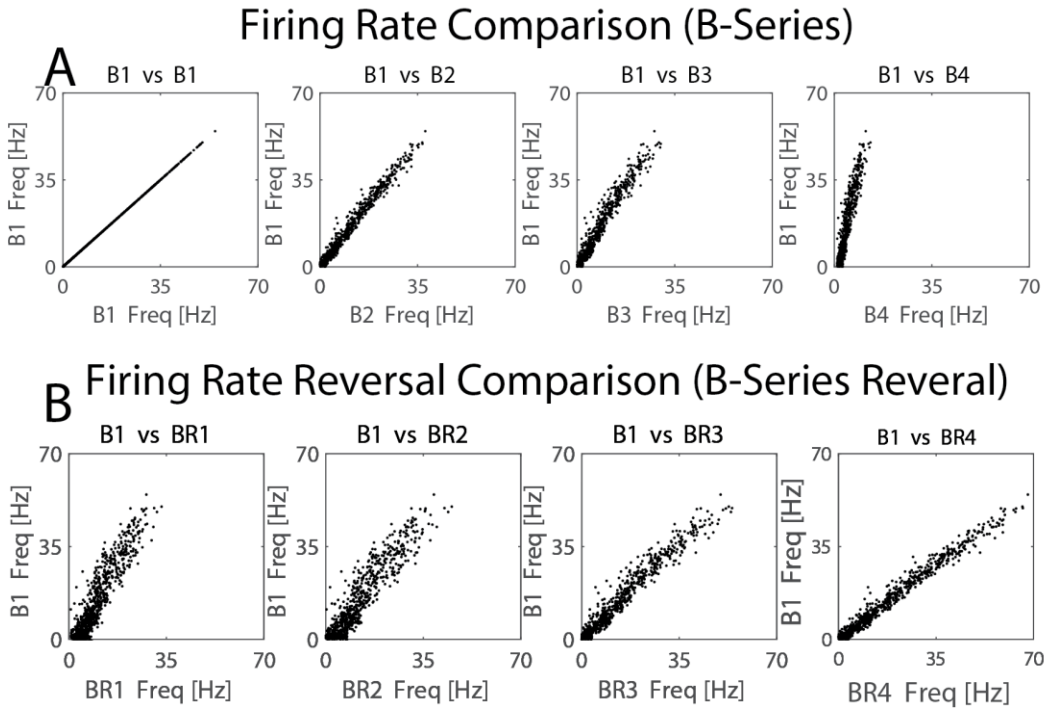

Supplementary Figure IV.S1 B-Series Firing Rate Reversal

Effects of anesthetic concentration and simulated ACh-induced reversal on relative profiles of neuronal firing frequency. Each panel depicts the firing frequency of each neuron in a given anesthetic/reversal state (x-axis) compared to its firing frequency in the non-anesthetic condition (B1) (y-axis) A,B) Neurons in B series optimized networks and reversal.

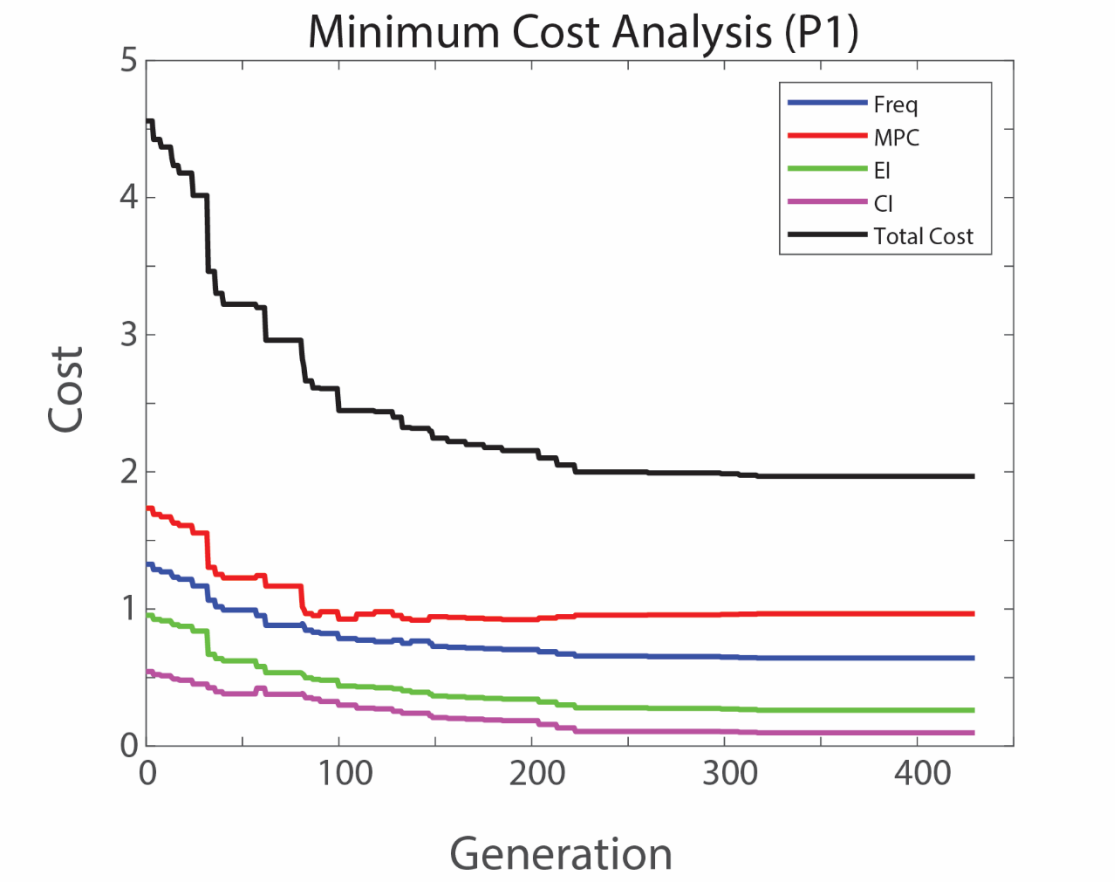

Supplementary Figure IV.S2. Error cost analysis for the lowest cost fit.

For each generation, 10 agents (parameter sets) with the highest cost function from the population of 30, were chosen for replacement. Algorithm was repeated until stopping criteria of 100 generations without change in lowest cost function value across the population was met and performed on single network.

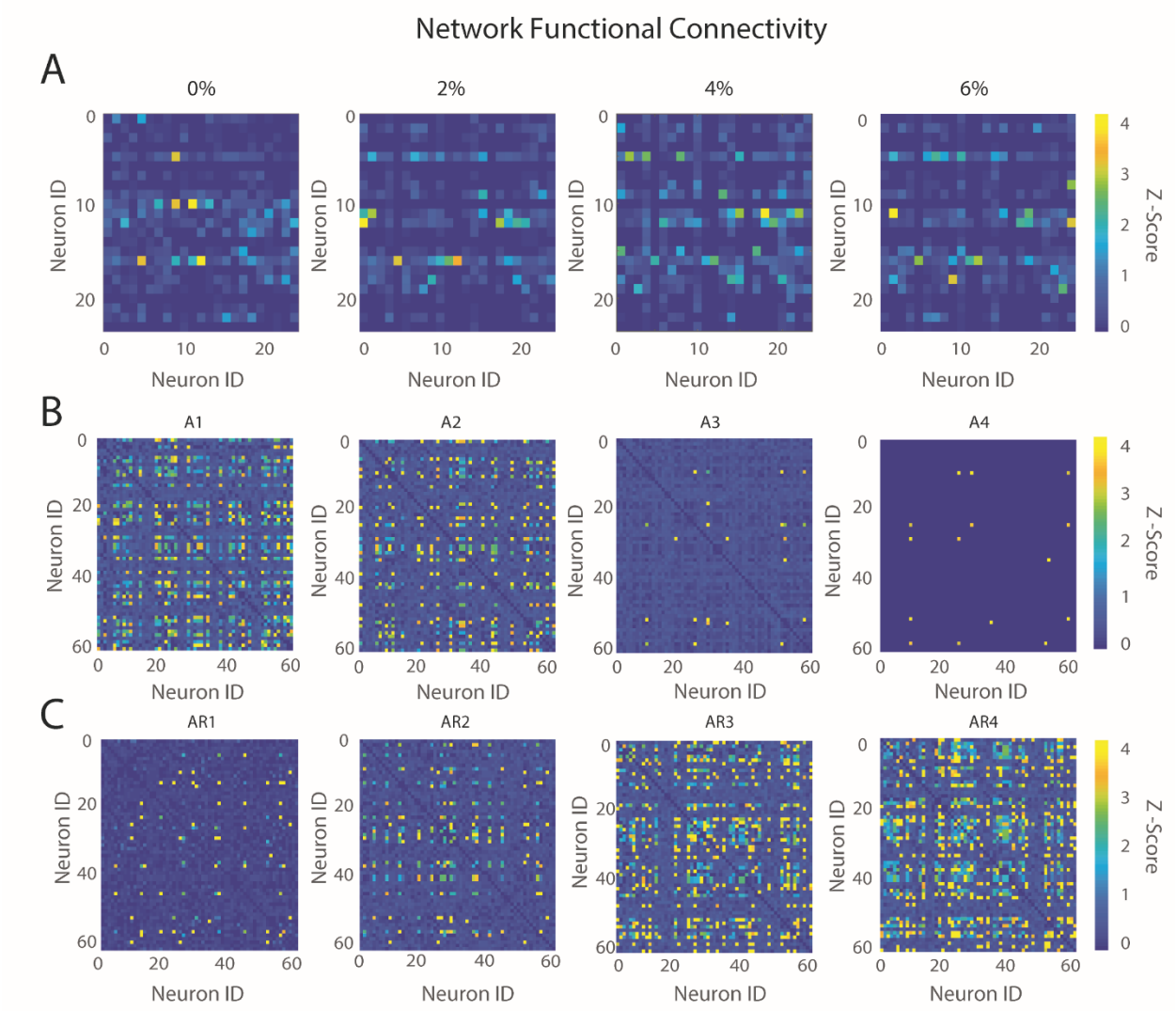

Supplementary Figure IV.S3. Functional Connectivity for Experiment and Simulated Anesthesia and Reversal

A) Example of experimental functional connectivity for 0%-6% anesthesia. Strong overlap can be seen in the significant connection found between 0% and 2% however similar connections are seen at all anesthetic levels B) Example A-Series functional connectivity. Higher connectivity is seen for A1 and decreases with increasing simulated anesthesia. Common connections between all anesthetic states can be observed. C) Example of AR Series functional connectivity. Low connectivity is seen for AR1 and increases with g_{Ks} reversal. Common connections between all anesthetic states can be observed. Single network/experiment shown in each case.

Bibliography

1. Abeles M, Gerstein GL. Detecting spatiotemporal firing patterns among simultaneously recorded single neurons. J Neurophysiol. 1988;60: 909–924. doi:10.1152/jn.1988.60.3.909

2. Churchland PS, Koch C, Sejnowski TJ. What is Computational Neuroscience? Computational Neuroscience. Cambridge, MA, USA: MIT Press; 1993. pp. 46–55.

3. Fan X, Markram H. A Brief History of Simulation Neuroscience. Front Neuroinform. 2019;13. doi:10.3389/fninf.2019.00032

4. Giménez C. [Composition and structure of the neuronal membrane: molecular basis of its physiology and pathology]. Rev Neurol. 1998;26: 232–239.

5. Pereda AE. Electrical synapses and their functional interactions with chemical synapses. Nat Rev Neurosci. 2014;15: 250–263. doi:10.1038/nrn3708

6. Yuste R. The discovery of dendritic spines by Cajal. Front Neuroanat. 2015;9: 18. doi:10.3389/fnana.2015.00018

7. Purves D, Augustine GJ, Fitzpatrick D, Hall WC, LaMantia A-S, McNamara JO, et al., editors. Neuroscience, 4th ed. Neuroscience, 4th ed. Sunderland, MA, US: Sinauer Associates; 2008.

8. Tamagawa H, Funatani M, Ikeda K. Ling's adsorption theory as a mechanism of membrane potential generation observed in both living and nonliving systems. Membranes (Basel). 2016;6. doi:10.3390/membranes6010011

9. Hodgkin AL, Huxley AF. A Quantitative Description of Membrain current and its application to conduction and excitation in nerve. J Physiol. 1952;117: 500–544. doi:10.1109/ICCCT2.2017.7972284

10. Pickard BG. Action potentials in higher plants. Bot Rev. 1973;39: 172–201. doi:10.1007/BF02859299

11. Sakmann B, Neher E. Patch clamp techniques for studying ionic channels in excitable membranes. Annu Rev Physiol. 1984;46: 455–472. doi:10.1146/annurev.ph.46.030184.002323

12. Häusser M. The Hodgkin-Huxley theory of the action potential. Nat Neurosci. 2000;3: 1165. doi:10.1038/81426

13. Catterall WA, Raman IM, Robinson HPC, Sejnowski TJ, Paulsen O. The Hodgkin-Huxley Heritage: From Channels to Circuits. J Neurosci. 2012;32: 14064–14073. doi:10.1523/JNEUROSCI.3403-12.2012

14. Lettvin JY, Maturana HR, McCulloch WS, Pitts WH. What the Frog's Eye Tells the Frog's Brain. Proc IRE. 1959;47: 1940–1951. doi:10.1109/JRPROC.1959.287207

15. Magee JC. Dendritic integration of excitatory synaptic input. Nat Rev Neurosci. 2000;1: 181–190. doi:10.1038/35044552

16. Poirazi P, Brannon T, Mel BW. Arithmetic of subthreshold synaptic summation in a model CA1 pyramidal cell. Neuron. 2003;37: 977–987. doi:10.1016/s0896-6273(03)00148-x

17. Rubinov M, Sporns O. Complex network measures of brain connectivity: uses and interpretations. Neuroimage. 2010;52: 1059–1069. doi:10.1016/j.neuroimage.2009.10.003

18. Renart A, Song P, Wang XJ. Robust spatial working memory through homeostatic synaptic scaling in heterogeneous cortical networks. Neuron. 2003;38: 473–485. doi:10.1016/S0896-6273(03)00255-1

19. Hebb DO. The organization of behavior; a neuropsychological theory. The organization of behavior; a neuropsychological theory. Oxford, England: Wiley; 1949.

20. Bi G, Poo M. Synaptic Modification by Correlated Activity: Hebb's Postulate Revisited. Annu Rev Neurosci. 2001;24: 139–166. doi:10.1146/annurev.neuro.24.1.139

21. Markram H, Lübke J, Frotscher M, Sakmann B. Regulation of Synaptic Efficacy by Coincidence of Postsynaptic APs and EPSPs. Science (80-). 1997;275: 213–215. doi:10.1126/science.275.5297.213

22. Bell CC, Han VZ, Sugawara Y, Grant K. Synaptic plasticity in a cerebellum-like structure depends on temporal order. Nature. 1997;387: 278–281. doi:10.1038/387278a0

23. von Bernhardi R, Bernhardi LE, Eugenín J. What Is Neural Plasticity? Adv Exp Med Biol. 2017;1015: 1–15. doi:10.1007/978-3-319-62817-2_1

24. Babaeeghazvini P, Rueda-Delgado LM, Gooijers J, Swinnen SP, Daffertshofer A. Brain Structural and Functional Connectivity: A Review of Combined Works of Diffusion Magnetic Resonance Imaging and Electro-Encephalography. Front Hum Neurosci. 2021;15: 721206. doi:10.3389/fnhum.2021.721206

25. Ainsworth M, Lee S, Cunningham MO, Traub RD, Kopell NJ, Whittington MA. Rates and Rhythms: A Synergistic View of Frequency and Temporal Coding in

Neuronal Networks. Neuron. 2012;75: 572–583. doi:10.1016/j.neuron.2012.08.004

26. Marder E. Neuromodulation of Neuronal Circuits: Back to the Future. Neuron. 2012;76: 1–11. doi:https://doi.org/10.1016/j.neuron.2012.09.010

27. Schnitzler A, Gross J. Normal and pathological oscillatory communication in the brain. Nat Rev Neurosci. 2005;6: 285–296. doi:10.1038/nrn1650

28. Bagherzadeh Y, Baldauf D, Pantazis D, Desimone R. Alpha Synchrony and the Neurofeedback Control of Spatial Attention. Neuron. 2020;105: 577-587.e5. doi:https://doi.org/10.1016/j.neuron.2019.11.001

29. Baldauf D, Desimone R. Neural mechanisms of object-based attention. Science. 2014;344: 424–427. doi:10.1126/science.1247003

30. Hughes JR. Gamma, fast, and ultrafast waves of the brain: their relationships with epilepsy and behavior. Epilepsy Behav. 2008;13: 25–31. doi:10.1016/j.yebeh.2008.01.011

31. Munk MHJ, Roelfsema PR, König P, Engel AK, Singer W. Role of Reticular Activation in the Modulation of Intracortical Synchronization. Science (80-). 1996;272: 271–274. doi:10.1126/science.272.5259.271

32. Herculano-Houzel S, Munk MHJ, Neuenschwander S, Singer W. Precisely Synchronized Oscillatory Firing Patterns Require Electroencephalographic Activation. J Neurosci. 1999;19: 3992–4010. doi:10.1523/JNEUROSCI.19-10-03992.1999

33. Buzsáki G, Draguhn A. Neuronal Oscillations in Cortical Networks. Science (80-). 2004;304: 1926–1929. doi:10.1126/science.1099745

34. Buzsáki G. “Neural Oscillation.” Encyclopedia Britannica. 2023.

35. Singer W. Neuronal synchrony: a versatile code for the definition of relations? Neuron. 1999;24: 49–65.

36. Varela F, Lachaux J-P, Rodriguez E, Martinerie J. The brainweb: Phase synchronization and large-scale integration. Nat Rev Neurosci. 2001;2: 229–239. doi:10.1038/35067550

37. Gray CM, Singer W. Stimulus-specific neuronal oscillations in orientation columns of cat visual cortex. Proc Natl Acad Sci U S A. 1989;86: 1698–1702. doi:10.1073/pnas.86.5.1698

38. Tallon-Baudry C, Bertrand O. Oscillatory gamma activity in humans and its role in object representation. Trends Cogn Sci. 1999;3: 151–162. doi:10.1016/s1364-6613(99)01299-1

39. Pesaran B, Pezaris JS, Sahani M, Mitra PP, Andersen RA. Temporal structure in neuronal activity during working memory in macaque parietal cortex. Nat Neurosci. 2002;5: 805–811. doi:10.1038/nn890

40. Izhikevich EM. Dynamical Systems in Neuroscience: The Geometry of Excitability and Bursting. The MIT Press; 2006. doi:10.7551/mitpress/2526.001.0001

41. Buzsáki G. Rhythms of the brain. Rhythms of the brain. New York, NY, US: Oxford University Press; 2006. doi:10.1093/acprof:oso/9780195301069.001.0001

42. Gansel KS. Neural synchrony in cortical networks: mechanisms and implications for neural information processing and coding. Front Integr Neurosci. 2022;16: 1–24. doi:10.3389/fnint.2022.900715

43. Tiesinga PHE, Fellous JM, José J V., Sejnowski TJ. Computational model of carbachol-induced delta, theta, and gamma oscillations in the hippocampus. Hippocampus. 2001;11: 251–274. doi:10.1002/hipo.1041

44. Fries P, Reynolds JH, Rorie AE, Desimone R. Modulation of Oscillatory Neuronal Synchronization by Selective Visual Attention. Science (80-). 2001;291: 1560–1563. doi:10.1126/science.1055465

45. Engel AK, Singer W. Temporal binding and the neural correlates of sensory awareness. Trends Cogn Sci. 2001;5: 16–25. doi:10.1016/s1364-6613(00)01568-0

46. Axmacher N, Mormann F, Fernández G, Elger CE, Fell J. Memory formation by neuronal synchronization. Brain Res Rev. 2006;52: 170–182. doi:10.1016/j.brainresrev.2006.01.007

47. Magee JC, Johnston D. A synaptically controlled, associative signal for Hebbian plasticity in hippocampal neurons. Science. 1997;275: 209–213. doi:10.1126/science.275.5297.209

48. Fortin DA, Levine ES. Differential Effects of Endocannabinoids on Glutamatergic and GABAergic Inputs to Layer 5 Pyramidal Neurons. Cereb Cortex. 2006;17: 163–174. doi:10.1093/cercor/bhj133

49. Hashimotodani Y, Ohno-Shosaku T, Kano M. Endocannabinoids and synaptic function in the CNS. Neurosci a Rev J bringing Neurobiol Neurol psychiatry. 2007;13: 127–137. doi:10.1177/1073858406296716

50. Conlay LA, Sabounjian LA, Wurtman RJ. Exercise and neuromodulators: choline and acetylcholine in marathon runners. Int J Sports Med. 1992;13 Suppl 1: S141-2. doi:10.1055/s-2007-1024619

51. Scheler G. Regulation of neuromodulator receptor efficacy—implications for whole-neuron and synaptic plasticity. Prog Neurobiol. 2004;72: 399–415.

doi:https://doi.org/10.1016/j.pneurobio.2004.03.008

52. Han JW, Ahn YD, Kim W-S, Shin CM, Jeong SJ, Song YS, et al. Psychiatric Manifestation in Patients with Parkinson's Disease. J Korean Med Sci. 2018;33: e300. doi:10.3346/jkms.2018.33.e300

53. Armstrong MJ, Okun MS. Diagnosis and Treatment of Parkinson Disease: A Review. JAMA. 2020;323: 548–560. doi:10.1001/jama.2019.22360

54. Vazquez J, Baghdoyan HA, Basal HAB, Baghdoyan HA. rapid communication Basal forebrain acetylcholine release during REM sleep is significantly greater than during waking. Am J Physiol Regul Integr Comp Physiol. 2001. Available: http://www.ajpregu.org

55. Szczypka MS, Rainey MA, Kim DS, Alaynick WA, Marck BT, Matsumoto AM, et al. Feeding behavior in dopamine-deficient mice. Proc Natl Acad Sci U S A. 1999;96: 12138–12143. doi:10.1073/pnas.96.21.12138

56. Berger M, Gray JA, Roth BL. The expanded biology of serotonin. Annu Rev Med. 2009;60: 355–366. doi:10.1146/annurev.med.60.042307.110802

57. Wimbiscus M, Kostenko O, Malone D. MAO inhibitors: risks, benefits, and lore. Cleve Clin J Med. 2010;77: 859–882. doi:10.3949/ccjm.77a.09103

58. O'Donnell J, Zeppenfeld D, McConnell E, Pena S, Nedergaard M. Norepinephrine: a neuromodulator that boosts the function of multiple cell types to optimize CNS performance. Neurochem Res. 2012;37: 2496–2512. doi:10.1007/s11064-012-0818-x

59. Sara SJ, Bouret S. Orienting and Reorienting: The Locus Coeruleus Mediates Cognition through Arousal. Neuron. 2012;76: 130–141. doi:https://doi.org/10.1016/j.neuron.2012.09.011

60. Picciotto MR, Higley MJ, Mineur YS. Acetylcholine as a neuromodulator: cholinergic signaling shapes nervous system function and behavior. Neuron. 2012;76: 116–129. doi:10.1016/j.neuron.2012.08.036

61. Myers RD, Waller MB. Differential release of acetylcholine from the hypothalamus and mesencephalon of the monkey during regulation. J Physiol. 1973;230: 273–293. doi:10.1113/jphysiol.1973.sp010188

62. Drevets WC. Neuroimaging studies of major depression. Advances in brain imaging. Arlington, VA, US: American Psychiatric Association; 2001. pp. 123–170.

63. Janowsky DS, el-Yousef MK, Davis JM, Sekerke HJ. A cholinergic-adrenergic hypothesis of mania and depression. Lancet (London, England). 1972;2: 632–635. doi:10.1016/s0140-6736(72)93021-8

64. Risch SC, Cohen RM, Janowsky DS, Kalin NH, Sitaram N, Christian Gillin J, et al. Physostigmine induction of depressive symptomatology in normal human subjects. Psychiatry Res. 1981;4: 89–94. doi:https://doi.org/10.1016/0165-1781(81)90012-3

65. Berger-Sweeney J, Stearns NA, Murg SL, Floerke-Nashner LR, Lappi DA, Baxter MG. Selective Immunolesions of Cholinergic Neurons in Mice: Effects on Neuroanatomy, Neurochemistry, and Behavior. J Neurosci. 2001;21: 8164–8173. doi:10.1523/JNEUROSCI.21-20-08164.2001

66. McQuiston AR. Acetylcholine release and inhibitory interneuron activity in hippocampal CA1. Front Synaptic Neurosci. 2014;6: 1–7. doi:10.3389/fnsyn.2014.00020

67. McKay BE, Placzek AN, Dani JA. Regulation of synaptic transmission and plasticity by neuronal nicotinic acetylcholine receptors. Biochem Pharmacol. 2007;74: 1120–1133. doi:10.1016/j.bcp.2007.07.001

68. Placzek AN, Zhang TA, Dani JA. Nicotinic mechanisms influencing synaptic plasticity in the hippocampus. Acta Pharmacol Sin. 2009;30: 752–760. doi:10.1038/aps.2009.39

69. Agmon A, Connors BW. Thalamocortical responses of mouse somatosensory (barrel) cortex in vitro. Neuroscience. 1991;41: 365–379. doi:10.1016/0306-4522(91)90333-j

70. Lambe EK, Picciotto MR, Aghajanian GK. Nicotine Induces Glutamate Release from Thalamocortical Terminals in Prefrontal Cortex. Neuropsychopharmacology. 2003;28: 216–225. doi:10.1038/sj.npp.1300032

71. Fernández de Sevilla D, Buño W. Presynaptic inhibition of Schaffer collateral synapses by stimulation of hippocampal cholinergic afferent fibres. Eur J Neurosci. 2003;17: 555–558. doi:10.1046/j.1460-9568.2003.02490.x

72. Barkai E, Hasselmo ME. Modulation of the input/output function of rat piriform cortex pyramidal cells. J Neurophysiol. 1994;72: 644–658. doi:10.1152/jn.1994.72.2.644

73. Groleau M, Chamoun M, Vaucher E. Stimulation of Acetylcholine Release and Pharmacological Potentiation of Cholinergic Transmission Affect Cholinergic Receptor Expression Differently during Visual Conditioning. Neuroscience. 2018;386: 79–90. doi:10.1016/j.neuroscience.2018.06.023

74. Marrion N V. CONTROL OF M-CURRENT. Annu Rev Physiol. 1997;59: 483–504. doi:10.1146/annurev.physiol.59.1.483

75. Prescott SA, Sejnowski TJ. Spike-rate coding and spike-time coding are affected oppositely by different adaptation mechanisms. J Neurosci. 2008;28: 13649–

13661. doi:10.1523/JNEUROSCI.1792-08.2008

76. Stiefel KM, Gutkin BS, Sejnowski TJ. Cholinergic neuromodulation changes phase response curve shape and type in cortical pyramidal neurons. PLoS One. 2008;3. doi:10.1371/journal.pone.0003947

77. Tsuno Y, Schultheiss NW, Hasselmo ME. In vivo cholinergic modulation of the cellular properties of medial entorhinal cortex neurons. J Physiol. 2013;591: 2611–2627. doi:10.1113/jphysiol.2012.250431

78. Izhikevich EM. Dynamical Systems in Neuroscience : The Geometry of Excitability and Bursting The MIT Press Chapter 4 Two-Dimensional Systems. 2005. Available: http://citeseerx.ist.psu.edu/viewdoc/download?doi=10.1.1.725.8216&rep=rep1&type=pdf

79. Börgers C. An Introduction to Modeling Neuronal Dynamics. 2017;66. doi:10.1007/978-3-319-51171-9

80. Gutkin BS, Ermentrout GB. Dynamics of Membrane Excitability Determine Interspike Interval Variability: A Link Between Spike Generation Mechanisms and Cortical Spike Train Statistics. Neural Comput. 1998;10: 1047–1065. doi:10.1162/089976698300017331

81. Gutkin B, Pinto D, Ermentrout B. Mathematical neuroscience: from neurons to circuits to systems. J Physiol. 2003;97: 209–219. doi:https://doi.org/10.1016/j.jphysparis.2003.09.005

82. Stiefel KM, Gutkin BS, Sejnowski TJ. Cholinergic neuromodulation changes phase response curve shape and type in cortical pyramidal neurons. PLoS One. 2008;3. doi:10.1371/journal.pone.0003947

83. Tang AC, Bartels AM, Sejnowski TJ. Effects of cholinergic modulation on responses of neocortical neurons to fluctuating input. Cereb Cortex. 1997;7: 502–509. doi:10.1093/cercor/7.6.502

84. Bogaard A, Parent J, Zochowski M, Booth V. Interaction of cellular and network mechanisms in spatiotemporal pattern formation in neuronal networks. J Neurosci. 2009;29: 1677–1687. doi:10.1523/JNEUROSCI.5218-08.2009

85. Fink CG, Booth V, Zochowski M. Cellularly-driven differences in network synchronization propensity are differentially modulated by firing frequency. PLoS Comput Biol. 2011;7. doi:10.1371/journal.pcbi.1002062

86. Prescott SA, Ratté S, De Koninck Y, Sejnowski TJ. Pyramidal neurons switch from integrators in vitro to resonators under in vivo-like conditions. J Neurophysiol. 2008;100: 3030–3042. doi:10.1152/jn.90634.2008

87. Roach JP, Ben-Jacob E, Sander LM, Zochowski MR. Formation and Dynamics of Waves in a Cortical Model of Cholinergic Modulation. PLoS Comput Biol. 2015;11. doi:10.1371/journal.pcbi.1004449

88. Knudstrup S, Zochowski M, Booth V. Network burst dynamics under heterogeneous cholinergic modulation of neural firing properties and heterogeneous synaptic connectivity. Eur J Neurosci. 2016;43: 1321–1339. doi:10.1111/ejn.13210

89. Mofakham S, Fink CG, Booth V, Zochowski MR. Interplay between excitability type and distributions of neuronal connectivity determines neuronal network synchronization. Phys Rev E. 2016;94: 42427. doi:10.1103/PhysRevE.94.042427

90. Von Der Malsburg C. The what and why of binding: The modeler's perspective. Neuron. 1999;24: 95–104. doi:10.1016/S0896-6273(00)80825-9

91. Theunissen F, Miller JP. Temporal encoding in nervous systems: A rigorous definition. J Comput Neurosci. 1995;2: 149–162. doi:10.1007/BF00961885

92. Hasselmo ME. The role of acetylcholine in learning and memory. Curr Opin Neurobiol. 2006;16: 710–715. doi:10.1016/j.conb.2006.09.002

93. Easton A, Douchamps V, Eacott M, Lever C. A specific role for septohippocampal acetylcholine in memory? Neuropsychologia. 2012;50: 3156–3168. doi:https://doi.org/10.1016/j.neuropsychologia.2012.07.022

94. Dutar P, Bassant M-H, Senut M-C, Lamour YBT-PR. The septohippocampal pathway: structure and function of a central cholinergic system. 1995;75: 393+. Available: https://link.gale.com/apps/doc/A16871743/AONE?u=googlescholar&sid=bookmark-AONE&xid=04f7e9d8

95. Newman EL, Gupta K, Climer JR, Monaghan CK, Hasselmo ME. Cholinergic modulation of cognitive processing: Insights drawn from computational models. Front Behav Neurosci. 2012;6: 1–19. doi:10.3389/fnbeh.2012.00024

96. Raza SA, Albrecht A, Çalışkan G, Müller B, Demiray YE, Ludewig S, et al. HIPP neurons in the dentate gyrus mediate the cholinergic modulation of background context memory salience. Nat Commun. 2017;8: 189. doi:10.1038/s41467-017-00205-3

97. Lovett-Barron M, Kaifosh P, Kheirbek MA, Danielson N, Zaremba JD, Reardon TR, et al. Dendritic inhibition in the hippocampus supports fear learning. Science. 2014;343: 857–863. doi:10.1126/science.1247485

98. Nichol H, Amilhon B, Manseau F, Badrinarayanan S, Williams S. Electrophysiological and Morphological Characterization of Chrna2 Cells in the Subiculum and CA1 of the Hippocampus: An Optogenetic Investigation. Front Cell

Neurosci. 2018;12. doi:10.3389/fncel.2018.00032

99. Jia Y, Yamazaki Y, Nakauchi S, Ito K-I, Sumikawa K. Nicotine facilitates long-term potentiation induction in oriens-lacunosum moleculare cells via Ca2+ entry through non-α7 nicotinic acetylcholine receptors. Eur J Neurosci. 2010;31: 463–476. doi:https://doi.org/10.1111/j.1460-9568.2009.07058.x

100. Kametani H, Kawamura H. Alterations in acetylcholine release in the rat hippocampus during sleep-wakefulness detected by intracerebral dialysis. Life Sci. 1990;47: 421–426. doi:https://doi.org/10.1016/0024-3205(90)90300-G

101. Ruivo L, Baker K, Conway M, Kinsley P, Gilmour G, Phillips K, et al. Coordinated Acetylcholine Release in Prefrontal Cortex and Hippocampus Is Associated with Arousal and Reward on Distinct Timescales. Cell Rep. 2017;18: 905–917. doi:10.1016/j.celrep.2016.12.085

102. Delorme J, Wang L, Kuhn FR, Kodoth V, Ma J, Martinez JD, et al. Sleep loss drives acetylcholine- and somatostatin interneuron–mediated gating of hippocampal activity to inhibit memory consolidation. Proc Natl Acad Sci. 2021;118: e2019318118. doi:10.1073/pnas.2019318118

103. Rogers JL, Kesner RP. Cholinergic modulation of the hippocampus during encoding and retrieval of tone/shock-induced fear conditioning. Learn Mem. 2004;11: 102–107. doi:10.1101/lm.64604

104. Rogers JL, Kesner RP. Cholinergic modulation of the hippocampus during encoding and retrieval. Neurobiol Learn Mem. 2003;80: 332–342. doi:10.1016/s1074-7427(03)00063-7

105. Rasch BH, Born J, Gais S. Combined blockade of cholinergic receptors shifts the brain from stimulus encoding to memory consolidation. J Cogn Neurosci. 2006;18: 793–802. doi:10.1162/jocn.2006.18.5.793

106. Pace-Schott E, Stickgold R, Hobson J. Dreaming and the Brain: Toward a Cognitive Neuroscience of Conscious States. Behav Brain Sci. 1970;23. doi:10.1017/S0140525X00003976

107. Watson CJ, Baghdoyan HA, Lydic R. Neuropharmacology of sleep and wakefulness. Sleep Medicine Clinics. 2010. pp. 513–528. doi:10.1016/j.jsmc.2010.08.003

108. Gandhi MH, Emmady PD. Physiology, K Complex. In: StatPearls [Internet]. Treasure Island (FL): StatPearls; Jan 2022. Available: https://www.ncbi.nlm.nih.gov/books/NBK557469/

109. McGinty DJ, Sterman MB. Sleep suppression after basal forebrain lesions in the cat. Science. 1968;160: 1253–1255. doi:10.1126/science.160.3833.1253

110. Prince T-M, Wimmer M, Choi J, Havekes R, Aton S, Abel T. Sleep deprivation during a specific 3-hour time window post-training impairs hippocampal synaptic plasticity and memory. Neurobiol Learn Mem. 2014;109: 122–130. doi:10.1016/j.nlm.2013.11.021

111. Patel AK, Reddy V, Shumway KR, Araujo JF. Physiology, Sleep Stages. Treasure Island (FL): StatPearls; 2022. Available: https://www.ncbi.nlm.nih.gov/books/NBK526132/

112. Nissen C, Nofzinger EA, Feige B, Waldheim B, Radosa M-P, Riemann D, et al. Differential Effects of the Muscarinic M1 Receptor Agonist RS-86 and the Acetylcholine-Esterase Inhibitor Donepezil on REM Sleep Regulation in Healthy Volunteers. Neuropsychopharmacology. 2006;31: 1294–1300. doi:10.1038/sj.npp.1300906

113. Girardeau G, Benchenane K, Wiener SI, Buzsáki G, Zugaro MB. Selective suppression of hippocampal ripples impairs spatial memory. Nat Neurosci. 2009;12: 1222–1223. doi:10.1038/nn.2384

114. Puentes-Mestril C, Roach J, Niethard N, Zochowski M, Aton SJ. How rhythms of the sleeping brain tune memory and synaptic plasticity. Sleep. 2019;42: 1–14. doi:10.1093/sleep/zsz095

115. Ognjanovski N, Maruyama D, Lashner N, Zochowski M, Aton SJ. CA1 hippocampal network activity changes during sleep-dependent memory consolidation. Front Syst Neurosci. 2014;8: 1–11. doi:10.3389/fnsys.2014.00061

116. Zhang H, Lin SC, Nicolelis MAL. Spatiotemporal coupling between hippocampal acetylcholine release and theta oscillations in vivo. J Neurosci. 2010;30: 13431–13440. doi:10.1523/JNEUROSCI.1144-10.2010

117. Nagode DA, Tang A-H, Yang K, Alger BE. Optogenetic identification of an intrinsic cholinergically driven inhibitory oscillator sensitive to cannabinoids and opioids in hippocampal CA1. J Physiol. 2014;592: 103–123. doi:10.1113/jphysiol.2013.257428

118. Shinoe T, Matsui M, Taketo MM, Manabe T. Modulation of synaptic plasticity by physiological activation of M1 muscarinic acetylcholine receptors in the mouse hippocampus. J Neurosci Off J Soc Neurosci. 2005;25: 11194–11200. doi:10.1523/JNEUROSCI.2338-05.2005

119. Feldman DE. The Spike-Timing Dependence of Plasticity. Neuron. 2012;75: 556–571. doi:10.1016/j.neuron.2012.08.001

120. Hübener M, Bonhoeffer T. Searching for Engrams. Neuron. 2010;67: 363–371. doi:10.1016/j.neuron.2010.06.033

121. Baeg EH, Kim YB, Kim J, Ghim JW, Kim JJ, Jung MW. Learning-induced

enduring changes in functional connectivity among prefrontal cortical neurons. J Neurosci. 2007;27: 909–918. doi:10.1523/JNEUROSCI.4759-06.2007

122. Clawson BC, Pickup EJ, Ensing A, Geneseo L, Shaver J, Gonzalez-Amoretti J, et al. Causal role for sleep-dependent reactivation of learning-activated sensory ensembles for fear memory consolidation. Nat Commun. 2021;12: 1–13. doi:10.1038/s41467-021-21471-2

123. Levenstein D, Watson BO, Rinzel J, Buzsáki G. Sleep regulation of the distribution of cortical firing rates. Curr Opin Neurobiol. 2017;44: 34–42. doi:10.1016/j.conb.2017.02.013

124. Clawson BC, Durkin J, Suresh AK, Pickup EJ, Broussard CG, Aton SJ. Sleep promotes, and sleep loss inhibits, selective changes in firing rate, response properties and functional connectivity of primary visual cortex neurons. Front Syst Neurosci. 2018;12: 1–16. doi:10.3389/fnsys.2018.00040

125. Ryan TJ, Roy DS, Pignatelli M, Arons A, Tonegawa S. Engram cells retain memory under retrograde amnesia. Science (80-). 2015;348: 1007–1013. doi:10.1126/science.aaa5542

126. Bachatene L, Bharmauria V, Cattan S, Chanauria N, Rouat J, Molotchnikoff S. Summation of connectivity strengths in the visual cortex reveals stability of neuronal microcircuits after plasticity. BMC Neurosci. 2015;16: 1–11. doi:10.1186/s12868-015-0203-1

127. Girardeau G, Inema I, Buzsáki G. Reactivations of emotional memory in the hippocampus-amygdala system during sleep. Nat Neurosci. 2017;20: 1634–1642. doi:10.1038/nn.4637

128. Roach JP, Pidde A, Katz E, Wu J, Ognjanovski N, Aton SJ, et al. Resonance with subthreshold oscillatory drive organizes activity and optimizes learning in neural networks. Proc Natl Acad Sci U S A. 2018;115: E3017–E3025. doi:10.1073/pnas.1716933115

129. Xia F, Richards BA, Tran MM, Josselyn SA, Takehara-Nishiuchi K, Frankland PW. Parvalbumin-positive interneurons mediate neocortical-hippocampal interactions that are necessary for memory consolidation. Elife. 2017;6: 1–25. doi:10.7554/eLife.27868

130. Durkin J, Suresh AK, Colbath J, Broussard C, Wu J, Zochowski M, et al. Cortically coordinated NREM thalamocortical oscillations play an essential, instructive role in visual system plasticity. Proc Natl Acad Sci U S A. 2017;114: 10485–10490. doi:10.1073/pnas.1710613114

131. Ognjanovski N, Broussard C, Zochowski M, Aton SJ. Hippocampal network oscillations rescue memory consolidation deficits caused by sleep loss. Cereb Cortex. 2018;28: 3711–3723. doi:10.1093/cercor/bhy174

132. Alkire MT, Miller J. General anesthesia and the neural correlates of consciousness. Prog Brain Res. 2005;150: 229–244. doi:10.1016/S0079-6123(05)50017-7

133. Schwartz RS, Brown EN, Lydic R, Schiff ND. Mechanisms of Disease General Anesthesia, Sleep, and Coma. N Engl J Med. 2010;363: 2638–50. doi:10.1056/NEJMra0808281

134. Mashour GA, Hudetz AG. Neural Correlates of Unconsciousness in Large-Scale Brain Networks. Trends Neurosci. 2018;41: 150–160. doi:10.1016/j.tins.2018.01.003

135. Franks NP. General anaesthesia: From molecular targets to neuronal pathways of sleep and arousal. Nat Rev Neurosci. 2008;9: 370–386. doi:10.1038/nrn2372

136. Liang Z, Huang C, Li Y, Hight DF, Voss LJ, Sleigh JW, et al. Emergence EEG pattern classification in sevoflurane anesthesia. Physiol Meas. 2018;39. doi:10.1088/1361-6579/aab4d0

137. Taub AH, Katz Y, Lampl I. Cortical balance of excitation and inhibition is regulated by the rate of synaptic activity. J Neurosci. 2013;33: 14359–14368. doi:10.1523/JNEUROSCI.1748-13.2013

138. Alkire MT, Hudetz AG, Tononi G. Consciousness and anesthesia. Science (80-). 2008;322: 876–880. doi:10.1126/science.1149213

139. Vizuete JA, Pillay S, Diba K, Ropella KM, Hudetz AG. Monosynaptic functional connectivity in cerebral cortex during wakefulness and under graded levels of anesthesia. Front Integr Neurosci. 2012;6: 90. doi:10.3389/fnint.2012.00090

140. Tononi G, Boly M, Massimini M, Koch C. Integrated information theory: From consciousness to its physical substrate. Nat Rev Neurosci. 2016;17: 450–461. doi:10.1038/nrn.2016.44

141. Hudetz AG. General Anesthesia and Human Brain Connectivity. Brain Connect. 2012;2: 291–302. doi:10.1089/brain.2012.0107

142. Pal D, Mashour GA. Consciousness, Anesthesia, and Acetylcholine. Anesthesiology. 2021;134: 515–517. doi:10.1097/ALN.0000000000003696

143. Luo T-Y, Cai S, Qin Z-X, Yang S-C, Shu Y, Liu C-X, et al. Basal Forebrain Cholinergic Activity Modulates Isoflurane and Propofol Anesthesia. Front Neurosci. 2020;14: 559077. doi:10.3389/fnins.2020.559077

144. Reed SJ, Plourde G, Tobin S, Chapman CA. Partial antagonism of propofol anaesthesia by physostigmine in rats is associated with potentiation of fast (80-200 Hz) oscillations in the thalamus. Br J Anaesth. 2013;110: 646–653. doi:10.1093/bja/aes432

145. Solt K, Van Dort CJ, Chemali JJ, Taylor NE, Kenny JD, Brown EN. Electrical stimulation of the ventral Tegmental area induces reanimation from general anesthesia. Anesthesiology. 2014;121: 311–319. doi:10.1097/ALN.0000000000000117

146. Guidera JA, Taylor NE, Lee JT, Vlasov KY, Pei JZ, Stephen EP, et al. Sevoflurane induces coherent slow-delta oscillations in rats. Front Neural Circuits. 2017;11. doi:10.3389/fncir.2017.00036

147. Markram H, Muller E, Ramaswamy S, Reimann MW, Abdellah M, Sanchez CA, et al. Reconstruction and Simulation of Neocortical Microcircuitry. Cell. 2015;163: 456–492. doi:10.1016/j.cell.2015.09.029

148. Alkire MT, McReynolds JR, Hahn EL, Trivedi AN. Thalamic microinjection of nicotine reverses sevoflurane-induced loss of righting reflex in the rat. Anesthesiology. 2007;107: 264–272. doi:10.1097/01.anes.0000270741.33766.24

149. Hudetz AG, Wood JD, Kampine JP. Cholinergic Reversal of Isoflurane Anesthesia in Rats as Measured by Cross-approximate Entropy of the Electroencephalogram. Anesthesiology. 2003;99: 1125–1131. doi:10.1097/00000542-200311000-00019

150. Pal D, Dean JG, Liu T, Li D, Watson CJ, Hudetz AG, et al. Differential Role of Prefrontal and Parietal Cortices in Controlling Level of Consciousness. Curr Biol. 2018;28: 2145-2152.e5. doi:10.1016/j.cub.2018.05.025

151. Barbero-Castillo A, Mateos-Aparicio P, Porta LD, Camassa A, Perez-Mendez L, Sanchez-Vives M V. Impact of gabaa and gabab inhibition on cortical dynamics and perturbational complexity during synchronous and desynchronized states. J Neurosci. 2021;41: 5029–5044. doi:10.1523/JNEUROSCI.1837-20.2021

152. Joo DT, Gong D, Sonner JM, Jia Z, Macdonald JF, Eger EI, et al. Blockade of AMPA Receptors and Volatile Anesthetics Reduced Anesthetic Requirements in GluR2 Null Mutant Mice for Loss of the Righting Reflex and Antinociception but Not Minimum Alveolar Concentration. Anesthesiology. 2001. doi:10.1097/00000542-200103000-00020

153. Rudolph U, Antkowiak B. Molecular and neuronal substrates for general anaesthetics. Nat Rev Neurosci. 2004;5: 709–720. doi:10.1038/nrn1496

154. Mapelli J, Gandolfi D, Giuliani E, Casali S, Congi L, Barbieri A, et al. The effects of the general anesthetic sevoflurane on neurotransmission: an experimental and computational study. Sci Rep. 2021;11: 1–17. doi:10.1038/s41598-021-83714-y

155. Mapelli J, Gandolfi D, Giuliani E, Prencipe FP, Pellati F, Barbieri A, et al. The effect of desflurane on neuronal communication at a central synapse. PLoS One. 2015;10. doi:10.1371/journal.pone.0123534

156. Fink CG, Murphy GG, Zochowski M, Booth V. A Dynamical Role for Acetylcholine

in Synaptic Renormalization. PLoS Comput Biol. 2013;9. doi:10.1371/journal.pcbi.1002939

157. Roach JP, Eniwaye B, Booth V, Sander LM, Zochowski MR. Acetylcholine Mediates Dynamic Switching Between Information Coding Schemes in Neuronal Networks. Front Syst Neurosci. 2019;13. doi:10.3389/fnsys.2019.00064

158. Stiefel KM, Gutkin BS, Sejnowski TJ. The effects of cholinergic neuromodulation on neuronal phase-response curves of modeled cortical neurons. J Comput Neurosci. 2009;26: 289–301. doi:10.1007/s10827-008-0111-9

159. Watts DJ, Strogatz SH. Collective dynamics of 'small-world' networks. Nature. 1998;393: 440–442. doi:10.1038/30918

160. Hsieh CY, Cruikshank SJ, Metherate R. Differential modulation of auditory thalamocortical and intracortical synaptic transmission by cholinergic agonist. Brain Res. 2000;880: 51–64. doi:10.1016/S0006-8993(00)02766-9

161. Osipov G V, Sushchik MM. Synchronized clusters and multistability in arrays of oscillators with different natural frequencies. Phys Rev E. 1998;58: 7198–7207. doi:10.1103/PhysRevE.58.7198

162. Acebrón JA, Bonilla LL, Vicente CJP, Ritort F, Spigler R. The Kuramoto model: A simple paradigm for synchronization phenomena. Rev Mod Phys. 2005;77: 137–185. doi:10.1103/RevModPhys.77.137

163. Favaretto C, Cenedese A, Pasqualetti F. Cluster Synchronization in Networks of Kuramoto Oscillators. IFAC-PapersOnLine. 2017;50: 2433–2438. doi:10.1016/j.ifacol.2017.08.405

164. Ratté S, Hong S, DeSchutter E, Prescott SA. Impact of neuronal properties on network coding: Roles of spike initiation dynamics and robust synchrony transfer. Neuron. 2013;78: 758–772. doi:10.1016/j.neuron.2013.05.030

165. Gjorgjieva J, Mease RA, Moody WJ, Fairhall AL. Intrinsic Neuronal Properties Switch the Mode of Information Transmission in Networks. PLoS Comput Biol. 2014;10. doi:10.1371/journal.pcbi.1003962

166. Atiani S, Elhilali M, David S V., Fritz JB, Shamma SA. Task Difficulty and Performance Induce Diverse Adaptive Patterns in Gain and Shape of Primary Auditory Cortical Receptive Fields. Neuron. 2009;61: 467–480. doi:10.1016/j.neuron.2008.12.027

167. Williamson RS, Ahrens MB, Linden JF, Sahani M. Input-Specific Gain Modulation by Local Sensory Context Shapes Cortical and Thalamic Responses to Complex Sounds. Neuron. 2016;91: 467–481. doi:10.1016/j.neuron.2016.05.041

168. Angeloni C, Geffen MN. Contextual modulation of sound processing in the

auditory cortex. Curr Opin Neurobiol. 2018;49: 8–15. doi:10.1016/j.conb.2017.10.012

169. Chance FS, Abbott LF, Reyes AD. Gain modulation from background synaptic input. Neuron. 2002;35: 773–782. doi:10.1016/S0896-6273(02)00820-6

170. Cardin JA, Palmer LA, Contreras D. Cellular Mechanisms Underlying Stimulus-Dependent Gain Modulation in Primary Visual Cortex Neurons In Vivo. Neuron. 2008;59: 150–160. doi:10.1016/j.neuron.2008.05.002

171. Carvalho TP, Buonomano D V. Differential Effects of Excitatory and Inhibitory Plasticity on Synaptically Driven Neuronal Input-Output Functions. Neuron. 2009;61: 774–785. doi:10.1016/j.neuron.2009.01.013

172. Soma S, Shimegi S, Osaki H, Sato H. Cholinergic modulation of response gain in the primary visual cortex of the macaque. J Neurophysiol. 2012;107: 283–291. doi:10.1152/jn.00330.2011

173. Soma S, Shimegi S, Suematsu N, Sato H. Cholinergic modulation of response gain in the rat primary visual cortex. Sci Rep. 2013;3: 1–7. doi:10.1038/srep01138

174. Himmelheber AM, Sarter M, Bruno JP. Increases in cortical acetylcholine release during sustained attention performance in rats. Cogn Brain Res. 2000;9: 313–325. doi:10.1016/S0926-6410(00)00012-4

175. Kozak R, Martinez V, Young D, Brown H, Bruno JP, Sarter M. Toward a neuro-cognitive animal model of the cognitive symptoms of schizophrenia: Disruption of cortical cholinergic neurotransmission following repeated amphetamine exposure in attentional task-performing, but not non-performing, rats. Neuropsychopharmacology. 2007;32: 2074–2086. doi:10.1038/sj.npp.1301352

176. Parikh V, Kozak R, Martinez V, Sarter M. Prefrontal Acetylcholine Release Controls Cue Detection on Multiple Timescales. Neuron. 2007;56: 141–154. doi:10.1016/j.neuron.2007.08.025

177. Vertes RP, Kocsis B. Brainstem-diencephalo-septohippocampal systems controlling the theta rhythm of the hippocampus. Neuroscience. 1997;81: 893–926.

178. Alger BE, Nagode DA, Tang AH. Muscarinic cholinergic receptors modulate inhibitory synaptic rhythms in hippocampus and neocortex. Front Synaptic Neurosci. 2014;6: 1–23. doi:10.3389/fnsyn.2014.00018

179. Wittenberg GM, Wang SSH. Malleability of spike-timing-dependent plasticity at the CA3-CA1 synapse. J Neurosci. 2006;26: 6610–6617. doi:10.1523/JNEUROSCI.5388-05.2006

180. Seol GH, Ziburkus J, Huang SY, Song L, Kim IT, Takamiya K, et al.

Neuromodulators Control the Polarity of Spike-Timing-Dependent Synaptic Plasticity. Neuron. 2007;55: 919–929. doi:10.1016/j.neuron.2007.08.013

181. Marrosu F, Portas C, Mascia MS, Casu MA, Fà M, Giagheddu M, et al. Microdialysis measurement of cortical and hippocampal acetylcholine release during sleep-wake cycle in freely moving cats. Brain Res. 1995;671: 329–332. doi:10.1016/0006-8993(94)01399-3

182. Miyawaki H, Watson BO, Diba K. Neuronal firing rates diverge during REM and homogenize during non-REM. Sci Rep. 2019;9: 1–14. doi:10.1038/s41598-018-36710-8

183. Tononi G, Cirelli C. Sleep and the Price of Plasticity: From Synaptic and Cellular Homeostasis to Memory Consolidation and Integration. Neuron. 2014;81: 12–34. doi:10.1016/j.neuron.2013.12.025

184. Mizuseki K, Sirota A, Pastalkova E, Buzsáki G. Theta Oscillations Provide Temporal Windows for Local Circuit Computation in the Entorhinal-Hippocampal Loop. Neuron. 2009;64: 267–280. doi:10.1016/j.neuron.2009.08.037

185. Mizuseki K, Buzsáki G. Preconfigured, skewed distribution of firing rates in the hippocampus and entorhinal cortex. Cell Rep. 2013;4: 1010–1021. doi:10.1016/j.celrep.2013.07.039

186. Sarter M, Lustig C, Howe WM, Gritton H, Berry AS. Deterministic functions of cortical acetylcholine. Eur J Neurosci. 2014;39: 1912–1920. doi:https://doi.org/10.1111/ejn.12515

187. Skilling QM, Eniwaye B, Clawson BC, Shaver J, Ognjanovski N, Aton SJ, et al. Acetylcholine-gated current translates wake neuronal firing rate information into a spike timing-based code in Non-REM sleep, stabilizing neural network dynamics during memory consolidation. PLOS Comput Biol. 2021;17: e1009424. Available: https://doi.org/10.1371/journal.pcbi.1009424

188. Aton SJ, Broussard C, Dumoulin M, Seibt J, Watson A, Coleman T, et al. Visual experience and subsequent sleep induce sequential plastic changes in putative inhibitory and excitatory cortical neurons. Proc Natl Acad Sci U S A. 2013;110: 3101–3106. doi:10.1073/pnas.1208093110

189. Prince TM, Wimmer M, Choi J, Havekes R, Aton S, Abel T. Sleep deprivation during a specific 3-hour time window post-training impairs hippocampal synaptic plasticity and memory. Neurobiol Learn Mem. 2014;109: 122–130. doi:10.1016/j.nlm.2013.11.021

190. Graves LA, Heller EA, Pack AI, Abel T. Sleep deprivation selectively impairs memory consolidation for contextual fear conditioning. Learn Mem. 2003;10: 168–176. doi:10.1101/lm.48803

191. Ognjanovski N, Schaeffer S, Wu J, Mofakham S, Maruyama D, Zochowski M, et al. Parvalbumin-expressing interneurons coordinate hippocampal network dynamics required for memory consolidation. Nat Commun. 2017;8. doi:10.1038/ncomms15039

192. Durkin J, Aton SJ. Sleep-dependent potentiation in the visual system is at odds with the synaptic homeostasis hypothesis. Sleep. 2016;39: 155–159. doi:10.5665/sleep.5338

193. Feldt S, Waddell J, Hetrick VL, Berke JD, Zochowski M. Functional clustering algorithm for the analysis of dynamic network data. Phys Rev E - Stat Nonlinear, Soft Matter Phys. 2009;79: 1–20. doi:10.1103/PhysRevE.79.056104

194. Wu J, Skilling QM, Maruyama D, Li C, Ognjanovski N, Aton S, et al. Functional network stability and average minimal distance – A framework to rapidly assess dynamics of functional network representations. J Neurosci Methods. 2018;296: 69–83. doi:10.1016/j.jneumeth.2017.12.021

195. Tronson NC, Schrick C, Guzman YF, Huh KH, Srivastava DP, Penzes P, et al. Segregated populations of hippocampal principal CA1 neurons mediating conditioning and extinction of contextual fear. J Neurosci. 2009;29: 3387–3394. doi:10.1523/JNEUROSCI.5619-08.2009

196. Daumas S, Halley H, Francés B, Lassalle JM. Encoding, consolidation, and retrieval of contextual memory: Differential involvement of dorsal CA3 and CA1 hippocampal subregions. Learn Mem. 2005;12: 375–382. doi:10.1101/lm.81905

197. Jones BE. From waking to sleeping: Neuronal and chemical substrates. Trends Pharmacol Sci. 2005;26: 578–586. doi:10.1016/j.tips.2005.09.009

198. Dasari S, Gulledge AT. M1 and M4 receptors modulate hippocampal pyramidal neurons. J Neurophysiol. 2011;105: 779–792. doi:10.1152/jn.00686.2010

199. Gutkin BS, Ermentrout GB, Reyes AD. Phase-response curves give the responses of neurons to transient inputs. J Neurophysiol. 2005;94: 1623–1635. doi:10.1152/jn.00359.2004

200. Kang YJ, Lewis HES, Young MW, Govindaiah G, Greenfield LJ, Garcia-Rill E, et al. Cell Type-specific Intrinsic Perithreshold Oscillations in Hippocampal GABAergic Interneurons. Neuroscience. 2018;376: 80–93. doi:10.1016/j.neuroscience.2018.02.014

201. Yang S, Yang S, Moreira T, Hoffman G, Carlson GC, Bender KJ, et al. Interlamellar CA1 network in the hippocampus. Proc Natl Acad Sci U S A. 2014;111: 12919–12924. doi:10.1073/pnas.1405468111

202. Pikovsky A, Rosenblum M, Kurths J. Synchronization - A Universal Concept in Nonlinear Sciences. Cambridge Nonlinear Science Series. 2001.

203. Skilling QM, Ognjanovski N, Aton SJ, Zochowski M. Critical dynamics mediate learning of new distributed memory representations in neuronal networks. Entropy. 2019;21. doi:10.3390/e21111043

204. Watson BO, Levenstein D, Greene JP, Gelinas JN, Buzsáki G. Network Homeostasis and State Dynamics of Neocortical Sleep. Neuron. 2016;90: 839–852. doi:10.1016/j.neuron.2016.03.036

205. Smeal RM, Bard Ermentrout G, White JA. Phase-response curves and synchronized neural networks. Philos Trans R Soc B Biol Sci. 2010;365: 2407–2422. doi:10.1098/rstb.2009.0292

206. Bi G, Poo M. Synaptic Modifications in Cultured Hippocampal Neurons: Dependence on Spike Timing, Synaptic Strength, and Postsynaptic Cell Type. J Neurosci. 1998;18: 10464–10472. doi:10.1523/JNEUROSCI.18-24-10464.1998

207. Puentes-Mestril C, Aton SJ. Linking Network Activity to Synaptic Plasticity during Sleep: Hypotheses and Recent Data. Front Neural Circuits. 2017;11. doi:10.3389/fncir.2017.00061

208. Antony JW, Schönauer M, Staresina BP, Cairney SA. Sleep Spindles and Memory Reprocessing. Trends Neurosci. 2019;42: 1–3. doi:https://doi.org/10.1016/j.tins.2018.09.012

209. Ognjanovski N, Broussard C, Zochowski M, Aton SJ. Hippocampal network oscillations rescue memory consolidation deficits caused by sleep loss. Cereb Cortex. 2018;28: 3711–3723. doi:10.1093/cercor/bhy174

210. Gava GP, McHugh SB, Lefèvre L, Lopes-dos-Santos V, Trouche S, El-Gaby M, et al. Integrating new memories into the hippocampal network activity space. Nat Neurosci. 2021;24: 326–330. doi:10.1038/s41593-021-00804-w

211. Peyrache A, Benchenane K, Khamassi M, Wiener SI, Battaglia FP. Sequential reinstatement of neocortical activity during slow oscillations depends on cells' global activity. Front Syst Neurosci. 2010;3: 1–7. doi:10.3389/neuro.06.018.2009

212. Grosmark AD, Buzsáki G. Diversity in neural firing dynamics supports both rigid and learned hippocampal sequences. Science. 2016;351: 1440–1443. doi:10.1126/science.aad1935

213. Cheng S, Frank LM. New Experiences Enhance Coordinated Neural Activity in the Hippocampus. Neuron. 2008;57: 303–313. doi:10.1016/j.neuron.2007.11.035

214. Buzsáki G, Wang X-J. Mechanisms of gamma oscillations. Annu Rev Neurosci. 2012;35: 203–225. doi:10.1146/annurev-neuro-062111-150444

215. Lee SH, Dan Y. Neuromodulation of Brain States. Neuron. 2012;76: 209–222. doi:10.1016/j.neuron.2012.09.012

216. Bjorness TE, Greene RW. Adenosine and sleep. Curr Neuropharmacol. 2009;7: 238–245. doi:10.2174/157015909789152182

217. Pape HC. Adenosine promotes burst activity in guinea-pig geniculocortical neurones through two different ionic mechanisms. J Physiol. 1992;447: 729–753. doi:10.1113/jphysiol.1992.sp019026

218. Durkin J, Suresh AK, Colbath J, Broussard C, Wu J, Zochowski M, et al. Cortically coordinated NREM thalamocortical oscillations play an essential, instructive role in visual system plasticity. Proc Natl Acad Sci U S A. 2017;114: 10485–10490. doi:10.1073/pnas.1710613114

219. Carr MF, Jadhav SP, Frank LM. Hippocampal replay in the awake state: a potential substrate for memory consolidation and retrieval. Nat Neurosci. 2011;14: 147–153. doi:10.1038/nn.2732

220. Vaz AP, Wittig JHJ, Inati SK, Zaghloul KA. Replay of cortical spiking sequences during human memory retrieval. Science. 2020;367: 1131–1134. doi:10.1126/science.aba0672

221. Davidson TJ, Kloosterman F, Wilson MA. Hippocampal replay of extended experience. Neuron. 2009;63: 497–507. doi:10.1016/j.neuron.2009.07.027

222. Eniwaye BP, Booth V, Hudetz AG, Zochowski M. Modeling cortical synaptic effects of anesthesia and their cholinergic reversal. PLOS Comput Biol. 2022;18: e1009743. Available: https://doi.org/10.1371/journal.pcbi.1009743

223. Hudetz AG, Vizuete JA, Pillay S, Ropella KM. Critical Changes in Cortical Neuronal Interactions in Anesthetized and Awake Rats. Anesthesiology. 2015;123: 171–180. doi:10.1097/ALN.0000000000000690

224. Vizuete JA, Pillay S, Ropella KM, Hudetz AG. Graded defragmentation of cortical neuronal firing during recovery of consciousness in rats. Neuroscience. 2014. doi:10.1016/j.neuroscience.2014.06.018

225. Ferron J-F, Kroeger D, Chever O, Amzica F. Cortical inhibition during burst suppression induced with isoflurane anesthesia. J Neurosci. 2009;29: 9850–9860. doi:10.1523/JNEUROSCI.5176-08.2009

226. Rich S, Zochowski M, Booth V. Effects of Neuromodulation on Excitatory–Inhibitory Neural Network Dynamics Depend on Network Connectivity Structure. J Nonlinear Sci. 2020;30: 2171–2194. doi:10.1007/s00332-017-9438-6

227. Mainen,'tll ZF, Joerges J, Huguenard JR, Sejnowski' TJ. A Model of Spike Initiation in Neocortical Pyramidal Neurons. Neuron. 1427.

228. Jacobs AL, Fridman G, Douglas RM, Alam NM, Latham PE, Prusky GT, et al. Ruling out and ruling in neural codes. Proc Natl Acad Sci. 2009;106: 5936–5941.

doi:https://doi.org/10.1073/pnas.0900573106

229. Mofakham S, Fink CG, Booth V, Zochowski MR. Interplay between excitability type and distributions of neuronal connectivity determines neuronal network synchronization. Phys Rev E. 2016;94. doi:10.1103/PhysRevE.94.042427

230. Buzsáki G, Mizuseki K. The log-dynamic brain: How skewed distributions affect network operations. Nat Rev Neurosci. 2014;15: 264–278. doi:10.1038/nrn3687

231. Moradi K, Moradi K, Ganjkhani M, Hajihasani M, Gharibzadeh S, Kaka G. A fast model of voltage-dependent NMDA receptors. J Comput Neurosci. 2013;34: 521–531. doi:10.1007/s10827-012-0434-4

232. Wang H, Stradtman GG, Wang X-J, Gao W-J. A specialized NMDA receptor function in layer 5 recurrent microcircuitry of the adult rat prefrontal cortex. Proc Natl Acad Sci. 2008;105: 16791 LP – 16796. doi:10.1073/pnas.0804318105

233. Tononi G. Consciousness, information integration, and the brain. Prog Brain Res. 2005;150: 109–126. doi:10.1016/S0079-6123(05)50009-8

234. Fujisawa S, Amarasingham A, Harrison MT, Buzsáki G. Behavior-dependent short-term assembly dynamics in the medial prefrontal cortex. Nat Neurosci. 2008;11: 823–833. doi:10.1038/nn.2134

235. Csicsvari J, Hirase H, Czurko A, Buzsáki G. Reliability and State Dependence of Pyramidal Cell–Interneuron Synapses in the Hippocampus: an Ensemble Approach in the Behaving Rat. Neuron. 1998;21: 179–189. doi:https://doi.org/10.1016/S0896-6273(00)80525-5

236. Das S, Suganthan PN. Differential evolution: A survey of the state-of-the-art. IEEE Trans Evol Comput. 2011;15: 4–31. doi:10.1109/TEVC.2010.2059031

237. Storn R, Price K. Differential Evolution-A Simple and Efficient Heuristic for Global Optimization over Continuous Spaces. J Glob Optim. Kluwer Academic Publishers; 1997. doi:https://doi.org/10.1023/A:1008202821328

238. Bhandari D, Murthy C, Pal S. Variance as a Stopping Criterion for Genetic Algorithms with Elitist Model. Fundam Informaticae. 2012;120: 145–164. doi:10.3233/FI-2012-754

239. Leung Y-W, Wang Y. An orthogonal genetic algorithm with quantization for global numerical optimization. IEEE Trans Evol Comput. 2001;5: 41–53. doi:10.1109/4235.910464

240. Xu X, Zheng C, Li N, Shen H, Wang G. The decrease of NMDAR subunit expression and NMDAR EPSC in hippocampus by neonatal exposure to desflurane in mice. Behav Brain Res. 2017;317: 82–87. doi:10.1016/j.bbr.2016.09.035

241. Hutt A, Longtin A. Effects of the anesthetic agent propofol on neural populations. Cogn Neurodyn. 2010;4: 37–59. doi:10.1007/s11571-009-9092-2

242. Hudetz AG, Vizuete JA, Imas OA. Desflurane selectively suppresses long-latency cortical neuronal response to flash in the rat. Anesthesiology. 2009. doi:10.1097/ALN.0b013e3181ab671e

243. Pappas I, Adapa RM, Menon DK, Stamatakis EA. Brain network disintegration during sedation is mediated by the complexity of sparsely connected regions. Neuroimage. 2019;186: 221–233. doi:10.1016/j.neuroimage.2018.10.078

244. Pal D, Li D, Dean JG, Brito MA, Liu T, Fryzel AM, et al. Level of consciousness is dissociable from electroencephalographic measures of cortical connectivity, slow oscillations, and complexity. J Neurosci. 2020;40: 605–618. doi:10.1523/JNEUROSCI.1910-19.2019

245. Hashemi M, Hutt A, Buhry L, Sleigh J. Optimal Model Parameter Estimation from EEG Power Spectrum Features Observed during General Anesthesia. Neuroinformatics. 2018;16: 231–251. doi:10.1007/s12021-018-9369-x

246. Hutt A. The population firing rate in the presence of GABAergic tonic inhibition in single neurons and application to general anaesthesia. Cogn Neurodyn. 2012;6: 227–237. doi:10.1007/s11571-011-9182-9

247. Sleigh JW, Vizuete JA, Voss L, Steyn-Ross A, Steyn-Ross M, Marcuccilli CJ, et al. The electrocortical effects of enflurane: Experiment and theory. Anesth Analg. 2009;109: 1253–1262. doi:10.1213/ANE.0b013e3181add06b

248. Sleigh JW, Voss L, Steyn-Ross ML, Steyn-Ross DA, Wilson MT. Modelling Sleep and General Anaesthesia. Sleep Anesth. 2011;15: 21–41. doi:10.1007/978-1-4614-0173-5_2

249. Bukoski A, Steyn-Ross DA, Pickett AF, Steyn-Ross ML. Anesthesia modifies subthreshold critical slowing down in a stochastic Hodgkin-Huxley-like model with inhibitory synaptic input. Phys Rev E. 2018;97. doi:10.1103/PhysRevE.97.062403

250. Storer KP, Reeke GN. γ-Aminobutyric acid receptor type a receptor potentiation reduces firing of neuronal assemblies in a computational cortical model. Anesthesiology. 2012;117: 780–790. doi:10.1097/ALN.0b013e318269ba6d

251. Banks MI, Krause BM, Endemann CM, Campbell DI, Kovach CK, Dyken ME, et al. Cortical functional connectivity indexes arousal state during sleep and anesthesia. Neuroimage. 2020;211: 116627. doi:10.1016/j.neuroimage.2020.116627

252. Kim M, Kim S, Mashour GA, Lee U. Relationship of topology, multiscale phase synchronization, and state transitions in human brain networks. Front Comput Neurosci. 2017;11. doi:10.3389/fncom.2017.00055

253. Borisyuk R, Borisyuk G. Synchronization of neural activity and models of information processing in the brain. Behav Brain Sci. 1998;21: 833–833. doi:10.1017/S0140525X98241768

254. Matias FS, Carelli P V., Mirasso CR, Copelli M. Anticipated synchronization in neuronal circuits unveiled by a phase-response-curve analysis. Phys Rev E. 2017;95: 052410. doi:10.1103/PhysRevE.95.052410

255. Simonov AY, Gordleeva SY, Pisarchik AN, Kazantsev VB. Synchronization with an arbitrary phase shift in a pair of synaptically coupled neural oscillators. JETP Lett. 2014;98: 632–637. doi:10.1134/S0021364013230136

256. Lu Y, Sarter M, Zochowski M, Booth V. Phasic cholinergic signaling promotes emergence of local gamma rhythms in excitatory–inhibitory networks. Eur J Neurosci. 2020;52: 3545–3560. doi:10.1111/ejn.14744

257. Panzeri S, Macke JH, Gross J, Kayser C. Neural population coding: Combining insights from microscopic and mass signals. Trends Cogn Sci. 2015;19: 162–172. doi:10.1016/j.tics.2015.01.002

258. Stiefel KM, Gutkin BS, Sejnowski TJ. Cholinergic Neuromodulation Changes Phase Response Curve Shape and Type in Cortical Pyramidal Neurons. PLoS One. 2008;3: 7–12. doi:10.1371/journal.pone.0003947

259. Roach JP, Sander LM, Zochowski MR. Memory recall and spike-frequency adaptation. Phys Rev E. 2016. doi:10.1103/PhysRevE.93.052307

260. Mateos-Aparicio P. Impact of GABAA and GABAB inhibition on cortical dynamics and perturbational complexity during synchronous and asynchronous activity. doi:10.5281/zenodo.3856665

261. Lendner JD, Helfrich RF, Mander BA, Romundstad L, Lin JJ, Walker MP, et al. An electrophysiological marker of arousal level in humans. Elife. 2020;9: 1–29. doi:10.7554/eLife.55092

262. Hudetz AG, Wood JD, Kampine JP. Cholinergic reversal of isoflurane anesthesia in rats as measured by cross-approximate entropy of the electroencephalogram. Anesthesiology. 2003;99: 1125–1131. doi:10.1097/00000542-200311000-00019

263. Tononi G, Sporns O, Edelman GM. A measure for brain complexity: Relating functional segregation and integration in the nervous system. Proc Natl Acad Sci U S A. 1994;91: 5033–5037. doi:10.1073/pnas.91.11.5033

264. Luo T, Leung LS. Basal Forebrain Histaminergic Transmission Modulates Electroencephalographic Activity and Emergence from Isoflurane Anesthesia. Anesthesiology. 2009;111: 725–733. doi:10.1097/ALN.0b013e3181b061a0

265. Nelson LE, Guo TZ, Lu J, Saper CB, Franks NP, Mazel M. The sedative

component of anesthesia is mediated by GABAA receptors in an endogenous sleep pathway. Nat Neurosci. 2002;5: 979–984. doi:10.1038/nn913

266. Xie G, Deschamps A, Backman SB, Fiset P, Chartrand D, Dagher A, et al. Critical involvement of the thalamus and precuneus during restoration of consciousness with physostigmine in humans during propofol anaesthesia: A positron emission tomography study. Br J Anaesth. 2011;106: 548–557. doi:10.1093/bja/aeq415

267. Ririe DG, Ririe KL, Sethna NF, Fox L. Unexpected interaction of methylphenidate (Ritalin) with anaesthetic agents. Paediatr Anaesth. 1997;7: 69–72. doi:10.1046/j.1460-9592.1997.d01-34.x

268. Solt K, Cotten JF, Cimenser A, Wong KFK, Chemali JJ, Brown EN. Methylphenidate actively induces emergence from general anesthesia. Anesthesiology. 2011;115: 791–803. doi:10.1097/ALN.0b013e31822e92e5

269. Li Y, Chen D, Wang H, Wang Z, Song F, Li H, et al. Intravenous versus Volatile Anesthetic Effects on Postoperative Cognition in Elderly Patients Undergoing Laparoscopic Abdominal Surgery: A Multicenter, Randomized Trial. Anesthesiology. 2021; 381–394. doi:10.1097/ALN.0000000000003680